UNIVERSITÀ
DEGLI STUDI
DI PADOVA

Universita` degli Studi di Padova

Dipartimento di Fisica e Astronomia “Galileo Galilei”

SCUOLA DI DOTTORATO DI RICERCA IN: FISICA

INDIRIZZO: FISICA

CICLO XXIX

Fabrication and characterization of spiral phase masks for super-resolution

Direttore della scuola : Ch.mo Prof. Gian Guido dall’Agata

Coordinatore dell’indirizzo : Ch.mo Prof. Gian Guido dall’Agata

Supervisore : Ch.mo Prof. Filippo Romanato

Dottorando : Michele Gintoli

Contents

Acknowledgements

I wish to thank my supervisor Prof. Filippo Romanato, for the great opportunity that he gave me to learn about such a complex and interesting field as modern super-resolution microscopy.
I also want to thank prof. Fabio Mammano and prof. Mario Bortolozzi, for kindly accepting me at VIMM and letting me work on the project DYCENDI. I am grateful for the meaningful experience.
Thanks to all the colleagues that helped me and connected with me during these years, both at VIMM (Giulia, Federico, Veronica, Stefano, Alessandro, Saima, Catalin) and at LaNN (Gianluca, Giulia, Enrico, Erfan, Roberto, Michele).
I want also to give my best wishes to Andrea, Chiara and Mirko, and to all the other guys I met while working on the microscope. Keep marching strong!
Finally, I want to thank my friends, no matter the distance between us, and my family, who gave me all the love and support I could have ever wished for.

Chapter 1

Introduction

Fluorescence microscopy has been the pillar of modern biological sciences, due to the high selectivity with which it is able to generate images of specific elements of the cells. Laser-scanning microscopes, and their major upgrade, the confocal microscopes [1], were also able to bring the imaging resolution down to its physical limit and to provide three-dimensional sectioning of thin tissues and cell cultures, which laid the bases for further developments in biology and medicine.

Confocal microscopes, though, are limited in their ability to image details at depth of hundreds of micrometers, which makes them unsuitable for *in vivo* imaging. This is a profound shortcoming, since the capability to image biological dynamics in their own environment gives the possibility to acquire more realistic informations compared to imaging of cell cultures and tissue slices. Alternative platforms were then required, with the ability to image deeper regions of the tissues.

Due to this reason, nonlinear microscopy has been given a lot of attention in the last two decades. The technique makes use of multiphoton interactions with matter in order to generate a signal, with an output intensity dependent on a nonlinear function of the total intensity, hence the name. It provides several advantages over confocal microscocopy: since they rely on red and infrared light, which undergoes less scattering and absorption from biological matter, they can form a strong focal volume even hundreds of micrometers below the sample surface, allowing for deep tissue imaging.

Infrared light, in particular, displays a lower phototoxicity compared to visible light, and as it is weakly absorbed by the tissue, it reduces the physical damage on the sample. As a consequence, nonlinear techniques can be used to perform live imaging, and that made them a resource for the study of the brain neuronal structure and dynamics. Additionally, the signal nonlinear dependency on the incoming intensity gives it a strong axial localization, which means a sectioning capability on par with confocal microscopy.

Another field that developed at the same time is super-resolution mi-

croscopy, where different strategies enable imaging of fluorescent samples at resolution that surpass the diffraction limit to which ordinary microscopes are subjected. Since 1994, when the first method (STED microscopy [2]) was developed, a window has been opened on the inner workings of the cells, where the cells organelles and structures manage its sustainance and its functional role inside the organisms. At this point in time, techniques exist that are able to provide super-resolution on both laser-scanning and wide-field microscopes, and thanks to the continuous developments of the technologies and of new fluorescent molecules they make use of, the capability to reach nanometric scales is commercially available.

Our interest lies mainly on STED microscopy, an upgrade of the laser-scanning systems where the excitation beam that scans the sample is coupled to a laser beam, that uses stimulated emission to force the excited molecules back to the ground state without fluorescent emission. Super-resolution is achieved thanks to a depletion beam with a dark central spot, that suppresses fluorescence only in the outer tail of the excited spot, which then shows a narrower profile that can probe smaller regions of the sample.

It is only natural that, given the advantages of both nonlinear microscopy and STED technique, a combination of the two was tested. A first two-photon excitation STED microscope (TPE-STED) was developed in 2009 [3], then only a few groups [4, 5] tried to do the same, due to the high costs of the laser sources and the electronics needed, and due the severe scattering of the STED wavelengths in thick tissues. High resolution were obtained, nonetheless, at greater depths than confocal STED microscopes (still, $\lesssim 100\mu m$ [4]). To improve the depth imaging capabilities of the technique, several development are still required, like longer excitation and depletion wavelengths and easily switchable fluorescent molecules in these new wavelengths regions.

The objective of the Ph.D. work reported in this thesis was the development of the first TPE-STED microscope with excitation wavelengths in the $[1000-1500]$ nm range and depletion wavelengths in the $[700-900]$ nm range, capable of surpassing the depth limit of current microscopes.

To reach this objective, the depletion and super-resolution capabilities of the fluorescent molecules, ATTO 594, ATTO 647N and mGarnet2 [6] were tested at excitation wavelengths longer than 1000 nm and STED wavelength in the 800 nm proximity.

The dual-beam nature of the platform, makes it also suitable to provide, in a different configuration, two-photon excitation with both the beams, with the addition of a third, "virtual" excitation window at $[900-1100]$ nm, thanks to the two-color two-photon excitation technique [7].

A consistent part of the thesis work was also centered on the fabrication and characterization of optical elements for the manipulation of light (in particular, phase masks) required by the STED microscopes. Though commercial solutions exist and have proved to be affordable and precise, the

available models do not cover the entire range of wavelengths spanned by the tunable lasers of the setup. As the choice of the depletion wavelength depends on the specific fluorescent molecule used to label the sample, it is generally not possibile to anticipate the exact mask model required for the job. The ability to produce tailored optics in relatively short times and with comparable quality respect to the commercial options solves this problem, giving the opportunity to add a degree of freedom for the maximization of the depletion efficiency of the microscope.

The thesis is divided as follow:

- In Chapter 2, nonlinear microscopy is introduced, together with the background knowledge needed to follow the work done to test the capabilities of the main microscope setup
- In Chapter 3, a separate introduction to the super-resolution STED microscopy is given, where the essential concepts are explained and the problems that come with coupling two-photon excitation and STED are explained
- Chapter 4 provides an introduction to how diffractive optical elements, and specifically phase masks work, and to the fabrication process involved in their production
- The microscope setup, the protocols for the preparation of the cellular lines and the procedures for the preparation of the imaging samples are described in Chapter 5
- In Chapter 6, the tests regarding the nonlinear capabilities of the microscope are presented, and the calibration needed to open the virtual excitation spectral window by means of two-color two-photon microscopy is described
- Chapter 7 deals with the experimental work done to align and test the super-resolution STED path on sample tests and on the ATTO 594, ATTO 647N dyes and the mGarnet2 proteins
- The fabrication of the optical masks and the characterization of the optical pattern generated are described in Chapter 8.

Chapter 2

Nonlinear microscopy

2.1 Introduction

The high versatility of fluorescence microscopy and its high target selectivity, combined with the resolution and sectioning capability of the confocal platforms, are at the basis of the advances in biology and medicine of the last sixty years, and still continue to provide vital informations in the most diverse fields of the natural sciences. The technology, though, suffers from severe limitations, mainly regarding the damage done on the sample by the strong laser intensities, and the inability to reach deep regions of the samples, due to scattering and absorption along the torbid medium of biological matter. Even though many strides have been made to reduce the photodamage risk, mainly by the development of ever brighter fluorescent molecules, requiring less intensity to provide clear images, the depth limit of confocal systems depends on the wavelengths used for the imaging. Tissue optical clearing, that is, the use of high-refractive index agents to reduce the inhomogeneities due to internal scatterers, allows to increase the depth limit, but not below the $100\mu m$ threshold.

A solution to the depth limit problem was given by the introduction of nonlinear -also called multiphoton- microscopy [8]. The nonlinear microscope setup is mostly identical to the typical scanning microscope: the laser light is focused in a small spot on the sample, where the contrast mechanism generates a signal that is collected and directed to a single-pixel detector. The pixel raster scan, which can be provided by scanning the laser spot over the sample or viceversa, gives the final image. The difference lies in the contrast mechanism, which requires the interaction of the sample with multiple photons from the laser sources, with identical (degenerate) or different (nondegenerate) wavelengths λ_i, in a single quantum event. Examples are the two-photon excitation (TPE) and three-photon excitation (3PE) microscopes [9, 10, 11], involving degenerate multiphoton absorption, and the harmonic generation (HG) microscopes, based on degenerate mul-

tiphoton elastic scattering. Those and other kinds of interactions are shown in Figure.2.1, by means of their Jablonsky diagrams. As a general simplification, multiphoton processes can be thought as the almost simultaneous occurrence of statistically independent single-photon interactions. Each one of them, given a total amount N of available points of interaction inside the material, will affect a fraction $n_i$proportional to the density of photons available at λ_i, that is, proportional to the respective beams intensity I_i. The fraction that will be involved in the actual multiphoton interaction will then be approximable to the product of all these single-photon occurrences, $n_{\mathrm{NL}} = \prod n_i(I_i)$ resulting in a nonlinear dependency on the total light intensities, from which the "nonlinear" denomination was derived. All of these systems provide an output signal whose frequency is approximately given by a linear combination of the incoming photons frequencies. This means that the light sources must operate at wavelengths longer than the one detected. In practice, nonlinear microscopes operate mostly in the far-red and NIR spectra, whose wavelenghts undergo less scattering and absorption than the optical wavelengths.

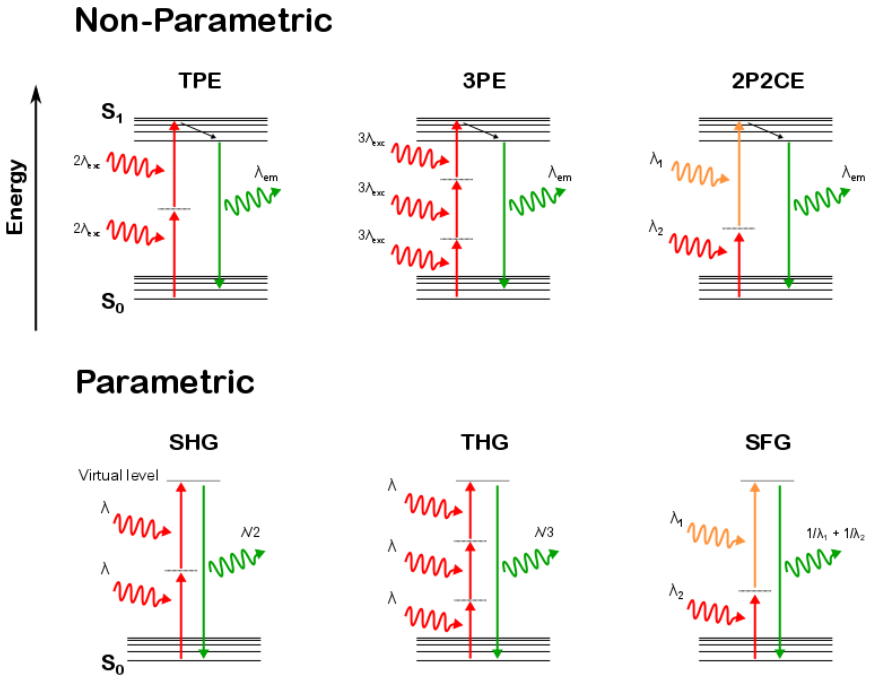

Figure 2.1: Diagram of the main nonlinear processes used in microscopy. **Top)** Non-parametric processes, involving absorption of the photons and then incoherent and independent from phase considerations. **Bottom)** Parametric processes, which don't involve transitions between different excited states, and then coherent and dependent on the relative phase between the photons involved in the interaction.

Scattering and absorption are the main reasons for the limited imaging depth reachable by single-photon excitation (SPE) systems (at best $\sim 100\mu m$). In biological tissues, we can expect the light power that reaches the focus of the objective lens at the distance z from the surface, to follow a Lambert-Beer-like exponential decay [12]:

$$P(z) = P(z=0)\mathrm{e}^{-\frac{z}{l_s}-\frac{z}{l_a}} \tag{2.1}$$

where l_s, l_a are respectively the scattering and absorption mean free path (MFP). The natural consequence is that, to reach deeper levels below the sample surface, one needs to exponentially increase the laser power, up to a point where a background signal from the surface is generated, gradually reducing the image resolution. Scattering can be expressed as a combination of Rayleigh and Mie scattering, the first strongly dependent on the excitation wavelength (MFP$\propto \lambda^{-4}$), the second only weakly dependent on it, though with a MFP that still surpasses the $100\mu m$ limit as one moves from 800 nm further into the IR spectrum [12]. Increasing the excitation wavelengths then always reduces the amount of scattering undergone by the incoming light, letting more power to reach the focus. Absorption due to organic matter is particularly strong in the UV and visible spectrum, but in the IR window the main contribution is given by water absorption, which becomes stronger at longer wavelengths, up to 1450 nm where the MFP reaches a minimum of about $200 - 300\mu m$. The following $1600 - 1800$ nm window, where the absorption MFP returns longer than 1 mm, is the ideal region where to observe higher multiphoton interactions, like 3PE [13] or third harmonic generation (THG) [14, 15], and it was used to image detail even below the 1 mm depth limit.

The drawback related to the use of nonlinear interaction as sources of signal is given by their low efficiency: being the probability of multiphoton absorption -or scattering- approximately the product of each single-photon interaction probability, we expect to see extremely unlikely events. As an example, the single-photon absorption cross-section is about $\sigma_i \approx 10^{-16} - 10^{-18}\,\mathrm{cm}^2$, meaning that the two-photon absorption cross-section falls easily 16 orders of magnitude below. This translates into the need for extremely intense laser sources, with irradiances of about $100\,\mathrm{GW/cm}^2$, that would be impossible to generate with a CW laser source. Pulsed lasers are then required, which provide high irradiances while keeping low the total energy administered to the samples. The preferred choices are femtosecond-pulse lasers, specifically the Ti:Sapphire models, which work in the $500 - 900$ nm range, at 10-to-100 MHz pulse rates. Many models provide a tunable wavelength, which can be useful to widen the palette of usable fluorophores.

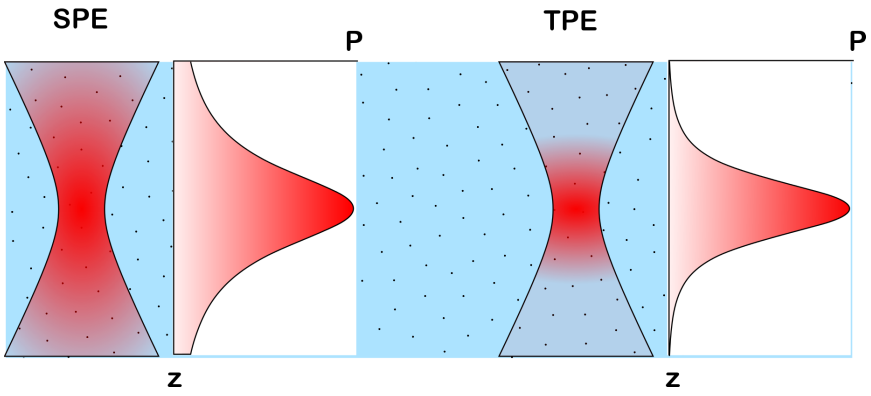

Figure 2.2: Comparison between the SPE and TPE fluorescence generation: SPE **(left)** depends linearly on the excitation intensity, so that slow variations cause similarly slow changes in the number of molecules excited along the axial direction. TPE, on the contrary **(right)**, depends on the second power of the excitation intensity, so that even at small distances from the focus plane the reduction of the incoming light causes a steep fall of the number of excited molecules.

Even though the low cross-section of multiphoton interactions provides a significant handicap when compared to the single-photon processes, it also reduces the amount of unwanted interactions from out-of-focus regions of the beam. Together with the nonlinear dependency on the total photon density, which exasperates the effect of any intensity gradient, this means that only the small focal volume will be involved in the generation of useful signal (Figure.2.2). Common characteristic of nonlinear microscopes is then an intrinsic sectioning capability over the axial direction, without the need for confocal filtering techniques. The absence of out-of-focus interactions is a strong reason to adopt nonlinear microscopes when working with thick tissue samples, as the total damage and photobleaching generated by the beams are greatly reduced. Furthermore, since the entirety of the signal comes from a confined focal spot, information can be acquired by both ballistic and scattered photons, increasing the available photons per pixel, which somewhat reduces the handicap given by the low interaction probability. Following the nonlinear dependency on the light intensity available on the sample, the resolution too depends nonlinearly on the beams focal spots on the focal plane. In the single-photon case, the resolution is proportional to the width of the focal intensity distribution of the laser, also called the point spread function (PSF) of the illumination system, which we describe as a function of its adimensional axial coordinates (v, u):

$$h_{1P}(v,u) \quad , \quad (v,u) = \left(\frac{2\pi\,\mathrm{NA}\,r}{\lambda}, \frac{2\pi\,\mathrm{NA}^2\,z}{n\lambda} \right) \tag{2.2}$$

where (r, z) are the physical cylindrical coordinates originated on the focal point, $\mathrm{NA} = n \sin\alpha$ is the numerical aperture of the focusing optics, the product of the sample refractive medium and the sine of the focused light cone half-angle. In the nonlinear case, where a signal at $\lambda_{\mathrm{NL}}^{-1} = \sum_i (\pm)\lambda_i^{-1}$ is generated, with intensity $I_{\mathrm{NL}} = \prod_i I_i$, the PSF is expressed as:

$$h_{\mathrm{NL}}(v,u) = \prod_i h_{1P}\left(\tfrac{\lambda_{\mathrm{NL}}}{\lambda_i} v, \tfrac{\lambda_{\mathrm{NL}}}{\lambda_i} u \right) \tag{2.3}$$

his results in a nonlinear PSF narrower than the single-photon λ_i PSFs, but broader than the single-photon λ_{NL} PSF. Compared with the common fluorescence an confocal systems, then, the resolution is somewhat at a loss, which is not a strong handicap, since the main reason for using a nonlinear platform is to guarantee deep imaging with lower damage on the biological tissue.

As of now, nonlinear microscopy (in particular multiphoton excitation (MPE) microscopy) has represented one of the principal tools for the study of neural networks in brain slices and in whole brain imaging [16]. In this chapter, we show the main characteristics and advantages of the most nonlinear microscopy techniques used today, providing the needed background to follow the work done during the thesis years.

2.2 Two-Photon and Three-Photon Excitation Microscopy

two-photon excitation (TPE), the simultaneous absorption of two identical photons by a fluorescent molecule, was first predicted by Maria Goeppert-Mayer in 1931 [17], but demonstrated only in 1990[9], after the development of mode-locked lasers.

Since the photons that excite the molecule must be identical, their energy is typically greater or equal to half the excitation energy, and their wavelength is shorter or equal to twice the equivalent SPE process wavelength. To excite molecules in the ultraviolet (UV)-optical window, infrared light in the $600 - 1200\,\mathrm{nm}$ is typically used, with all the advantages we described above (low scattering and absorption, low damage to the sample). TPE is mostly used to provide excitation of UV molecules without relying on UV optics [18], and for deep-tissue and in-vivo imaging with fluorophores and fluorescent molecules in the visible range [19]. For wavelengths shorter than

1300 nm, the absorption length of infrared (IR) light is greater than 1 mm, even by orders of magnitude, so that the attenuation of IR light is caused only by scattering inside the sample, that typically shows scattering lengths values between $200\mu m$ and $400\mu m$. Thanks to these favorable conditions, commercial and simple custom setups are able to reach depths of about $\sim 700\mu m$, while dedicated systems working in the $1200 - 1400$ nm window were able reach and surpass the 1 mm limit [20].

TPE cross-sections are usually measured in Goeppert-Mayer (GM) units, ranging from a few GM for conventional fluorophores to hundreds of GM for engineered probes. Research on fluorescent molecules dedicated to TPE imaging is a strong field, continuously growing. A number of non-organic probes also exists, like quantum dots (QDs), impurity-vacancy sites in diamond nanocrystals (NDs) and other fluorescent nanoparticles. They are characterized by extremely large cross-sections (easily surpassing the thousand GMs), but they are also rarely used in common imaging scenarios, due to their size and often due to their toxicity.

In a simplified scenario, we can expect the TPE spectrum to coincide with the SPE equivalent, just stretched over a wavelength interval twice as large. Experimental TPE spectra do have such a behaviour, but with peaks always blue-shifted respect to their expected positions. This has been attributed to the presence of additional vibrational transitions that couple to the pure electronic ones, easing the parity requirements that would otherwise be violated [21, 22]. The different physical nature of single-photon and two-photon excitation affects also the absorption efficiency: while the SPE scenario favours direct transitions to the first excited level, meaning the highest peak is found at the longest wavelength, TPE absorption of higher levels is strongly enhanced [23]. Many common fluorophores and fluorescent proteins have then strong absorption peaks in the $700 - 800$ nm interval, corresponding to the secondary SPE peaks at $300 - 400$ nm.

First demonstrated in 1996 [10, 11, 8], 3PEM exploits the simultaneous absorption of three photons to generate fluorescence. It works at longer wavelengths than two-photon microscopy, with immediate advantages regarding background noise, attenuation losses and sectioning capability. Specifically, the 3PE signal falls as $\sim 1/z^4$ with increasing distance from the focal spot, whereas the TPE signal falls as $\sim 1/z^2$. Just as for TPE, three-photon excitation is mainly used to reach UV excitation windows with available sources [24], or to reach extremely deep regions inside living or explanted tissues [13]. Currently, its main application is the imaging of the brain innermost regions (white matter and hippocampus), which is made possible by imaging in the $1200 - 1300$ nm and $1600 - 1800$ nm otical windows, where light attenuation is mostly caused by water absorption. Depths greater than $1.5\mu m$ were recently demonstrated [13] with specific, low-pulse repetition sources at 1700 nm.

2.3 Multicolor Multiphoton Excitation Microscopy

multicolor multiphoton excitation (MCMPE) techniques are non-degenerate equivalents of the previously described multiphoton excitation (MPE) techniques. Given the need for multiple laser sources at different operating wavelenghts, it usually is used only in its two-photon implementation, 2C2PE (in this thesis ,we will use the equivalent acronym TCTPE).

It was first observed in 1996 [7], when picosecond pulses at 750 nm and 375 nm were used to excite the ultraviolet emission of p-terphenyl at 340 nm. It was initially adopted to push the spectral excitation window of Ti:Sapphire laser sources into the ultraviolet interval [25, 26, 27, 28], specifically for the imaging of the tryptophan amino acid, which shows an absorption peak at 280 nm. In 2012, two-color two-photon excitation (TCTPE) was used to provide excitation in the intermediate spectral window of a pump+optical parametric oscillator (OPO) system for brain imaging [29]. This extended wavelength range made it possible to observe the entire palette of "Brainbow" proteins expressed by neurons.

As TCTPE requires the simultaneous absorption of photons from different pulsed laser sources, it is fundamental to achieve a spatial overlap as high as possible between the beams, together with a precise temporal superposition of the pulses. This latter requirement can be met either using an a dedicated synchronization circuitry connecting the laser platforms, or using pumped laser systems, which provide naturally synchronized pulse trains, whose relative delay can be simply adjusted with a mechanical delay line or retroreflector. For pulses with a Gaussian temporal profiles that belong to beams at different wavelengths, one with power P_1 and one operating at P_2, the intensity of the signal from the third excitation channel will scale as $P_1 P_2 \ \exp(-\Delta t/\tau_{\mathrm{TIIC}})$, where Δt is the temporal delay between the pulses peaks and τ_{TIIC} is the $1/e^2$ width of the temporal intensity intercorrelation function (TIIC) between the pulses [29].

The image signal then increases quadratically with the total excitation power (or intensity), while being proportional to the intensity of each laser.

2.4 Harmonic Generation Microscopy

Harmonic generation shares with TPE and the other nonlinear excitations the multi-photon nature of the process, but they differ in the fact that no photon absorption is required. Classically, the concept that lies at the heart of these phenomena is the polarization of the molecule electron cloud by means of an external electromagnetic field [30]. Oscillating electromagnetic fields act on molecules, which can be considered as neutral systems, by generating a dishomogeneity in its charge distribution. This causes the molecule to act as a dipole, which can be characterized by a polarization vector os-

cillating at the same frequency of the incoming light. As the polarization oscillates, it generates a propagating electromagnetic field, a scattered wave. We can interpret this phenomenon in a quantum mechanical framework, as the elastic scattering of single photons with the molecules.

As the strength of the electromagnetic field that interacts with the material increases, it reaches a point where the amplitude of the polarization oscillation stops increasing linearly, resulting in a non-harmonic scattered wave being emitted. To describe this phenomenon we can think the scattered wave as the sum of multiple waves with wavelengths long an integer fraction of the one of the incoming light (and that we call "harmonics"). As the field becomes stronger, the contribution of the n-th harmonics to the scattered wave increases proportionally to the n-th power of the light intensity, resulting in a considerable fraction of the energy being converted to the new wavelength. The quantum mechanical interpretation is that at some point the number of photons in the proximity of the molecules rises to a level at which single-photon-molecule interaction starts to be penalized in favor of multiple-photon-molecule interactions, which return as a product single photons with n times the energy of the incoming ones.

As no light absorption is required, harmonic generation is a coherent process. This means that not only the total harmonic signal will depend nonlinearly on the total irradiation intensity, but it will also depend nonlinearly on the density of the single emitters due to interference between their individual contribution. When particular conditions (named "phase-matching" conditions) are met, it is possible to observe significant harmonic emission from constructive wave interference. These phase-matching condition cause HG emission to be a highly directional phenomenon, in contrast with the low anisotropy of the incoherent fluorescence emission.

Symmetry rules also apply to the emission of higher order harmonics, with different results: second harmonic generation (SHG), as an example, can take place only when the molecules involved are noncentrosymmetric, meaning that they don't posses a central point of symmetry. The symmetry requirements can also not be caused by the intrisic nature of the process, but simply by the context of the specific HG process involved. It is known that third harmonic generation (THG) can take place with any kind of molecule, but when it is generated by a focused (Gaussian) beam in a bulk material, the phase inversion inside the focus causes destructive interference between the two generating regions, so that no signal can be observed. THG from focused beams can then be observed only when dishomogeneities in the optical properties of the material are present in the beam focus, that is, in correspondence of interfaces and discontinuities [31].

When used in the field of microscopy, HG processes give an extraordinary selectivity to specific structural characteristics of the sample. SHG is now routinely adoperated to observe ordered noncentrosymmetrical molecules ensembles (collagen fibers [32, 33, 34], starches [35, 36], cellulose [37, 38] are

just a few examples). THG proved to be a precious tool for the observation of refractive index discontinuities and interfaces (myelin sheats in neurons [39] and water-lipid interfaces [40], just to name a few). Since harmonic generation does not involve the absorption of photons, it poses far less damage risks for the sample than MPE. Additionally, since the processes can happen at any wavelength where competing excitation process don't interfere, they constitute a set of truly label-free tools, which can be used to complement the MPE techniques with informations regarding the structural elements of the tissues. Sharing also the deep imaging and sectioning capabilities of multiphoton excitation platforms, they can work in tandem over similar depth ranges, with the only limitations given by scattering and absorption by the sourrounding medium.

Chapter 3

STED microscopy

3.1 Introduction

The ability of a microscope to image subcellular structures is limited by a fundamental issue: far-field optics like lenses and mirrors are unable to focus light in spots smaller than its own wavelength. This limit is a physical consequence of the wave nature of light, and was given a mathematical form in 1873 by Ernst Abbe [41]. More specifically, given an arbitrary optical system, which focuses monocromatic light at a wavelength λ, inside a transparent material with refractive index n, with a convergence semiangle α, the minimum radius of the spot it can form is given by the following expression [42]:

$$\Delta r = \frac{\lambda}{2n \sin \alpha} = \frac{\lambda}{2\,\mathrm{NA}} \tag{3.1}$$

where NA is the numerical aperture of the optical system. Even ideal systems with no defects or aberrations are bound to work on a scale that can at best be reduced to that of the working wavelength, that is way they are called "diffraction-limited" systems. In a microscope, any two light sources separated by a distance smaller than Δr will be imaged as a single entity, i.e., they won't be "resolved", and no detail at lower spatial scales will be observed. The same can be told about single sources smaller than Δr, that will be imaged as a light pattern with geometry and extension dependent only on the optical system (the point spread function, PSF). This behaviour is shared by wide field microscopes, where the lenses are required to project an image of the sample onto a CCD or the observer's eyes, and laser-scanning microscopes, that generate the image by counting the photons emitted by a luminous point scanned over the sample plane. In the former case, the resolution can be quantified by the dimension of the PSF projected on the CCD when imaging a point source; in the latter, the resolution of the system can be expressed as the extension of the scanned spot. This chapter gives a brief description of the techniques developed to surpass the diffraction limit,

and provides basic concepts and definitions that will be used throughout the presentation of the stimulated emission depletion (STED) setup in Chapter 5 and the description of the experimental work done in Chapter 7.

3.2 Super-resolution methods

Since the beginning of the 20^{th} century, researchers explored relentlessly optical imaging system able to surpass these limitations. As the Abbe limit applies to all of the optical systems working with light in conditions of free-space propagation, one first method was devised by Pohl in 1991 [43, 44], based on a near-field approach: an optical fiber with a sub-μm tip was scanned over the sample, both delivering and collecting light at spatial scales of the orders of tens-to-hundreds of nm. The system limitation lies in the low penetration of near-field waves, capable of probing only layers a few nanometers thin, and by the scanning probe architecture, that relies on piezoelectric actuators, with high resolution (fractions of a nanometer) but small translation ranges ($\leqslant 200 \times 200 \mu m^2$ fields, few μm heights) and slow throughputs (tens of $\mu m/s$).

Other strategies were employed to reach higher resolutions while still using far-field optics. Starting from 1957, phase and amplitude modulation of the focused beam with complex phase masks was investigated [45, 46]. Using diffraction of multi-ring phase patterns is able to confine the light better than common optics, but never less than half of the diffraction limit was achieved. The resolution enhancement provided this way is always the result of a tradeoff, be it between the beam widths over two orthogonal directions, or between the overall reduction in the spot size and the total intensity transmitted on the focus.

Structured illumination microscopy (SIM) is another super-resolution strategy invented in 1998 by Tony Wilson [47]: the sample is imaged as in wide-field microscopy, but the illumination is provided by an optical sinusoidal pattern, so that the Moiré fringes emitted by the sample are detected. Once multiple photograms from different configurations of the light grating are taken, a mathematical algorithm is then employed to reconstruct the original image. In this way, SIM provides a wide field of view, quicly and reliably, with twice the resolution of common wide-field microscopes.

PSF modulation and SIM belong to a class of systems that use diffraction itself to stretch the resolution limits. As the Abbe limit is a natural consequence of diffraction, though, it is simply not possible to achieve arbitrarily high resolution enhancements. More precisely, as long as the captured signal depends linearly on the illumination intensity, the achievable improvement will always be limited to a factor of 2.

Modern super-resolution methods rely on the physics of fluorescent molecules, more specifically they make use of transitions between distinguishable fluo-

rophore states in order to discriminate the signal from neighbouring regions of the sample. Depending on the working principle, super-resolution approaches separate in two families: coordinate-stochastic - also called single-molecule localization microscopy (SMLM) - and coordinate-targeted methods [48].

SMLM methods, that can be applied to any wide-field microscope, are based on the properties of known stochastic distributions. A single fluorescent molecule can be considered as a point source, and imaging with a microscope will return a PSF with a Gaussian (or Lorentzian) radial profile. The image of the molecule will then be blurred, but its position can be determined fitting the PSF and calculating its centroid. If the molecule emitted a number N of photons, the maximum precision with which its position r can be determined is given by:

$$\Delta r = \frac{\lambda}{2\pi \,\mathrm{NA}\,\sqrt{N}} \tag{3.2}$$

for any given wavelength λ and numerical aperture NA, the localization precision is set by the number of photons detected from the molecules, limited only by practical issues, such as the image signal-to-noise ratio (SNR), the optical pixel size and other specific bias due to the sample and environmental conditions.

Single fluorophore detection was demonstrated in 1989, for solid crystals at cryo-temperatures, first by absorption [49] and then by fluorescence [50], then it was followed by the detection of bursts of fluorescence from single fluorophore molecules in acqueous solution at room temperature [51, 52]. In 1995 the application of isolating and localizing the fluorophores for resolving biological features was introduced by Betzig [53]. Initially spectral separation was suggested for the fluorophore isolation implemented a few years later van Oijen et al. [54].

As spectral isolation was inherently difficult, and limited to a finite number of fluorophores at a time, the method was then discarded in favour of an approach based on fitting of images before and after each single photobleaching, with which positions with 5 nm precision could be determined [55]. The last step toward SMLM imaging was made after the advent fo photoswitchable proteins, by Betzig and co. in 2006, when the sequential excitation of a subset of fluorophores to spectroscopically distinct states was used to collect images with spatially separated PSFs, that could be separately localized. The method was called Photoactivated localization microscopy (PALM) [56]. PALM was then followed by similar techniques, namely fluorescence-PALM (fPALM, Hess et al. [57]), STORM (Zhuang and co. [58]) and its direct-STORM variant (dSTORM [59]). Other methods are still being developed, with small differences in the implementation of the PALM principle of operation.

Coordinate-targeted methods, contrary to SMLM methods, can be applied to laser-scanning systems, where the width of the scanning spot determines the image detail. The resolution gain is achieved by reducing the occupation of the molecular state involved in signal emission, everywhere but for a subdiffraction-sized region. A super-resolved fluorescence spot is then created, that can be scanned with a shorter step, returning details on sub-micrometric scales. The reduction of the emissive state population is achieved by diverting the molecules to other states using reversible saturable optical fluorescence transitions, from which the acronym RESOLFT has come to be.

The first of the RESOLFT technique to be invented was STimulated Emission Depletion (STED) microscopy, developed in 1994 by Stefan Hell [2], that uses stimulated emission to reduce the excited spot diameter. In 1995, Hell and Kroug introduced the concept of ground-state depletion (GSD), relying on singlet-triplet state transitions [60]. Other methods were then developed in the first decade of 2000, employing reversible transitions in photoswitchable fluorescent proteins [61] and organic dyes [62], and able to work at much lower intensities.

Though both SMLM and RESOLFT use transitions between different molecular states to achieve super-resolution, their differences makes them suitable for almost opposite cases, so that it is not incorrect to define them as complementary techniques.

The clear advantage of SMLM is given by the low requirements on the setup hardware: given a regular wide-field microscope, it is possible to turn it into a PALM/stochastic optical reconstruction microscopy (STORM) system by adding the light source needed for the isolation of the fluorescent molecules. The sensibility of the approach is such that one single switching cycle per molecule would already be sufficient to produce an image, also implying that all the emitted photons can in theory contribute to the signal and to the resolution gain.

To achieve these levels of collection efficiency, though, sensitive cameras are required, and the observation must be done in a configuration with low SNR, both from the environment and from excitation/isolation light. One example is total internal reflection fluorescence microscopy (TIRF), where the excitation beam is directed to the sample with an inclination higher then the total reflection angle, providing excitation of the fluorophores by means of the evanescent field on the outside of the reflection surface. This system has a penetration depth lower than 100 nm, that limit also the penetration depth reachable by PALM/STORM methods. An additional disadvantage is given by the tens of thousands of images required to achieve a number of photons suitable for super-resolution localization of the fluorophores: this high number can only be provided at the expense of both the temporal resolution and the processing powers required to process the images.

In RESOLFT approaches, localization is intrinsic to the scanning strat-

egy, so that only a small number of photons per pixel is required and the acquisition times are the same of the diffraction-limited technique. The corresponding disadvantage is given by the fact that most of the switching cycles a molecule undergoes do not contribute to the detected signal. If high intensities are required to inhibit the emissive state population (as in the case of STED microscopy), this implies higher bleaching rates and the risk of damaging the sample.

As a means of comparison between the different SMLM and RESOLFT methods, Table.3.1 provides informations about the average specifics of the most common super-resolution instruments.

Methods	**Resolution**	**Acquisition time****
SIM	100 nm	$\sim 1s$
PALM	50 nm	$> 2s$
STORM	50 nm	$> 2s$
STED (confocal)	$40 - 70$ nm	$10 - 100s$
RESOLFT*	$80 - 100$ nm	$> 500s$

Table 3.1: Comparison between the most common super-resolution methods. Data are taken from [63].
*RESOLFT here refers to super-resolution specifically on photoswitchable molecules.
**limited to the acquisition of a $50 \times 50\mu m$ field.

3.3 STED microscopy

During stimulated emission, an excited fluorescent molecule is forced back to its ground state by the interaction with a traveling photon at a wavelength belonging to its emission spectrum. The de-excited molecule emits a second photon, identical in wavelength, phase and direction to the travelling one, as shown in Figure.3.1. Stimulated emission cross sections have similar values compared to the excitation process, and the rate at which it occurs in an excited fluorophore population is proportional to the intensity of the light used. A strong radiation, then, can force molecules to return to the ground state at a faster rate than spontaneous emission, so that the excited population gets depleted to a fraction of its original size before having a chance to emit its spontaneous fluorescence signal [64] (Figure.3.2). Using detection filters to discard the stimulated emission signal, the depletion process appears as a reduction of the fluorescence light.

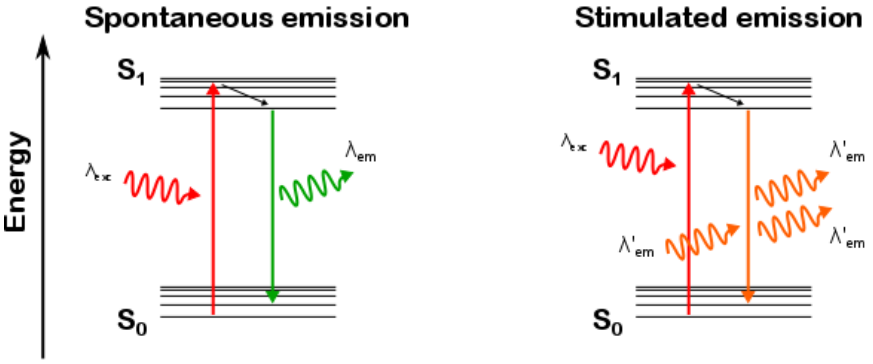

Figure 3.1: Jablonsky diagrams of the processes of spontaneous emission and stimulated emission.

The efficiency of the depletion process can be measured comparing the residual depleted fuorescence with the unaffected signal: the ratio between the two quantities follows a nonlinear behaviour, with a quick initial signal reduction at low intensities, which reaches a tipping point after which small

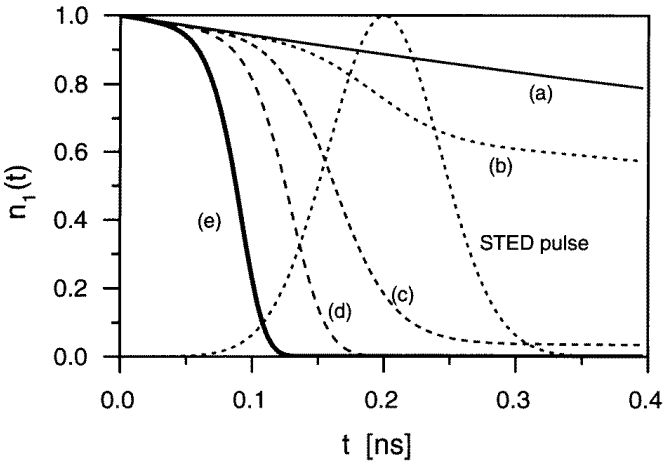

Figure 3.2: Temporal representation of the stimulated emission depletion (STED) process: a population of fluorophores is brought to the excited state at the instant t=0, and it is then irradiated by a laser pulse (represented by the bell function at the center of the image) with a wavelength belonging to the emission spectrum of the molecules. The decaying curves show the temporal evolution of the excited population for different powers of the STED pulse: (a) 0, (b) 10, (c) 100, (d) 500, (e) 1000 MW/cm^2. Higher STED powers induce faster decay rates, until the excited state is completely estinguished (saturation). Adapted from [64]

additional depletion efficiency must be acquired at the expense of considerably stronger intensities.

This depletion "saturation" is due to the fact that only a few excited molecules are left, and the chance of interacting with a photon is low. The intensity threshold at which the saturation regime starts is called the saturation intensity, I_{sat}, and characterises the depletion efficiency of a specific molecule, though depending also on the environment parameters (pH, temperature, bonds with other molecules, electric field, ionic concentration, and so forth) of the sample. The typical I_{sat} order of magnitude is $10 - 10^3\,\text{MW/cm}^2$, higher than SPE requirements, but easily accessible with TPE light sources.

STED microscopy is a two-laser technique, where the main laser generates an excited spot on the sample, and then a second laser with a dark central point (a "doughnut" beam) is used to deplete the outer tail of the PSF until saturation (Figure.3.3). The result is a smaller excited spot, that can be scanned over shorter steps, resulting in a greater resolution.

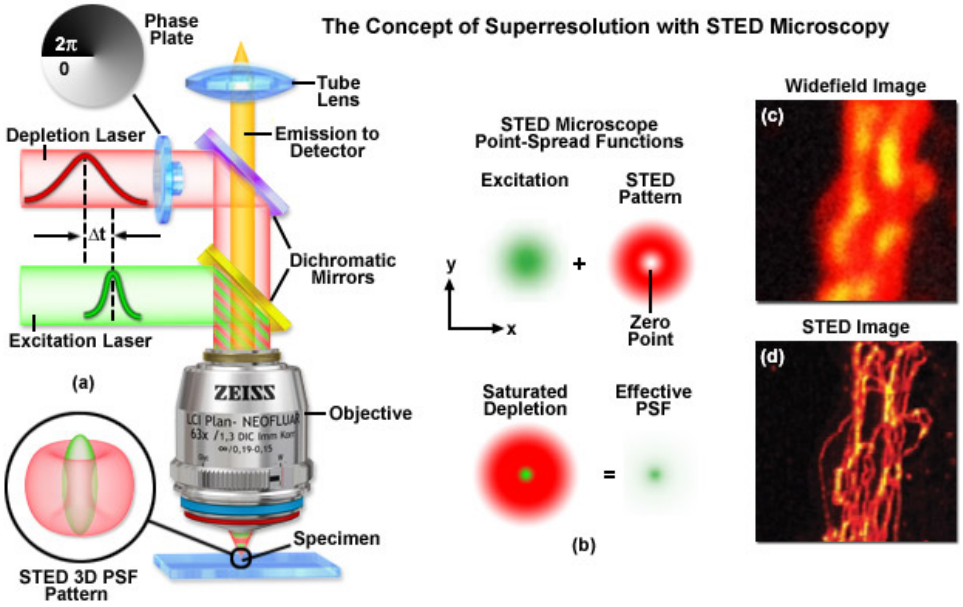

Figure 3.3: Concept of STED microscope: **(a)** the excitation pulse is followed by a stretched depletion pulse with a dougnut-like intenstiy distribution, **(b)** As the excited spot is irradiated by the depletion light, it is selectively de-excited on its outer tail, while its central portion is left unaffected and can be scanned over the sample at smaller steps. **(c-d)** The result, is a higher resolution compared with widefield (or confocal). Adapted from Zeiss Campus STED tutorial: *http://zeiss-campus.magnet.fsu.edu/tutorials/superresolution/stedconcept/indexflash.html*

We can give an approximate guess for the final PSF dimensions by assuming the ring intensity to be much higher than the saturation intensity: fluorescence will be emitted only from the center of the doughnut intensity distribution, that we can approximate with a radial parabolic profile, $I_{\mathrm{STED}}(r) \approx aI_0r^2$. The area unaffected by the depletion process will be confined to the region where $I_{\mathrm{STED}}(r) < I_{\mathrm{sat}}$, that is, $r < \sqrt{I_{\mathrm{sat}}/aI_0}$. This inverse square-root dependency on the beam intensity is confirmed by more rigorous analyses [65], where it appears in the form of a generalized Abbe principle:

$$\Delta r_{\mathrm{STED}} = \frac{\Delta r}{\sqrt{1+aI_0/I_{\mathrm{sat}}}} \tag{3.3}$$

STED microscopy is then able to provide a precise control of the image resolution by modulation of the depletion intensity. The size of the excited spot can be arbitrarily decided, providing in theory limitless resolution. Experimental values show resolutions down to 20 nm [66, 67, 68, 69] (with average results of $40-50$ nm), limited only by the photobleaching and phototoxicity due to the laser intensities required.

Given a specific fluorescent tag, the depletion efficiency depends on the STED wavelength, λ_{STED}: high STED cross-sections can be reached near the emission peak [70], but due to the overlap with the emission spectrum, the risk of undesired excitation events from depletion photons increases. STED wavelengths are then typically chosen far from the emission peak, with a lower depletion efficiency that must be compensated by the beam intensity. Pulsed lasers are typically used, both as excitation and depletion light sources, in order to temporally separate the processes and to provide higher intensities. In this case, there are requirements that must be met:

- The excitation pulse should be shorter than the molecule's mean vibrational relaxation time τ_{vib}(typically a few picoseconds). As Kasha's rule predicts fluorescence emission only from the lowest excited state, a short excitation interval brings the fluorescent molecules to the excited state without risk of fluorescence emission. Femtosecond pulses, as the ones used in TPE microscopy, are typically chosen.

- The depletion pulse should leave the de-excited molecules the time to relax to their lowest vibrational level, to avoid the occurrence of re-excitation cycles that would reduce the depletion efficiency. The power should then be kept low enough to get a stimulated emission mean time longer than τ_{vib}. Since a certain amount of additional on-off cycle must be always considered, though, it is also important to provide pulses much longer than τ_{vib}, typically tens-to-hundreds of picoseconds, so that the chance for vibrational relaxation increases. Longer pulses are also preferred due to their lower peak intensities, that reduce the probability of TPE by the depletion wavelengths.

– The STED pulse has to closely follow the excitation pulse, so that the lowest amount of spontaneous fluorescence can be emitted by the spot before the actual depletion interval. This ideal delay can be found with a simple check on the residual fluorescence signal left by the pulse. Figure.3.4 shows the typical fluorescence signal dependence on the delay time: the correct alignment of the pulses corresponds to position of the minimum of the curve. For shorter (or negative) delays, there is a sharp increase in the amount of fluorescence, which means a fraction of the depletion energy arrives on the sample before the excitation pulse and is lost. For longer delays, the residual fluorescence increases at a slower rate, since it follows the spontaneous emission mean time.

STED limitations are due to the requirement of high intensities, that have a natural limit in the damage and phototoxicity induced on the sample. Even when safe laser intensities are used, the additional on-off cycles that the molecules need to withstand increases photobleaching, which means only a few images can be acquired before the sample loses available fluorescent molecules.

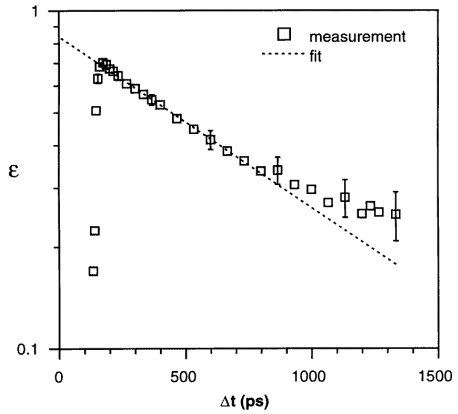

Figure 3.4: Dependency of the depletion efficiency on the delay between excitation and depletion pulses in a STED setup. As the delay brings the STED pulse immediately after the excitation pulse, the efficiency increases rapidly, since less depletion photons are lost before the excitation instant. The longer decaying ramp at longer delays corresponds to the slow build-up of fluorescence photons emitted by the excited molecules after the excitation pulse. Adapted from [64].

Bleaching reduction can be achieved by using low pulse repetition rates ($< 1\,\mathrm{MHz}$) [71]: as the triplet states where soon-to-be-bleached molecules have settled live for times of the order of the μs, leaving the sample unaffected for comparable times helps most of the triplet population to return to the ground state, so that the available excitable fraction is replenished.

3.4 TPE-STED

STED is an upgrade to an already existing laser-scanning imaging system, and its implementaiton does not depend on the mechanism by which fluorescence is generated. Addition to TPE microscopes was then a natural thought, the first experiments made in 2009 by Moneron and Hell [3], giving resolutions of 50 nm just below the coverslip surface, and 90 nm at depths of about $40 - 50\mu m$ (Figure.3.5, left panel). Other platforms followed, mainly dedicated to the super-resolution imaging of neural tissues [72, 73, 74, 5, 4], with comparable resolutions and depth limits.

Thick tissues present an obstacle to STED imaging due to the absorption and aberrations that the doughnut beam suffers while travelling inside the sample. Absorption plays the main role, as it reduces the depletion light reaching the focal spot, following the Lambert-Beer exponential trend shown in eq.2.1. It is possible to characterize analytically the loss of resolution by using in eq.3.3 an "effective" saturation intensity, proportional to the intensity at the sample surface multiplied by an exponential factor $e^{i\ell z}$, dependent on the imaging depth z and the tissue average absorption length ℓ (Figure.3.5, right panel, plots c and d) [4]. The role of aberrations is linked to an asymmetric modulation of the intensity profile on the focal plane, that generates both a reduction of the peak depletion intensity and a deformation of the beam shape on the focal plane. The latter is particularly dangerous, as it can divert a fraction of the beam energy on the doughnut center and cause a dramatic reduction of both the resolution gain and the image SNR. If compensation mechanisms -e.g. higher laser powers and adaptive optics [75, 76, 77] - are not provided, the resolution gain will fall in the deeper regions, reaching usually 3-4 times the performance of a confocal system. Given lasers in the far-red/NIR regions ($\sim 800\,\mathrm{nm}$), the expected resolutions are $\sim 100\,\mathrm{nm}$, as demonstrated by the experimental implementations.

TPE-STED at longer wavelengths To reach deeper regions in the sample, longer wavelengths are required, both for the excitation and the depletion beams. Molecules emitting in the red/NIR window would also prove useful, given the lower absorption of the emitted signal. We will from now on refer to this specific implementation as the "longer wavelength" TPE-STED (LWTPE-STED) microscope.

The first drawback of the LW strategy is the low absorption probability

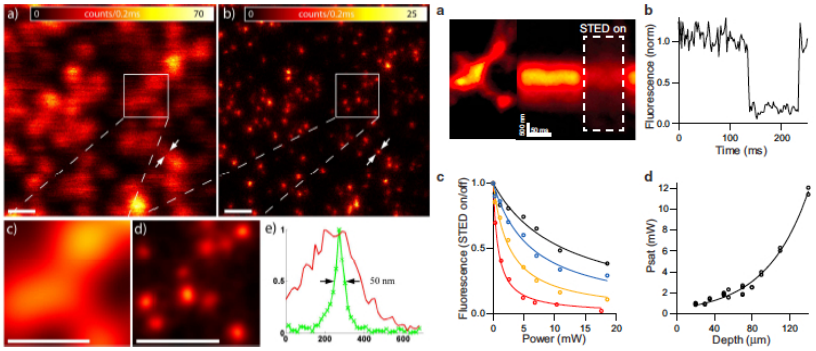

Figure 3.5: **[Left]** Comparison of TPE and TPE-STED images of 20 nm NileRed fluorescent beads mounted on a cover glass. (a) and (b) are, respectively, the raw pictures of TPE and TPE-STED. (c) and (d) shows linearly de-convolved enlargements of the areas marked with white squares in (a) and (b). All scale bars correspond to 500 nm. Normalized line profiles taken between the arrows in (a) and (b) are plotted in (e) in red and green, respectively. Adapted from [3]. **[Right]** Tissue penetration of depletion in acute brain slices. (a) TPE image of spiny dendrite (left) and fluorescence collected in linescan mode (right, along the dashed line). Pulsed STED light was simultaneously applied during the time period indicated (white dashed box). The vortex phase plate was withdrawn from the pulsed STED path to deplete the entire excitation volume. (b) Fluorescence averaged across the dendrite measured in linescan in panel a and normalized to the value before pulsed STED illumination. (c) Depletion efficiency versus pulsed STED laser power measured at 20 (red), 70 (yellow), 110 (blue), and 140 (black) μm deep. Data points were fit to rectangular hyperbolas to determine P_{sat}. (d) P_{sat} versus depth in slice. Data points were fit to an exponential to determine a surface constant ($P_{\text{sat}}(0) = 0.55\,\text{mW}$) and length constant ($\ell = 45\mu m$). Adapted from [4]

of the excitation light: as explained in Chapter 2, TPE is an efficient process when it involves the excitation of higher excited states, but shows a lower cross-section when the first excited state is involved, which is the case for wavelengths $> 1\mu m$. These low efficiency must be compensated, either with longer pixel dwell times (μs to ms [3, 4, 78]), or with high excitation intensities. In both cases, the photobleaching or the damage inflicted to the sample is increased. Lower pulse rates (0.25 MHz)[78] can be used to increase the amount of recovery and the overall fluorescence yield of the fluorophores, reducing also the power requirements of the system, but they also raise the lower limit reachable by the pixel dwell time. In general, when using ordinary fluorophores, a balance between bleaching/damage and acquisition speeds must be found. Only highly resistant red dyes can help surpass these compromises.

A second problem is given by the depletion beam itself, which increases the stress on the tissues and makes it necessary to reduce the overall exposure/pixel dwell time on the sample. In the specific case of longer wavelengths used to perform depletion, an additional issue must be faced, since the $700 - 800\,\text{nm}$ window brings an increased risk of two-photon excitation, even at the low intensities compared with the TPE light. near infrared (NIR) depletion wavelengths open a second excitation channel that can reach or even surpass the imaging signal level, drastically reducing the SNR of the image, and limiting the maximum STED intensity appliable to the sample (Figure.3.6). This is a known effect [79], which can be solved using longer stretching the STED pulse duration (hundreds ps): both TPE and depletion increase proportionally to the exposure time, but while the first follows the square of the pulse intensity, the second is still proportional to it. As the pulse is stretched, an increment of the SNR can be achieved without changes to the STED efficiency.

The ideal system where LWTPE-STED should be performed is then characterized by a high-power excitation source and/or a long pixel dwell time scanning head (the faster the scanning head, the stronger the excitation source). Low pulse repetitions are preferred, together with long ($> 100\,\text{ps}$) pulse durations. This preliminar preparation should also be accompained by a careful choice of the fluorescent molecules: to achieve proper super-resolution

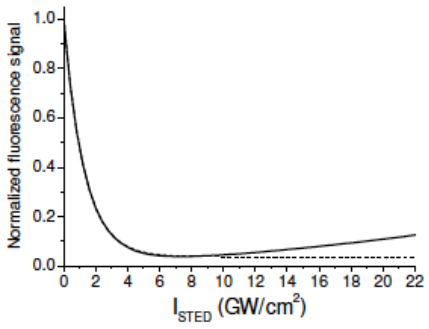

Figure 3.6: Example of interference between TPE and depletion for high STED intensities. If the TPE cross-section of the depletion beam is not low enough, raising the intensity brings to the re-excitation of the previously depleted region. This is particularly true for single-wavelength setups, where part of a femtosecond pulse beam is directed to a stretching and modulation line in order to provide depletion. The graph shows the calculated fluorescence depletion as a function of STED beam intensity in a single wavelength scheme (solid line). The beginning of the curve was fitted by an exponential decay (dashed line). Adapted from [79].

at these longer wavelengths, strong excitation cross-sections at $\lambda > 1000\,\text{nm}$ and low cross-sections (both SPE and TPE) in the $700 - 800\,\text{nm}$ interval are required. Higher resistances to photodamage and bleaching are also required with high pulse rates. At the moment, just a few choices are available with this properties, e.g. fluorescent proteins mGarnet [80] and mGarnet2 [6], developed only in the last few years. The expectation is that a larger palette will become available in the near future, making easier to reach the higher SNR noises needed for LWTPE-STED.

A final note of warning must be stated: the expected resolution of a LWTPE-STED system is intrinsically lower than a regular STED (or even a TPE-STED) setups. This can be inferred by two main arguments, regarding the depletion wavelengths and the imaging depths. Assuming the same fluorescent tags used in TPE-STED will be used for LWTPE-STED, the longer depletion wavelengths will be farther from their emission peaks, meaning that the relative depletion efficiency will be lower and higher saturation intensities will characterize the process. As for the latter argument, given the current TPE-STED limitations due to absorption and aberrations, we can expect that, farther from the sample surface, the effective saturation intensity will still rise considerably, and the doughnut core will still be affected by scattered light. We can then expect a positive LWTPE-STED outcome at deep regions being marked by lower factors than those of TPE-STED.

Chapter 4

Spiral Phase Plates

4.1 Introduction

STED microscopy depends on the ability to manipulate the depletion beam intensity profile in a simple and precise way. Since its invention, the tools used to meet these requirements have been phase masks, thin optics with non-trivial surface morphology that change the wavefront shape of a coherent beam and generate the desired output by means of diffraction. As the phase change required to achieve this effect is usually limited to a few oscillation cycles of the incoming light, phase masks can be fabricated with thickness profiles of the order of a few wavelengths. At this scales, mask fabrication requires to borrow the tools and knowledge of the micro- and nano-electronic industry, more specifically the micro- and nanolithography techniques for resist patterning.

This chapter provides the fundamental concepts needed to understand how diffractive optics work, and in particular how spiral phase plates are able to generate doughnut beams, then it introduces the reader to the basics of micro- and nanofabrication, and to the workings of electron beam lithography (EBL), the technique used to fabricate the custom spiral phase masks for our STED microscope.

4.2 Light propagation in collimated beams

Electromagnetic waves are coupled oscillations of the electric and magnetic field obeying the vectorial wave equations:

$$\nabla^2 \vec{E} - \frac{n^2}{c^2}\frac{\partial^2 \vec{E}}{\partial t^2} = 0 \qquad , \qquad \nabla^2 \vec{B} - \frac{n^2}{c^2}\frac{\partial^2 \vec{B}}{\partial t^2} = 0 \tag{4.1}$$

where $\nabla^2 = \frac{\partial^2}{\partial x^2} + \frac{\partial^2}{\partial y^2} + \frac{\partial^2}{\partial z^2}$ is the Laplacian operator, n is the refractive index of the medium inside which the waves propagate, and c is the speed of light. Our interest is to describe the propagation of light in air or in a

homogeneous, isotropic medium, so that we can describe the wave dynamics using only one of the two fields (the electric field is usually chosen), and also we can use only one component of the field vector instead of all three. We will refer to this component using the notation $u(\vec{r}, t)$, where $\vec{r}$ indicates the three-dimensional space coordinates (x, y, z), and we can immediately express eq.4 in terms of only this variable:

$$\nabla^2 u - \frac{n^2}{c^2}\frac{\partial^2 u}{\partial t^2} = 0 \tag{4.2}$$

A simple solution of eq.4 is given by harmonically oscillating functions, the *monochromatic waves*:

$$u(\vec{r}, t) = a(\vec{r})\cos[\omega t + \varphi(\vec{r})] \tag{4.3}$$

where the ω parameter (*angular frequency*) is proportional to the frequency ν of the light ($\omega = 2\pi\nu$), while the *phase* $\varphi(\vec{r})$ gives us information of the relative change of the oscillation evolution at various positions. The surfaces where the $\varphi(\vec{r})$ is constant are called the *wavefronts*. Their gradient $\vec{\nabla}\varphi(\vec{r})$ is parallel to the wavefront's normal vector at the position $\vec{r}$. The gradient represents the direction where the phase change happens at the fastest rate.

A convenient strategy is to see eq.4 as the real part of the *complex wavefunction* $U(\vec{r}, t)$:

$$U(\vec{r}, t) = U(\vec{r})e^{i\omega t} \tag{4.4}$$

Using this notation, we can separate eq.4 in a spatial and a temporal equation:

$$\nabla^2 U + k^2 U = 0 \qquad , \qquad k = \frac{\omega n}{c} = \frac{2\pi n}{\lambda} \tag{4.5}$$

where k is called the *wavenumber*. The spatial equation is called *Helmotz equation*, and it gives a complete description of the spatial behaviour of a monochromatic wave in a homogeneous and isotropic medium.

When the gradient $\vec{\nabla}\varphi(\vec{r})$ is approximately parallel to the propagation axis (the *optical axis*), we say that the wave is *paraxial*. The simplest paraxial wave is a *plane* wave, $U(\vec{r}) = Ae^{-i\vec{k}\cdot\vec{r}}$, where the wavefronts are planes with constant amplitude, perpendicular to the propagation (*optical*) axis indicated by the *wavevector* $\vec{k}$. Paraxial waves can be imagined as plane waves with a slowly varying complex amplitude $A(\vec{r})$:

$$U(\vec{r}) = A(\vec{r})e^{-ikz} \quad , \quad \frac{\partial A(\vec{r})}{\partial z} \ll kA(\vec{r}) \tag{4.6}$$

where the inequality on the right explains the "slowly varying" requirement: on a scale comparable to one wavelength, the change in the amplitude must be much smaller than the amplitude itself. The same inequality stands for

the second order derivative $\partial^2 A/\partial z^2$, and we can use it to find a simpler approximation to eq.4.5, the *paraxial Helmotz equation*:

$$\left(\frac{\partial^2}{\partial x^2} + \frac{\partial^2}{\partial y^2}\right) A - 2ik\frac{\partial A}{\partial z} = 0 \tag{4.7}$$

An important family of solutions eq.4.7 is given by the Gaussian beams (Figure.4.1), which show an axial symmetry and are better expressed in cylindrical coordinates:

$$A(r,\phi,z) = A_0 \quad \frac{w_0}{w(z)} \quad \exp\left(-\frac{r^2}{w^2(z)}\right) \quad \exp\left(-ikz - ik\frac{r^2}{2R(z)} - i\zeta(z)\right) \tag{4.8}$$

where

$$w(z) = w_0\sqrt{1+\left(\frac{z}{z_0}\right)^2} \qquad \text{is the beam } 1/e^2 \text{ radius} \tag{4.9}$$

$$R(z) = z\left[1+\left(\frac{z_0}{z}\right)^2\right] \qquad \text{is the wavefront radius of curvature} \tag{4.10}$$

$$\zeta(z) = \tan^{-1}\left(\frac{z}{z_0}\right) \qquad \text{is called Gouy phase} \tag{4.11}$$

$$w_0 = \sqrt{\frac{\lambda z_0}{\pi}} \tag{4.12}$$

w_0 and z_0 indicate respectively the minimum radius of the beam, the "waist" radius (where the origin of the axial coordinates was set), and the "Rayleigh length", defined as $w(z_0) = \sqrt{2}w_0$. As eq.4.12 shows, the Rayleigh length is longer for broader beams. Eq.4.10 shows also that the wavefronts are planar on the waist (infinite radius of curvature) and approximately spherical when $z \gg z_0$ ($R(z) \simeq z$).

Laser systems generate Gaussian beams. They are particularly well indicated for a diverse variety of applications, mainly due to the fact that their profile keeps its Gaussian shape along all the beam path, though with an increasing diameter. This property stands also for Gaussian profiles with polynomials multipliers, which means that many families of Gaussian beams are actually available. One family is particularly useful in the context of microscopy, as it mantains an axial symmetry that suits well the optical system, are the *Laguerre-Gaussian* beams (Figure.4.2):

$$\begin{aligned}\mathrm{LG}_{\ell,p}(r,\phi,z) = A_{\ell,p}\left(\frac{w_0}{w(z)}\right)\left(\frac{r}{w(z)}\right)^{|\ell|} L_p^{\ell}\left(\frac{2r^2}{w^2(z)}\right)\exp\left(-\frac{r^2}{w^2(z)}\right)\times \\ \times\exp\left(-ikz - ik\frac{r^2}{2R(z)} - i(|\ell|+2p+1)\zeta(z)\right)\exp(-i\ell\phi)\end{aligned} \tag{4.13}$$

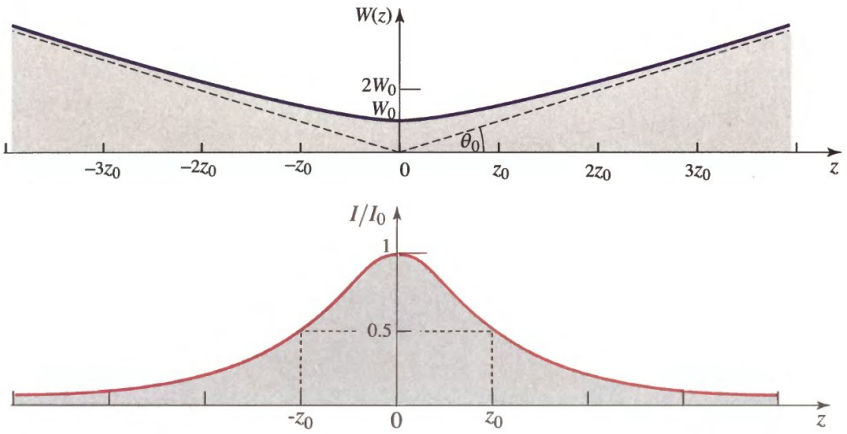

Figure 4.1: Graphical representation of the Gaussian beam. **Top)** Beam geometrical profile and **Bottom)** beam intensity along the direction of propagation. Adapted from [81].

where the generalized Laguerre polynomials L_p^ℓ are used as multipliers. The p parameter, which indicates the degree of the polynomial, influences the radial profile of the beam, which developes $(p+1)$ lobes separated by p nodes. The ℓ parameter influences the wavefront geometry, as the phase $\left(kz - k\frac{r^2}{2R(z)} - i(|\ell|+2p+1)\zeta(z) - \ell\phi\right)$ has a constant value over helicoidal surfaces with ℓ lobes, centered on the optical axis. Since all the different phase wavefronts meet on the optical axis, the phase itself has not a definite value at $r = 0$, so that we find a *phase singularity*, more exactly an *optical vortex*. ℓ refers to the strength - *topological charge* - of the vortex, and corresponds to the number of times the phase changes by 2π around the optical axis.

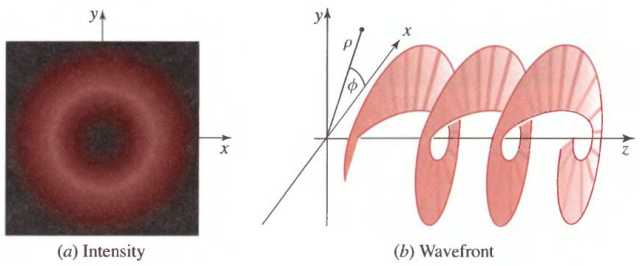

Figure 4.2: Representation of **(a)** the intensity profile and **(b)** the wavefront of a Laguerre-Gaussian beam of order $\ell \neq 0, p = 0$. Adapted from [81].

The lack of a definite phase value is not a physical possibility, as it contradicts the continuity of the electromagnetic field function, so the optical vortex should not exist. What happens, instead, is that for $\ell \neq 0$ the $r^{|\ell|}$ term brings the wave amplitude to zero, effectively "hiding" the singularity in a dark core.

4.3 Spiral Phase Plates

To generate a doughnut profile, a robust strategy is to use optical vortices, in particular Laguerre-Gaussian beams, since not only their singularity guarantees a perfect dark spot inside the beam, their intensity distribution is also invariant for propagation, except for a scaling factor that can be corrected with focusing optics. Dedicated optical resonators would be required, though, to provide these modes, so that an easier and more flexible solution is to use a Gaussian beam and add to the path an optical element for the generation of the optical vortex, a diffractive optical element (diffractive optical element (DOE)).

DOEs are optics that change the beam phase-amplitude distribution, so that upon propagation the desired profile is generated. The concept can be described in a straightforward manner: given a light beam that, at a starting plane $\Sigma_0 = \{(x, y, z)|z = 0\}$, can be described by the complex function $A(x, y, 0)$, the light distribution on a parallel plane (x', y', z) is given by the expression:

$$A(x', y', z) = \frac{i}{\lambda} \int_{\Sigma_0} A(x, y, z) \frac{\exp(-ikr(x, y, z))}{r(x, y, z)} dx' dy' \tag{4.14}$$

where $r(x, y, z) = \sqrt{(x - x')^2 + (y - y')^2 + z^2}$. The effect of a DOE on the beam field can be described by multiplication with a complex transmittance function, $T(x, y)$:

$$A(x', y', z) = \frac{i}{\lambda} \int_{\Sigma_0} A(x, y, z) T(x, y) \frac{\exp(-ikr(x, y, z))}{r(x, y, z)} dx' dy' \tag{4.15}$$

We see from eq.4.15 that the output light field will depending on both the starting field distribution and on the specific DOE used on the beam.

DOEs appear in many forms, each one with its advantages and its drawbacks, that make them ideal for different applications. Phase masks (or phase plates) are the simplest kind of DOE in terms of working principles and fabrication requirements: they consists of a thin layer of transparent material with a varying thickness profile. Light that travels through the mask experiences different optical paths, and emerges at different instants, and as a consequence its wavefronts are undergo a deformation that mirrors the surface morphology.

Given a mask with a thickness $H(x, y)$, perpendicular to the beam axis, the phase accumulated by the light at the further end of the layer ($H_{\max}$) will be proportional to the local optical path:

$$\varphi(x, y) = 2\pi \frac{nH(x, y) + n_{\text{medium}}(H_{\max} - H(x, y))}{\lambda}$$

where n and n_{medium} are the refractive index of the mask and the surrounding medium. Ignoring any constant phase terms, the complex transmittance of the mask can be expressed as:

$$T(x, y) = \exp(i\varphi(x, y)) = \exp\left(i\varphi_0 + i\,\frac{\Delta n\, H(x, y)}{\lambda}\right) \approx \exp\left(i\,\frac{\Delta n\, H(x, y)}{\lambda}\right) \tag{4.16}$$

where $\Delta n = n - n_{\text{medium}}$. The complex function in eq.4.16 has unit norm, meaning that it DOEs not affect the beam intensity profile. This is a strong advantage when power transmission and aberration minimization are required, which is usually the case for imaging systems.

Spiral phase masks, spiral phase plate (SPP)s, generate optical vortices of strength ℓ by means of their helicoidal thickness profile:

$$H(x, y) = h_0 + h\frac{\ell\phi}{2\pi} \qquad , \qquad h = \frac{\lambda}{\Delta n}$$

which gives the beam a phase proportional to the azimuthal angle. At $\phi = 2\pi$, the helical ramp ends with a vertical step, whose height can be coupled only with the design wavelength λ.

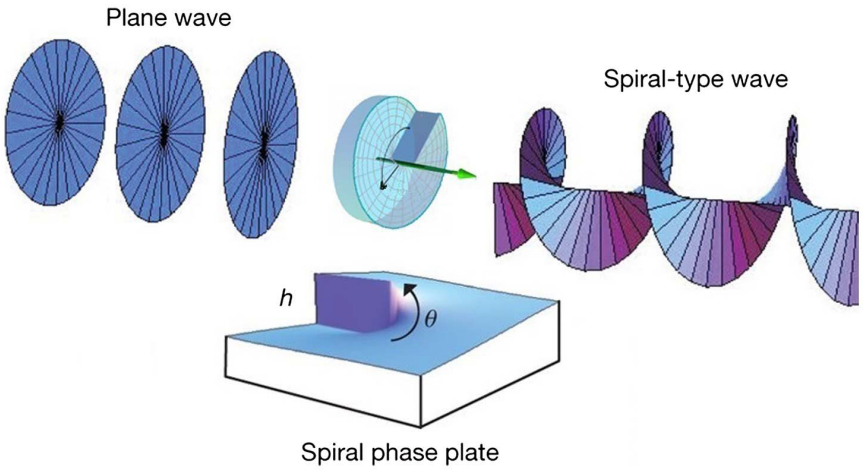

Figure 4.3: Model of a SPP: the helicoidal profile has a thickness profile proportional to the azimuthal angle θ around the center. The step has a height $h = \frac{\lambda}{\Delta n}$. Adapted from [82].

Achromatic SPPs can be fabricated, though they require two layers of materials with different refractive index, which need also to change differently with the wavelength, so that the preferred strategy is to just provide sets of plates designed for different wavelengths.

SPPs generate optical vortices, but their output DOEs not follow a Laguerre-Gaussian intensity profile. The far-field output generated by a Gaussian beam that meets a SPP on its waist is a Kummer beam, whose field distribution is proportional to a Kummer's confluent hypergeometric function, $M(\alpha, \beta, x)$:

$$A(r,\phi,z) = A_0 \left(\frac{r}{w_f}\right)^{|\ell|} M\left(\frac{\ell}{2}, \ell+1, \frac{r^2}{w_f^2}\right) \exp\left(-\frac{r^2}{w_f^2}\right) \exp(i\ell\phi)$$

Where $w_f = \frac{\lambda f}{\pi w_0}$ is the waist parameter of the doughnut. An alternative analytical expression can be found, in terms of Bessel functions:

$$A(r,\phi,z) = A_0 \left(\frac{r}{w_f}\right) \left[I_{\frac{\ell-1}{2}}\left(\frac{r^2}{2w_f^2}\right) - I_{\frac{\ell+1}{2}}\left(\frac{r^2}{2w_f^2}\right)\right] \exp\left(-\frac{r^2}{2w_f^2}\right) \exp(i\ell\phi) \tag{4.17}$$

The profile is shown in Fig.4.4: compared to the LG_0^ℓ modes, where maximum intensity is found on a ring with radius $r_{\max} \propto w_f|\ell|^{1/2}$, Kummer beams have larger rings, with radii following an approximately linear dependecy on the parameter ℓ $\left(\frac{r_{\max}}{w_f} \approx 0.47|\ell|+0.39\right)$. Additionally, while LG modes possess an exponential tail, Kummer beams follow an asymptotic inverse square law, so that they confine less their intensity.

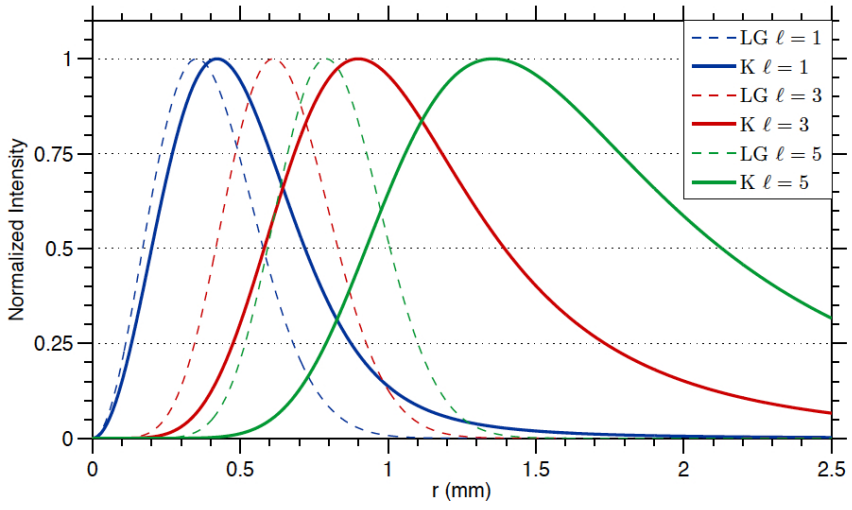

Figure 4.4: Comparison of Kummer (K, continuous lines) and Laguerre-Gaussian beams (LG, dashed lines) with equal ℓ values. Adapted from [83].

This is something that must be taken into consideration when focusing the doughnut with a microscope objective: as the best resolution is achieved when the back aperture of the lens is completely filled (*overfilling*), but still with an small enough beam to direct most of the beam energy inside the optics, a Kummer beam, whose tail transports a significant fraction of the total energy, must be smaller than the aperture radius.

4.3 Micro-/Nano-lithography

At the heart of modern electronic fabrication lies the ability to transfer specific patterns over flat multilayer films. The techniques developed for this purpose share this characteristic with the old lithographic techniques used to print journals and magazines, so they inherited the name, though exploiting entirely different physical principles. The most common micro- and nano-lithographic techniques can be divided in three main families:

- Optical lithography. Pattern is transferred using the interaction between the target film and a strong optical radiation (visible, UV or X-ray) that induces changes in the material composition or molecular arrangement
- Charged particle lithography. A focused beam of charged particles is used to change the physical and chemical properties of the target film
- Imprint lithography. Mechanical patterning is used, followed by a curing phase involving high temperatures or strong radiations.

Each of these techniques has a particular advantage over the others, so that they are all used in different context, with different purposes, depending on the speed, the resolution, the cost and the throughput required for the process.

Except for the specific technique used, the lithographic process follows a remarkably generalizable workflow, mainly regarding the preparation and the treatment of the material involved in the pattern trasfer. Common terms and metric were then introduced, and they constitute a widely spread knowledge around the world.

Resist deposition

The fundamental concept of this common terminology is the resist. This term encompasses all the materials that, by means of the lithographic process, change some of their physical/chemical properties in a way that allows to transfer a pattern on a thin film. Almost all of the resists consists of polymers made of long chains that, following irradiation with an energy source, are broken or cross-linked, changing their solubility to a specific chemical attack (development). A positive resist will become weaker to development in the interaction sites, and will then be removed from the pattern path, whereas a negative resist will see its resistance increased, being removed everywhere except for where the lithographic

process took place. From now on we will refer explicitly to positive resists, but the same terms and principles apply to the other case as well. At the beginning of a lithographic process the resist, immersed in a casting solvent, is coated on a substrate (glass slides, silicon wafers, metallic or insulating surfaces) by means of spin coating: the resist is deposited on the substrate, which is then spinned at high speeds. The generated centrifugal forces disperse the resist radially from the axis of rotation, so that after the solvent evaporation a thin flat layer is left, with a thickness depending on the coating surface tension and viscosity. The final thickness (t) can be controlled changing the rotation speed (ω, in rotations per meters, rpm), following the expression:

$$t = \frac{KC^{\beta}\eta^{\gamma}}{\omega^{\alpha}}$$

where C is the polymer concentration in grams per 100 ml solution, η is the intrinsic resist viscosity and the K, α, β and γ parameters must set experimentally with calibration measurements. Given a fixed coating area, a uniform film can be obtained if the rotation speed is high enough to let the resist cover the entire surface before solvent evaporation, but still low enough to avoid vibrations of the rotating support and air turbulence. Coating dishomogeneities can also be caused by low amount of initial resist, air bubbles not properly removed, or by particles present on the substrate surface before spinning. Immediately after spinning, the sample is baked for a short amount of time, in order to remove the residual solvent, and slowly cooled down to avoid stresses.

Pattern generation

The thin resist layer is then exposed with a radiation pattern, which changes the material solubility. The most fundamental metric in this regards is the dose, which quantifies the amount of action imposed on the resist: light irradiation is measured by the amount of energy absorbed, expressed typically in μJ, while for charged particle beams the amount of charge is preferred, expressed in μC. For two-dimensional pattern transfer, the dose per unit area (in $\mu J/\mathrm{cm}^2$ $-\mu C/\mathrm{cm}^2$) is the standard metric.

Depending on the writing strategy, we can differentiate lithographic techniques in the serial and parallel categories: the former involve the sequential exposure of single pattern elements, which makes them too slow for commercial purposes, but gives them flexibility (the only requirement is that the pattern can be described in a CAD file), the latter are faster, requiring only few one-shot exposures, but they depend on pre-patterned masks that require long fabrication times, falling short in terms of flexibility. Particle beam lithography is a common serial technique, where a sub-micrometric spot is exposed in a raster scan fashion over the sample;

a parallel strategy is instead followed by the majority of optical and imprinting lithography techniques. Similarly to microscopy, the resolution achieveable by a specific technique or machine can be expressed by means of a PSF, which expresses the distribution of the energy imparted to the resist around the desired exposure spot.

Resist development

After exposure, a chemical agent - called *developer* - is used, which attacks the resist pattern at a constant rate, dependent on the polymer solubility. Since the previous exposure step increased the local solubility of the resist by an amount dependent on the applied dose, the effect is that of a selective remotion of the layer in the patterned regions. To experimentally characterize the process, the residual layer thickness for different exposure doses (the *contrast curve*) is used, as shown in Figure.4.5.

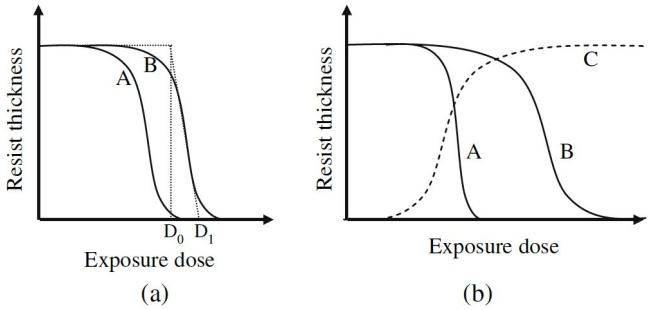

Figure 4.5: Representation of different contrast curves: **(a)** curves for resists with different sensitivities (A more sensitive than B), **(b)** curves for resists with different contrasts (A has higher contrast than B) and for different tones of the resist (A and B are positive resists, while C is a negative resist). Adapted from [84]

This simple visualization condenses in a single plot many different parameters regarding the resist (composition, phase, substrate), the developer (chemical formula, development time, temperature), the exposure process, and even the pattern geometry and dimensions. Usually, the contrast curve is acquired exposing small squares at different doses (*dose metrics*) and measuring the corresponding layer thickness. The normalized residual thickness is usually shown, in order to provide general informations independent on the experimental layer, and the dose are given on a logarithm scale. The two most important metrics that can be extracted from the contrast curve of a process are its *sensitivity* and its *contrast*. Sensitivity is expressed as the minimum dose required to completely consume the layer (*clearing dose*, D_1), gives us information on the amount of energy (or the time) required to pattern the resist. The contrast is

quantified by the slope of the curve:

$$\gamma = \frac{1}{\log_{10}(D_1/D_0)}$$

where D_0 is the minimum dose at which the resist starts to be consumed, and it gives an indication of how sensitive the process is to changes in the applied dose. In particular, contrast is linked to the capability of rendering vertical walls and binary structures from a continuous PSF slope, making it a necessary - though not sufficient - condition to generate high resolution patterns. To generate continuous three-dimensional structures, instead, a low contrast is required, as it gives a greater control on the resist thickness, also reducing the effects of the dose discretization imposed by some lithographic instruments.

The wide diffusion of lithography in the electronic industry is due to its versatility in many different fabrication scenarios: apart from situations where the aim is exactly the generation of a pattern on a resist film, the real strength of lithography is shown when the pattern transfered on the resist is replicated on the substrate or on other materials that would be difficult - if not impossible - to process in a direct manner. In these cases the lithographic process itself is a step in the actual fabrication process, where it is followed by a pattern replication phase that can take advantage of subtractive (*etching*) or additive (*liftoff*) techniques. These processes don't apply to three-dimensional fabrication of continuous reliefs, though, and won't be described in detail.

4.4 Electron Beam Lithography

Electron beam lithography (EBL) is a serial lithographic technique that uses a focused beam of highly energetic electrons ($1 - 100\,\mathrm{keV}$), quickly scanned over the sample, to change the resist properties. Charged beams have an important role in nanofabrication because they can be focused into extremely small probes using sophisticated instuments that, given the analogy with light focusing, are called charged particle optics. Modern instruments can focus the particles in a spot only a few nanometers wide, which helps to provide extremely high resolution patterns. Being a serial technique, where a single beam is sweeped over the pattern area, the corresponding throughput is extremely slow, as millimeter-sized fields require hours, if not days, to be exposed.

In an EBL system, the beam acceleration and the scanning of the focused spot are performed by a complex apparatus - the *optical column* (Figure.4.6) -, which consists of (1) an electron source for the generation of the beam, (2) a series of electromagnetic lenses to focus the beam on the sample, and (3) an electromagnetic deflection unit that scans the beam during the exposure.

All of these components need to work in high vacuum, at pressures on the order of $10^{-8} - 10^{-10}$ Pa, to avoid collisions between the travelling electrons and the gas atoms.

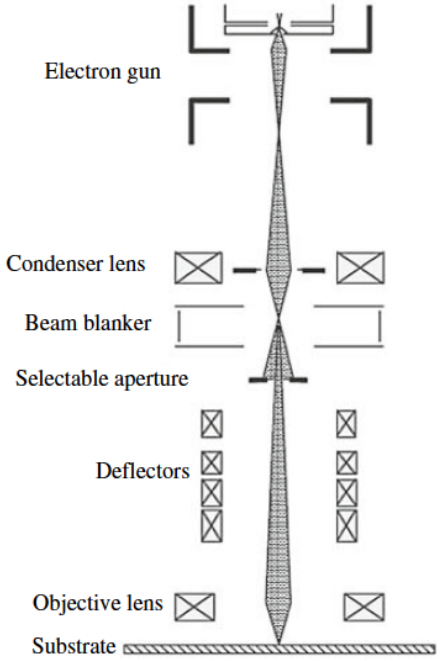

Figure 4.6: Schematic representation of the optical column of an EBL machine. Adapted from [85]

(1) Electron sources

Electron sources, or "guns", generate and accelerate the electron beam to tens-to-hundreds keV. They extract electrons from a metallic electrode and accelerate the particles with strong electric fields. Electrons are confined inside the metals by a potential barrier, which can be overcome either injecting thermal energy into the system, or reducing the potential well depth with opposing electric fields. Depending on which of the two strategies is employed, we distinguish between thermoionic emission and field emission guns. In the former case, the electrode is traversed by a high electrical current, which heats it to tempeatures high enough ($\sim 2000K$) to expel electrons from the metal. Large electrodes are required to sustain the heating currents, consequently thermoionic sources are characterized by large emission areas and stable, high-current ($\sim 1\mu A$) beams. As a drawback, they have a wide angular spread, that influences the minimum size of the focused spot. Field emission sources use strong electric fields ($> 10^8 V/m$) applied to a sharp metallic tip, in order to lower

the energy cost of electron extraction. They provide lower beam currents ($\leq 1\,\mathrm{nA}$), with the advantage of a lower Coulomb repulsion between the beam electrons, so that a narrower spot can be focused on the resist. For this reason, they are the standard choice for high-resolution electron microscopes. They are not used in nanofabrication systems, though, as they are strongly affected by the absorption of gaseous atoms on the emission surface, which causes a strong current noise and drift. These problems were solved with the development of thermal field emission (Schottky) sources: they consist of a tungsten tip coated with a layer of zirconium oxide, which is both heated to $1800K$ and exposed to strong electric field, in order to provide a stable current over the resist, and a nanometer-sized spot.

(2) Electron optics

The optical column provides focusing of the electron beam by means of electromagnetic lenses. Electromagnetic lenses show many analogies with optical lenses, as it is possible to introduce an electromagnetic "refractive index" to describe their effect on the electrons. The main difference in this regard is given by the fact that the electromagnetic refractive index follows the electric/magnetic field intensity, and cannot display any discontinuity like the optical analogue. An additional difference is given by the fact that magnetic lenses provide an additional rotational motion to the electrons around the beam axis, and that they provide different focusing to particles of different mass. While this characteristic is an obstacle to the use of magnetic lenses in ion beam focusing, it DOEs not constitute a problem for electron beam focusing, so that they are largely used for the strong magnetic fields they are able to provide. Simple electron beam systems will still use electric lenses, though, given their simpler design. The simplest kind is given by round lenses, which provide symmetrical focusing, but are affected by the common aberrations of optical analogues (spherical, chromatic, astigmatism). Aberrations can be corrected either reducing the focusing angle of the beam, or using quadrupole and multipole lenses, whose higher complexity provides a greater number of parameters on which to operate. Reducing the beam divergence is a common strategy, given the fact that both geometrical and chromatic aberrations increase nonlinearly with the focusing angle. This strategy finds a limit in the diffraction and Coulomb repulsion, which provide a significant contribution to the spot diameter on the focal plane and whose influence is stronger in more collimated beams.

(3) Deflection optics

Aberrations are exasperated by beam offsets respect to the column optical axis. The deflection of the beam, which is provided by electric deflectors before the objective lens, must then have a limited spanning range. Common systems never use deflections greater than 1 mm, using

mechanical translation of the target to provide wider exposure fields. A common strategy is also the combined use of two deflection systems, one for wide, slow changes of the beam position, and the other for small, fast subfield scanning. The advantage is given by the ability to expose only the regions where the pattern actually covers the field, together with a smaller positioning error compared to single-deflection systems operating on the same field width.

Electron-resist interactions and resolution High-energy electrons penetrating into a solid material will collide with atom nuclei and the electrons surrounding them. Two main scattering processes can happen, depending on the energy exchanged between the scattering particles: elastic processes, involving electrons and atoms nuclei and where no transfer of energy, only a change in the trajectory direction, and inelastic collisions between electrons, where energy is transferred to the electronic shell of the atoms. The electronic deflection depends strongly on the atomic number (Z) of the nuclei involved, as the expression of the cross-section shows:

$$\sigma(V,\theta) = \frac{Z^2}{16}\frac{1}{V^2}\frac{1}{\sin^4(\theta/2)}$$

Where V is the acceleration voltage of the optical column and θ is the deflection angle. Even though the vast majority of the collisions results in a small angle of deflection, as the $\sin^{-4}$proportionality suggests, the probability of a backscattering event ($\theta > 90°$) increases drastically for heavier elements, which are usually found on the substrate. While small angle deflections have a limited effect on the final resolution, providing a simple blurring effect far below 100 nm, backscattered electrons are able to travel μm away from the exposure spot, interacting with the resist in a large area and influlencing the exposure of dense pattern structures (*proximity effect*). As the electron travel in the resist, they collide with shell electrons, stripping them from the molecules. These *secondary electrons* are the reason of the resist exposure, and though they contribute to the PSF blurring by about 10 nm [86], they are unavoidable. The rate at which both primary and secondary electrons transfer their energy to the resist is expressed by Block's formula:

$$\frac{\mathrm{dE}}{\mathrm{dt}} = -7.85 \cdot 10^4 \frac{\rho Z}{A}\frac{1}{E}\ln\left(\frac{1.66E}{J}\right)\left[\frac{\mathrm{keV}}{\mathrm{cm}}\right]$$

where ρ is the resist density, A and J are respectively the atomic weight and the ionization potential of the resist molecules. We see from the E^{-1} term that more energetic particles transfer less energy to the resist, which means higher doses are required, when compared with less energetic bams. The PSF of the resist exposure, which describes the total effect of secondary electrons and forward-/backward-scattered primary electrons on the exposure resolution, can be approximated by a sum of gaussians with different

amplitudes and widths: the blur caused by forward-scattered primary electrons and secondary electron can be described with a high, but narrow, peak, while the backscattered electrons provide a weaker, but broader effect, that must be modeled with a short wide Gaussian. The best approximations are expressed as three-term additions:

$$\mathrm{PSF}(r) = \frac{e^{-\alpha r^2} + \nu e^{-\beta r^2} + \eta e^{-\gamma r^2}}{1 + \nu + \eta}$$

where the second term expresses "medium" range interactions concerning both primary and secondary electrons. The final dose distribution will be given by the convolution between the nominal dose pattern and the PSF function, and applying the contrast curve function to this result will give a prediction of the final pattern geometry. In order to achieve the closest correspondence between the fabricated and the desired pattern shape, the effect of electron scattering must be factored before the exposure step: the nominal doses must be administered in a manner which allows to compensate the dose dispersion from isolated features and the proximity effect in dense patterns. This correction step is called proximity effect correction (PEC), and can be performed by a variety of softwares, which use PSF models derived from numerical or experimental [87] investigations.

3D-EBL Micro- and nanolithographic techniques were initially developed for the generation of binary patterns in thin layers, which met the needs of the microelectronic industry. The process had to be engineered in order to provide vertical walls and densely packed features, so that resists had to have low sensitivities to reduce the influence of the proximity effect and high contrast to sharpen the smooth dose distribution that PEC wasn't able to compensate. These requirements don't translate to the fabrication of three-dimensional profiles, were the aim is the precise control of the resist residual thickness. 3D lithographic processes require low-contrast resists, in order to minimize the effects of dose discretization and exposure variations on the final layer thickness. High sensitivities are best coupled to wide, continuous geometries, where lower exposure times are useful and proximity effects help smoothen out the geometrical pattern of the beam raster scan, while higher clearing doses provide advantages when steps and thin, vertical features are requested, since they reduce the influence of the proximity effect.

Chapter 5

Microscope Setup and Experimental Methods

5.1 Introduction

The following chapter presents a detailed description of the experimental setup of the microscope and its configurations, and describes the protocols used to prepare the samples that were used in calibration tests and biological studies, and the procedures followed for the analysis of the data acquired. The optical path of the microscope is presented in paragraph 3.2, while the protocols and procedure are shown in paragraph 3.3.

5.2 Microscope

The microscope setup, based on a upright design, is described in Figure 5.1.: the objective (Olympus XLPLN25XWMP2, 1.05 NA for *in-vivo* experiments, LUMFLN60XW, 1.1 NA for high-resolution cell culture imaging and UPLSAPO100XO, 1.4 NA for STED imaging) and the scanning system are mounted on a vertically-translating head, while the sample holder is mounted on a 2D translation stage. The fluorescence light is collected by an epi-detection system with four photomultiplicator (PMT) modules (Hamamatsu, H7422-40), each with its own bandpass filter for channel acquisition (Table 5.1.), whereas the transmitted intensity can be collected by a condenser lens (Nikon, D-CUO Achr-Apl, 1.4 NA) and directed to a trans-detection sensor (biased InGaAs photodetector, DET20C, Thorlabs).

The objective-condenser scheme also works as a wide-field imaging system, illuminated by two LED lamps (MWWHL4 and M660L3, Thorlabs) and ending on a trinocular system placed on the microscope head. Separation between wide-field and scanning mode is provided by the primary mirror on top of the objective mount, which can be translated back and fort,

Figure 5.1: Microscope head, stage and detection modules

	Channel A	**Channel B**	**Channel C**	**Channel D**
$\lambda/\Delta\lambda$ (nm/nm)	395/25	460/50	525/40	625/90

Table 5.1: Wavelength detection range of the PMT modules. The fluorescent light is directed on the modules by a dichroic mirror (long-pass, 705nm cutoff wavelength, Semrock), then divided in different channels by long-pass and short-pass mirrors (Semrock).

blocking one path at a time.

The two excitation beams are generated by an OPO system (APE, Germany), pumped by a Ti:Sapphire laser (Chameleon Ultra II, Coherent Inc., Santa Clara, CA, USA), which generates a 4W beam with wavelength tunable between 700 nm and 900 nm. The OPO generate a beam with wavelength tunable between 1000 nm and 1600 nm, and can release a fraction of the pump intensity as a second independent beam.

The beam pulses have a 140 fs duration, and exit from the OPO already synchronized, with a 6 ns delay. Such a system was thought to avoid the use of expensive electronic control circuits between different lasers, in favour of mechanical delay regulation by means of a cheaper motorized translation stage.

The beams intensity is regulated by electro-optical devices known as Pockels cells (models 360-80 and 350-80, Conoptics, Figure 5.2.), made of crystals that, once immersed in a constant electric field, acquire a voltage-dependent birefringence; the change in the state of polarization of the transmitted beam is then converted to an intensity modulation by means of an external polarizer. Such devices allow fast modulation of the transmitted intensity at frequencies as high as 100 kHz , which allows in-line control of the pixel intensity. The pump beam transmitted by the Pockels cell passes through an optical isolator (IO-5-NIR-LP, Thorlabs inc) and a half-wave plate (AHWP05M-600, Thorlabs), then is directed to a bifurcation, where a removable mirror can be introduced to lead the light to the stretching line required in order to achieve STED super-resolution.

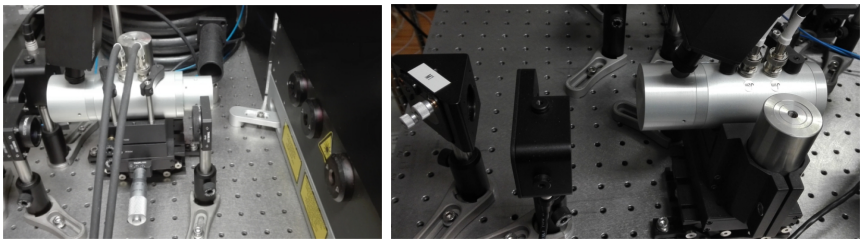

Figure 5.2: Pockels cell used to modulate the intensity of the pump (left) and OPO (right) beam

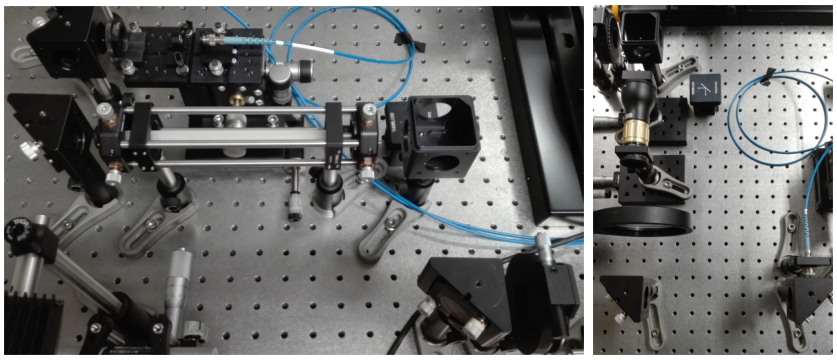

Figure 5.3: (Left) Stretching line: glass rod (bottom) and optical fiber (top); (Right) beam conditioning units: phase masks (bottom) and 3X beam expander (top).

Depletion requires pulses lasting tens or hundreds of picoseconds, generated by femtosecond-pulses by means of a 20 cm-long SF6 glass rod (Fuzhou Solid Photon Inc), which stretches the pulses to a few ps, and a $100m$ single-mode polarization-mantaining fiber (PM780-HP,Thorlabs), at the end of which the pulses exit with widths in the hundreds ps range (Figure.5.3). An aspheric lens (A280TMB, f = 18.4 mm, NA = 0.15, Thorlabs) couples the beam to the fiber, which is aligned by a 3-axis stage (MBT613D/M, Thorlabs) with micrometric precision.

The stretched pulses pass then through a spiral phase mask (VPP-1a, RPC Photonics Inc), which generates the doughnut intensity distribution, and a 3X telescope (#59-134, Edmund Optics), used to modify the convergence of the beam. The STED path joins the "femtosecond" path with a second removable mirror, after which a piezo-driven mirror redirects the light to the microscope.

In the OPO path, a motorized translator (LTS300/M,Thorlabs, Figure 5.4.), with 300 mm range and $0.1\mu m$ precision is used to change the relative delay between the OPO and pump pulses; then a 5X telescope (GBE05-C, Thorlabs) collimates the beam, which is directed to the microscope by a mirror-dichroic system that joins the ending tracts of the OPO and pump paths. Both the beams reach the microscope after passing through a half-wave plate (AHWP05M-600/-980, Thorlabs) and a quarter-wave plate each (AQWP05M-600/-980, Thorlabs), which give complete control over the polarization state before the objective.

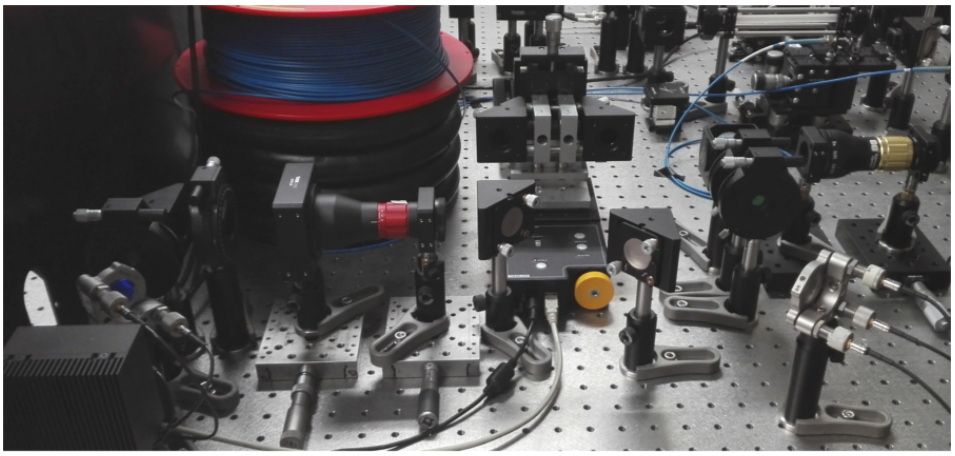

Figure 5.4: (Top image) Overview of the final parts of the STED and OPO paths

A short distance before the microscope body, a small fraction of the beams light is reflected to a fast InGaAs detector (DET08CL, Thorlabs, Figure 5.5.) connected to an oscilloscope, which allows to check the temporal separation between the OPO and pump pulses. Both the beams are then directed to the scanning mirrors (galvo/resonance system, 8kHz) by means of a periscope, finally meeting the scanning lens system (magnification 3X) and the objective lens.

The system, relying on the Thorlabs Bergamo series, was controlled by the native Thorimage LS software for multiphoton imaging. The scanning control was directed by a dedicated electronic control unit, while the data acquisition was performed by means of an ATS9440 waveform digitizer (AlazarTech,), with four 14-bit channels.

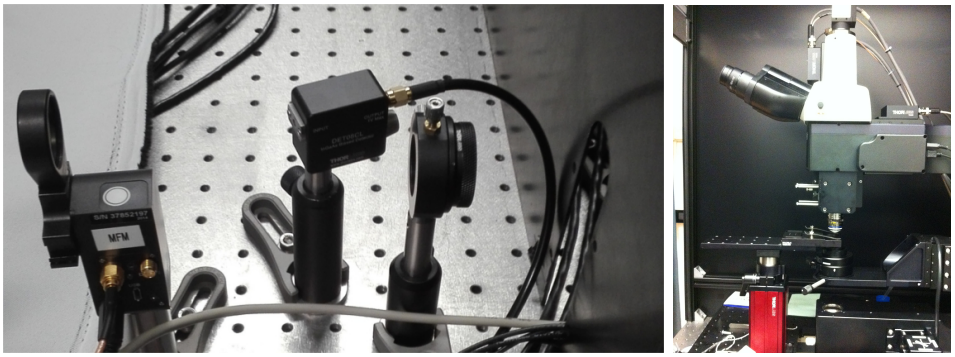

Figure 5.5: (Left) Fast InGaAs detector for the coarse measurement of the pulses delay, (Right) Lateral view of the microscope body

Size	Frame Rate	Pixel Size	Pixel Dwell Time
512×512	15 fps	8 nm (32X), 16 nm (16X)	32 ns
512×256	30 fps	8 nm (32X), 16 nm (16X)	32 ns
1024×1024	7.5 fps	128 nm (1X), 64 nm (2X),	16 ns
1024×256	30 fps	4 nm (32X), 8 nm (16X)	16 ns
1024×128	60 fps	4 nm (32X), 8 nm (16X)	16 ns

Table 5.2: Scanning properties of the images captured with the galvo-resonant mirror system of the microscope. The frame rate refers to the "one-way" scan option, where only the forward advancing line sweeped by the scan mirrors is considered to build the image. The pixel size is reported relative to the scanning magnification (which ranges from 0.6X to 32X of the backfocal plane aperture dimensions).

Table.5.2 provides a list of the scanning rates and resolutions of the principal acquisition modalities used in this thesis. The pulsed electronic synchronization signal from the pump laser, processed with a hand-made low-pass filter (kind concession from Luca Bacci of the Department of physics), was used to set the acquisition rate of the digitizer to the required 80 MHz.

5.3 Experimental methods and protocols

Measurements and analysis All the power measurements reported in the following chapter were measured using a Thorlabs PM100D console connected to a S305C thermal sensor. Single measurements are given a 0.1 mW uncertainty for measurements concerning the power of the pump beam, 0.5 mW for the OPO beam. The power values reported in the graphs of the excitation efficiency tests at different wavelengths, and during the depletion efficiency tests, are the average values of 50 fast measurements averaged over 1s each. The reported uncertainty is given by the standard deviation of the set.

Polarizations were measured using a Schafter+Kirchhoff SK010PA-NIR polarization analyzer. The degree of polarization used in all the experiments was always higher than 95%. For STED tests, in particular, the degree of polarization was checked and adjusted with the polarizer before the SPPs, in order to have values higher than 98% on the objective back aperture.

Test sample preparation The gold beads samples for the assessment of the doughnut quality and the diamond nanocrystals for STED tests were prepared by mixing the water suspension with the mounting medium (Mowiol-88), then pouring $5\mu L$ of the mix on a glass slide and covering with a coverslip. The GATTAquant beads sample was bought ready-to-use. The beads had a diameter of 20 nm and were immersed in polyglicole. The KDP mi-

croscrystals were mashed in a mortar, placed on a glass slide and covered with a coverslip without any mounting medium.

Cellular samples We used two cell lines for our samples: HeLa cells and mouse embryonic fibroblasts (MEF). HeLa cells have the advantage of being immortalized, and to be able to survive indefinitely outside the human body. Their main strength lies in the simplicity and rapidity of their preparation, which takes less than a week to be prepared and has a high margin of success.

MEF cells are often used as a model for studies of staminal growth and differentiation. They are an ideal test target to observe super-resolution: the intricate tubular network inside their cytoplasm can be stained both with immunostaining (like the Alexa and ATTO fluorophore families) and with fluorescent proteins (in particular molecules that fuse with the RITA protein[88], that binds to tubulin in the cytoplasm from where it shuttles the RBP-J/CBF-1 trascription factor to and from the nucleus), and provides many details at sub-micrometer scales that STED imaging can reveal.

Both cells lines were maintained in Standard Medium (89% DMEM, 10% FBS, 1% Pen/Strep 100X) in T25 or T75 Corning flasks. At approximately 80% confluence, the culture medium was removed and dead cells and serum were washed away with PBS 1X. Cells were detached from the flask with the addition of 1 mL of 0.25% Trypsin in EDTA and a 3-minutes incubation at 37 °C. 3mL of Standard Medium were added to block trypsinization, then the cells were spun at 1250 rpm for 5 minutes and resuspended in 4mL fresh medium. Cells were seeded on the coverslips at $\sim 125\,\text{cells/mm}^2$ density, inside a 6-well plate (BD Falcon). A 1:10 dilution was plated in a new flask for cell line expansion.

Plasmid trasfection Transfection is the process by which specific parts of genetic material are introduced into the cells. Cell lines trasfection uses liposomes, lipid vescicles that fuse with the cellular membrane and deliver the DNA they contain inside the cell.

Before trasfection, a mix of $5\mu L$ Lipofectamine2000 (LifeTechnologies) and $245\mu L$ Optimem (LifeTechnologies) and a dilution of $3\mu g$ of DNA in $250\mu L$ of Optimem were prepared for each cell coverslip and left for 5 minutes at room temperature, then mixed together and left at room temperature for 20 minutes. The cells were washed with PBS 1X, then $500\mu L$ of Optimem were added, followed by the trasfection dilution, and the plate was left 4 hours in the incubator at 37 °C. After incubation, the trasfection dilution was removed, and Standard Medium was added.

Immunofluorescence staining Before staining, cells were fixed in 3.7% para-formaldehyde in PBS (v/v, SIGMA-Aldrich) for 30 minutes at 4 °C. The solution was then removed and the coverslip washed 3 times for 10 min-

utes in PBS 1X. Cells membrane permeabilization was performed applying a dilution of BSA (1%) and Triton-X (0.1%) in PBS 1X for 5 minutes at room temperature. After the dilution was removed (washed 3 times with PBS 1X for 5 minutes), the cells were incubated in a humidified chamber, with the primary antibody and BSA 1% in PBS 1X, 30 minutes, 37 °C. The same step was applied for incubation with the secondary antibody, followed by three other washes for 5 minutes and application of the fluorophore following the seller indications. Staining with dyes conjugated with secondary antibodies skipped secondary antibody incubation. Coverslips were then mounted with Mowiol-88 over a glass slide.

Heart cryosections Mice were sacrificed by cervical dislocation and hearts were quickly harvested and cut in two portions in the transverse direction and processed as described in [89]. Briefly, blood clots were carefully removed and the heart was fixed to maintain structural integrity with 1% paraformaldehyde in phosphate buffered saline (PBS 1X: 137 NaCl, 2.7 KCl, 10 $Na_2\,HPO_4$, 1.8 $KH_2\,PO_4$, in mM) at room temperature for 15 minutes. After 3 washes of 5 minutes with PBS 1X, hearts were allowed to dehydrate in sucrose 30% (w/v in distilled water) at 4 °C overnight. The following day, hearts were embedded in OCT freezing medium (Optimal Cutting Temperature, Kaltec) and carefully frozen in liquid nitrogen vapor. Frozen samples were maintained at −80 °C. Frozen hearts were cut in $10\mu m$ slices using a cryostat (Leica CM1850, Leica Microsystems GmbH, Wetzlar, Germany) and placed on superfrost glass slides (Vetrotecnica) maintained at −80 °C until use.

Gastrocnemius muscle and SDH staining Gastrocnemius muscles were harvested from mice and immediately frozen in liquid nitrogen. $10 - m$ cryosections were obtained with a cryostat (Leica CM1850, Leica Microsystems GmbH, Wetzlar, Germany) and stained for Succinate dehydrogenase (SDH). Processed cryosections were examined in a fluorescence microscope (Olympus BX60).

Ex-vivo lungs Mouse was sacrificed by cervical dislocation and lungs were quickly harvested and carefully washed in ice-cold PBS to avoid blood clotting. Lungs were then transferred on a petri dish filled with PBS. To prevent curling and movement, lungs were held down through a homemade platinum holder. Decellularized bovine pericardium. Bovine pericardia were collected from the local slaughterhouse and decellularized using a method based on alternated hypo- and hypertonic solutions, detergents (Triton X-100 and sodium cholate, Sigma-Aldrich, Saint Louis, MO, USA) and non-specific endonucleases (Benzonase, Sigma-Aldrich). Following the decellularization procedure, samples of $1\,cm^2$ were placed into plastic embedding

devices (Bio Optica, Milano, Italy) and covered by a thin layer of 4% low melting agarose solution prepared in PBS (Sigma-Aldrich).

Image processing and statistical analysis Prior to any analysis, the images were processed using the Matlab software: the environment and sensor background was eliminated subtracting a "dark" image acquired with both the laser shutters closed, and a gaussian filter with 1 px width was applied. All the intensity values derived from the samples photos are expressed in pixel units, and consist of the average of the 5% brighter pixels values of the image, with the standard deviation set as the correspondent uncertainty.

For correlation analysis, images were processed with Fiji using the ROI Manager plug-in in order to obtain mean ROI intensity and Area values. Pearson correlation coefficient was evaluated with OriginPro^{TM} 2016 and data were fitted with linear regression.

Chapter 6

Nonlinear Microscopy: experimental results

6.1 Introduction

Our setup, described in Chapter 5, is a tunable, dual-laser system for simultaneous nonlinear imaging, in particular for deep, *in vivo* imaging. The basic configuration comprises only the minimal path necessary for the co-alignment and the insertion of the laser beams in the scanning head of the microscope body, which make it particularly simple and easy to set up. *In vivo*, TPE studies on the ulcer of live mices were performed in order to understand the influence of diabetes on the healing ability of scar tissue. This work has been published in a paper from Fadini *et al.* [90], and it provides a demonstration of the TPE-SHG imaging capabilities of the 800 nm, single-beam configuration.

Dual-beam nonlinear imaging was tested on a number of unstained cryosections cut from mouse heart and lung. The work was published in a paper from Filippi *et al.* [91], where the label-free simultaneous autofluorescence TPE, SHG and THG imaging of nicotinamide adenine dinucleotide (NADH), collagen, and elastin is demonstrated, both in thin and thick ($\sim 200\mu m$) samples. This study shows how the dual-beam approach allows for simultaneous optimization of the signal from different features, giving brighter images with distinct, easily recognizable elements. The next paragraph exposes briefly the main results shown in [91], leaving to the reader the option to read from the original publication in detail.

The third paragraph describes the spatial and temporal alignment procedures needed to achieve two-color two-photon excitation (TCTPE). This nondegenerate nonlinear technique provides the ability to excite molecules in a third spectral window, $[900 - 1000]$ nm, that the dual-beam setup is not able to reach. Since this "virtual" excitation source intensity can be tuned independently from the other two, it takes even further the capabili-

ties of our platform. A demonstration of the broader reach allowed by this technique is given with the efficient imaging of green molecules outside the normal excitation scope of the microscope.

6.2 TPE and SHG imaging

In Figure.6.1 an example of TPE/HG imaging is shown, taken from Filippi *et al.* (2017) [91]: cardiac cryosections were imaged without prior staining, using both the pump and the OPO laser, tuned at respectively 800 nm and 1200 nm. The top-left panel shows the image taken with the pump beam, where theSHG signal from the white channels reveals the sarcomeres' myosin and collagen deposits sourrounding the coronary vessel. Illumination at 1200 nm (top-center panel) shows a red SHG signal from the same structures. Magnification of the sarcomeres (bottom-left panel) shows a clear image, with little to none background compared to the signal. An additional detail revealed by the images is the elastin protein, both its autofluorescence from 800 nm and its THG signal from 1200 nm.

The dual-laser label-free strategy does not only allow to collect more signal from the same structures, it also helps to reveal features with which

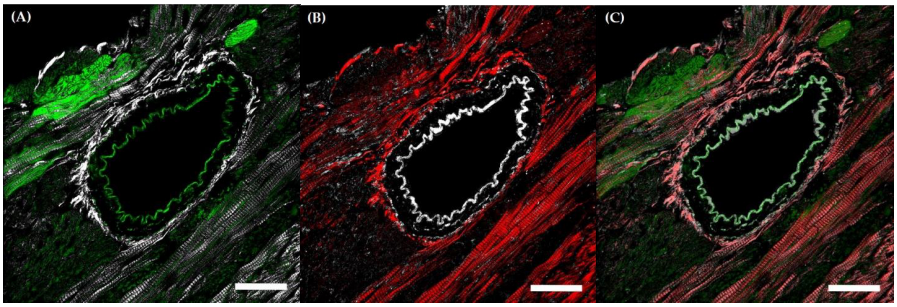

Figure 6.1: Simultaneous TPE and HG images of cardiac cryosections. **(A)** Cardiac cryosection imaged with 800 nm laser wavelength shows TPE autofluorescence (Green, $\lambda_{\text{em}} =\sim 500$ nm) and SHG signal (White, $\lambda_{\text{em}} =\sim 400$ nm). **(B)** Same field of view imaged with 1200 nm laser wavelength shows SHG (Red, $\lambda_{\text{em}} =\sim 600$ nm) and THG (White, $\lambda_{\text{em}} =\sim 400$ nm). **(C)** Superposition of the same field imaged with 800 nm and 1200 nm; The SHG produced by the two different laser beams, as well as the elastin autofluorescence and its THG signal, perfectly superimpose, testifying the excellent spatial alignment of the lasers. The auto-fluorescence excited with 800 nm also highlight some features that are not visible with an excitation wavelength of 1200 nm, proving the dual-laser imaging approach more information-rich than the common single-wavelength TPE. Scale bars $50\mu m$. From Filippi *et al.* [91].

one of the beams would be unable to interact: a strong TPE signal from NADH can be seen under 800 nm illumination, while being absent under the 1200 nm light. The fact that the NADH signal gives informations about the metabolic state of the highlighted cells means that it is possible to differentiate glycolytic and oxidative fibers with the same structural configuration.

This discriminative study was performed on skeletal muscle cryosections, as shown in Figure.6.2, where three consecutive muscle cryosections were observed using TPE-SHG (top-left panel), SDH staining (top-right panel) and Hematoxylin/Eosin staining (bottom-left panel). TPE and SDH signals show a strong correlation (bottom-right panel): stronger SDH activity is expected in oxidative fibers, together with a larger number of mithocondria, that implies a stronger NADH concentration and a stronger TPE autofluorescence.

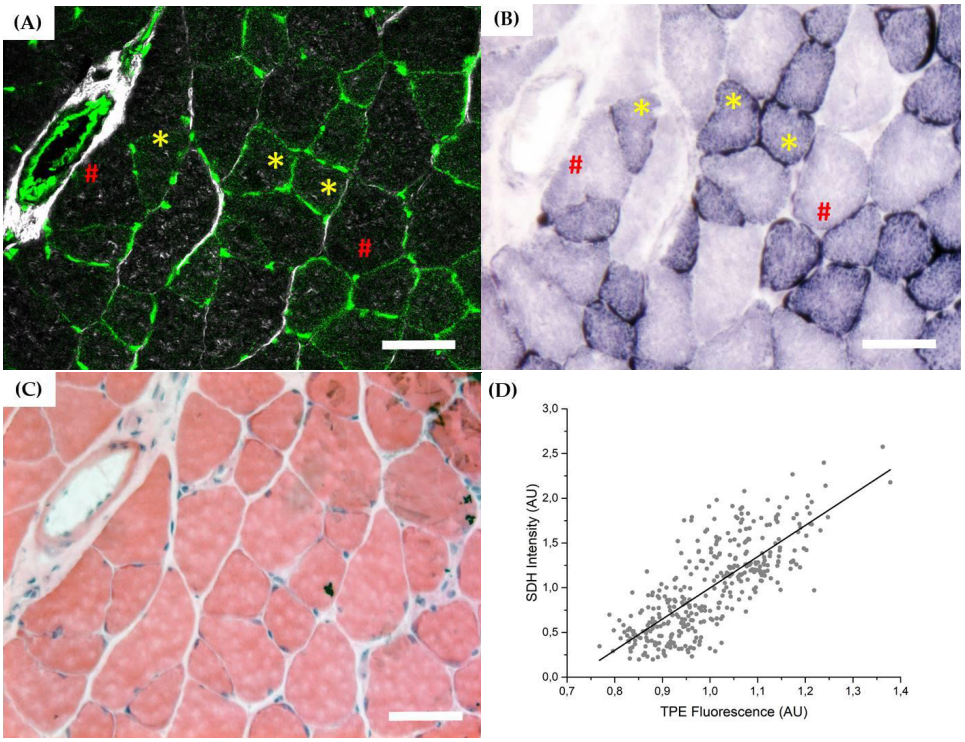

Figure 6.2: TPE of NADH in muscle cryosections. **(A)** TPE (Green) and SHG (White) signals from gastrocnemius muscles cryosection. **(B)** SDH staining of the consecutive cryosection from the same muscle. **(C)** Hematoxylin/Eosin staining of the consecutive cryosection from the same muscle. **(D)** Correlation analysis of TPE and SDH signal intensity from the same fiber (N = 4 cryosections, n= 350 fibers). Pearson correlation coefficient $P > 0.75$. Yellow (*) and red (#) highlight corresponding fibers, oxidative and glycolytic respectively. Scale bars $100\mu m$. From Filippi *et al.* [91].

This trend is confirmed by the experimental observations, that prove the validity of label-free TPE as a tool for NADH quantification. The collagen content of the cryosection was also imaged by means of both SHG and Hematoxylin/Eosin staining, with overlapping results, which validated the label-free approach to collagen imaging. To assess the *in vivo* and deep imaging capabilities of the label-free analysis performed with our setup, we started with the examination of thick, freshly excised unstained mouse lungs.

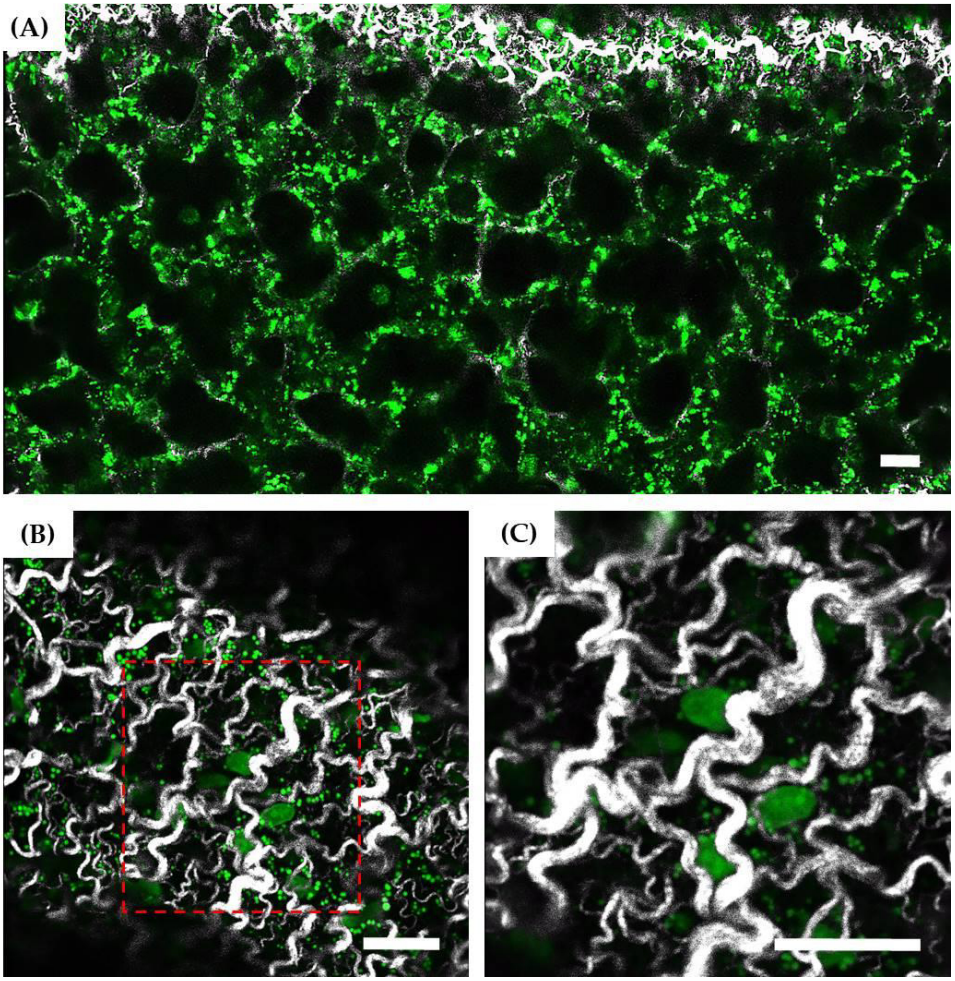

Figure 6.3: Simultaneous TPE and SHG images of ex-vivo lung tissue. **(A)** TPE and SHG signals imaged with 800 nm wavelength. Alveolar sacs can be recognized thanks to their TPE auto-fluorescence emission (Green) and are surrounded by the coarse collagen fibers of the serosa (White). **(B)** and **(C)** are two magnifications of the serosa collagen fibers. Scale bars $20\mu m$. From Filippi *et al.* [91]

As can be seen in Figure.6.3, the collagen fibrillary structure of the lungs appears clearly thanks to the SHG signal in the white channel, while the alveoli and several nuclei from cels inside the lung tissue were visible in the green channel. Both collagen features and cell nuclei remained perfectly visible and crisp even at relatively high zoom level, without any sign of photo-bleaching or photo-damages, confirming the power of this Label-Free technique when properly optimized.

A final test was performed to assess the ability to simultaneously optimize the excitation efficiency of different features: a portion of decellularized bovine pericardium was imaged with both the laser sources, in order to show the SHG of collagen fibrils and the autofluorescence of the elastin (Figure.6.4). The elastin absorption maximum is observed at 425 nm, requiring excitation from the 800 nm laser, while the fibrils, which in theory could be observed at any viable wavelength, were observed using the 1200 nm laser, avoiding detection of blue photons, which would be absorbed rapidly by the collagen itself. As te two laser sources were optimized in order to achieve maximum signal emission from their specific targets, bright images with clearly distinguishable SHG and autofluorescence signal were acquired, up to 200μm deep in the sample.

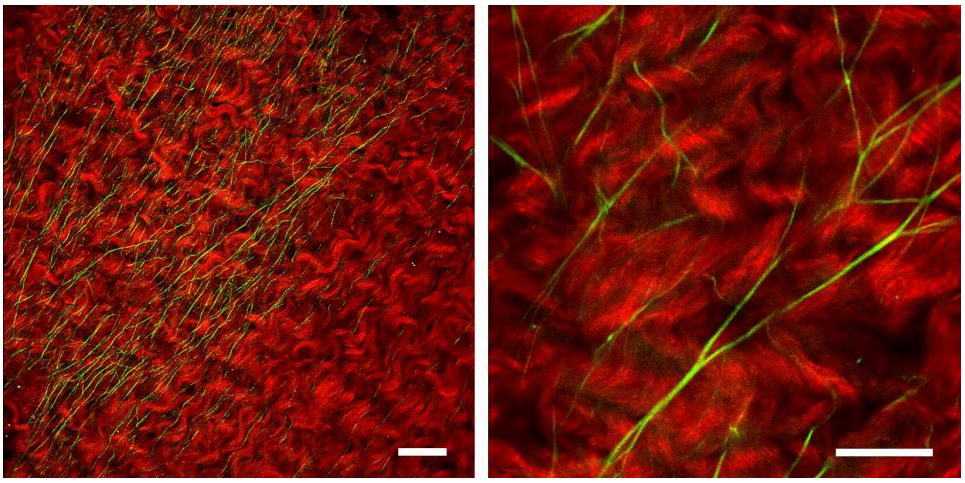

Figure 6.4: Simultaneous TPE and SHG images of decellularized pericardium for scaffold characterization. SHG signal from collagen bundles imaged with 1200 nm wavelength (Red) and elastin autofluorescence excited with 800 nm wavelength (Green). Scale bars 50 ţm. From Filippi *et al* [91]

6.3 Two-color Two-photon imaging

Pulse synchronization control As described in Chapter 2, when nondegenerate excitation is provided by two different beam pulses, the process efficiency will scale as $P_1 P_2 \ \exp(-\Delta t/\tau_{\mathrm{TIIC}})$, where P_1 and P_2 are the excitation beam powers, Δt is the temporal delay between the pulses and τ_{TIIC} is the width of the pulses temporal intensity intercorrelation function (TIIC). Assuming for both the pulses a Gaussian temporal profiles with width τ_1 and τ_2, the TIIC will be a Gaussian function too, with $\tau_{\mathrm{TIIC}} = \sqrt{\tau_1^2 + \tau_2^2}$. Given the nominal widths of the laser pulses, $\tau_{\mathrm{Ti:}Sa} = 140\,\mathrm{fs}$ and $\tau_{\mathrm{OPO}} = 200\,\mathrm{fs}$, the TIIC width was expected to be $\tau_{\mathrm{TIIC}} = 244\,\mathrm{fs}$. To span the entire overlap region, a $40\mu m$ delay range must be provided, and to set the maximum MCMPE efficiency with a tolerance of 5%, the accuracy needed is $\pm 27\,\mathrm{fs}$ ($\pm 4\mu m$ spatially). The choice of the linear stage has to take into consideration these two main requirements. In order to provide overlapping images without aberrations with both the beams, the two foci were aligned with a precision of a few tens of nanometers in the focal plane, and to a coarser degree ($< 0.5\,\mathrm{nm}$) in the axial direction (Figure.6.5).

The overlap interval was found using the fast photodetector, characterized by rise and fall times of about 70 ps, equivalent to a spatial accuracy of 21 mm. The fine overlap of the pulses was performed using as feedback the SFG signal emitted by mashed KDP powder illuminated by both the beams: the high nonlinear suscettivity of the material makes it an ideal choice to observe strong harmonic generation phenomena, both degenerate and non-degenerate.

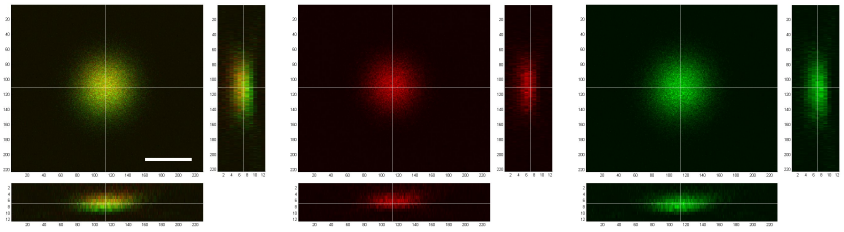

Figure 6.5: Spatial alignment of the beams foci, in the lateral an axial directions. The square windows show the focal plane distribution, with pixel size 8 nm/px. The lateral windows show the XZ/YZ projections of the photograms stacks, with a Z-pixel size of $0.4\mu m$/px. **Left)** Combined visual of the two beams PSF, the image was obtained visualizing an isolated quantum dot. The PSF of the 880 nm beam is coloured in red, while the 1300 nm PSF is shown in green. **Center)** 880 nm PSF, **Right)** 1300 nm PSF. Scale bar: 500 nm.

The dimensions of the crystals were great enough to provide a strong backscattered signal, which allowed to observe clear SHG and SFG images of the grains with the epi-detection architecture. We used wavelengths of 880 nm and 1350 nm, expecting to see signals at 440 nm, 675 nm, and 530 mn. The choice was made in order to see the different wavelengths with different detectors.

The results are shown in the left panel of Figure.6.6: in the top and central rows only one beam was used to illuminate the sample, first the 880 nm and then the 1350 nm, in the bottom row both the beams shutters were left open. Only in the latter case the green channel shows the same image of the other two, which confirms the SFG nature of the signal. The average signal strength at different position of the delay line is shown in the right panel, where the zero is set on the position of maximum efficiency, where the overlap degree between the pulses is at its highest. Since the SFG dependency on the pulse delay follows the same expression of the MCMPE, the plot gives a precise reconstruction of the TIIC.

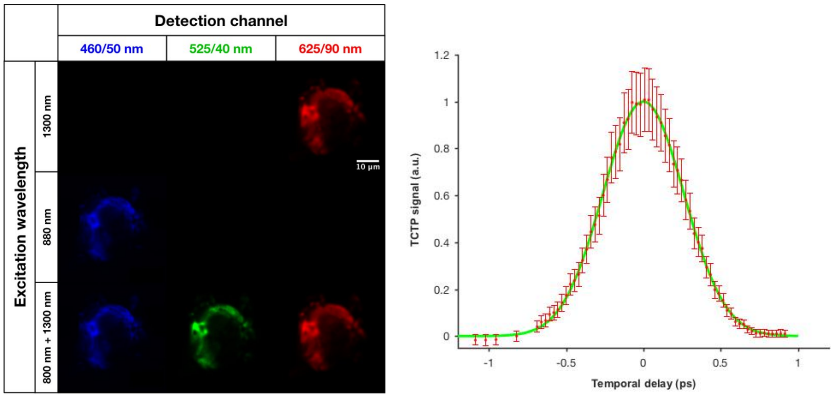

Figure 6.6: **Left)** Image of the SHG and SFG signals emitted by the KDP crystal: each of the squares on a row corresponds to a different wavelength of the detected light (A for the 425/25 nm, B for the 548/40 nm, C for the 625/90 nm), while each row indicates a different beam configuration. At the top, the 800 nm wavelength shutter was open and the 1300 nm one was closed, in the central row, the configuration was inverted, while the row at the bottom shows the result of both the beams shutter being open. It is easy to see that only when the two beams are hitting the sample, we manage to see the signal from the green channel. **Right)** Plot of the SFG signal for different positions of the delay line. The process efficiency shows a profile identical to the TIIC between the two pulses. The zero was set in correspondence of the TIIC maximum. Data for the errorbar plot was extracted following the procedure explained in Chapter 5.

This means that the control of the MCMPE channel intensity can be calibrated directly from these results, without using additional fluorescent test samples. The delay line was swept over a $300\mu m$ range, with a $4\mu m$ step, corresponding to a 2 ps interval sampled evey 27 fs. The width of the TIIC, measured as the $1/e^2$ diameter of the Gaussian fit, turned out to be (371 ± 5) fs.

Tests on biological samples After the calibration, we tried to observe TCTPE on biological samples. We used a MEF cells culture, stained with Alexa633 (Phalloidin), Alexa488 (Tom20) and DAPI. This combination was chosen in order to use the red and blue TPE fluorescence signal as reference, while keeping the green channel with the role of TCTPE signal detector. The different cellular structures highlighted by the fluorophores were needed to eliminate any ambiguity regarding the source of each signal. Wavelengths 820 nm and 1200 nm were used for the pump and OPO beams, respectively,

Figure 6.7: Images of MEF cells stained with Alexa633 (phalloidin), Alexa488 (Tom20) and DAPI(cell nuclei). The cells were imaged using 820 nm and 1200 nm wavelengths, which corresponds to 410 nm and 600 nm TPE and 974 nm TCTPE excitation. All the images were processed using the Fiji software in order to show the same color scale. **Top Left)** The merged blue, green and red channels are shown as the sample is excited only by the pump beam. The strong DAPI signal is visible, while the red and green fluorophores show only a faint image. **Top Center)** Image from the OPO beam illumination. The strength of the 1200 nm beam was kept low to reduce bleaching. The result is the absence of a visible signal. **Top Right)** Image from simultaneous pump+OPO illumination: while the blue signal does not show appreciable changes, both the red and green channels become brighter, and the mithocondrial network highlighted by the Alexa 488 fluorophore becomes clearly visible. **Bottom)** Green channel signals: as the two beams are simultaneously switched on (Right panel), the DAPI signal keeps the same level as with only the pump laser excitation (Left panel), while the mithocondrial structures become brighter, sign of an additional excitation source working exclusively on Alexa 488.

so that the corresponding TCTPE virtual wavelength was 974 nm, near the center of the $[900-1000]$ nm window. We can see the cells in Figure.6.7: on the left panel the cells illuminated only by the pump beam show a clear DAPI emission from the nuclei, which allows to easily identify each of them, while the green and red signal are sensibly lower. The dimness of the red channel is due mainly to the fact that we kept a low pump intensity during acquisition in order not to bleach the sample. The low brightness of the green channel is due to the faint signal coming from the DAPI and Alexa 488, instead, as it can be seen from the images of the left bottom panel, where only the green channel is shown. The OPO beam image, shown in the top central panel, didn't show any useful signal, not only in the blue and green channel, but also in the red one, where a faint Alexa 633 image should have been visible. The moderate beam intensity and the low Alexa 633 cross-section at 1200 nm (which corresponds to the lowest energy level excitation and is then less efficient in TPE) are to blame. As both the lasers shutters were opened (bottom and top right panels), AF488 signal increases dramatically, shadowing the DAPI green tail, which remains almost unperturbed by the additional light. Alexa 488 is not easily excited by TPE outside the $[900-1000]$ nm range, but here we see a strong signal, on par with the regular fluorescence from the other two fluorophores. This is proof that we were able to open an intermediate excitation channel by means of nondegenerate multiphoton absorption.

6.4 Conclusions

These results show how it is possible, with only the moderate expense of an OPO head and a mechanical delay line, to provide a broad excitation window extending well beyond the commercial Ti:Sapphire systems. In particular, the choice of a pumped laser system gave us an in-built synchronization, without the need of expensive dedicated circuitry. The synchronization, added with the mechanical delay line, provide the control of the TCTPE channel, which can cover most of the wavelength range unreacheable by both the pump and OPO laser platforms. We expect this new system to be able to expand our *in vivo* imaging capabilities in the near future.

Chapter 7

STED Microscopy: experimental results

7.1 Introduction

As described in Chapter 3, TPE-STED was previously obtained with excitation wavelengths shorter than 800 nm [3, 72, 5, 4]. This $700 - 800$ nm window is linked to the excitation of higher energetic levels of the molecules, which in the SPE regime have low efficiencies due to selection rules, while in the MPE regime they take advantage of the different requirements. As longer wavelengths overlap again with the excitation of the lower excited state, where the MPE regime is disadvantaged respect to SPE, the excitation efficiency is usually lower, and high intensities are required to get a uniform image without using a high number of frames or a long pixel dwell time. This in turn has the consequence of increasing the bleaching of the fluorophores and the damage on the cellular structures. Additional risks come from using the [750-850] nm wavelength window to perform STED, due to the increased probability of unwanted SPE and TPE phenomena. In such a situation, there is a limit to how much the proper alignment and calibration of the microscope can provide super-resolution by itself.

Most of the handicaps listed above can only be overcome by a suitable choice of fluorescent molecules, with high excitation cross-section in the [1000-1300] nm range and low excitation efficiency in the [700-900] nm window, both in the SPE and TPE regime (though the second requirement is much easier to meet, given the lower intensities of the stretched STED pulse). To this day, we could not find documentation about any attempt to achieve TPE-STED at long NIR wavelength. The following chapter describes the efforts done in order to set up and operate a STED system on the existing TPE platform, together with the assessment of the LWTPE-STED usefulness of different dyes and fluorescent proteins.

Given the strict NA requirements of STED microscopy, all the results

shown in this chapter were obtained using the UPLSAPO100XO objective (1.4 NA). In order to keep the experimental conditions throughout the imaging sessions as constant as possible, all the images reported in the following paragraphs were taken scanning an area of width $8.2\mu m$ with horizontal resolution of 512px or 1024px. The vertical height of the images was selected in order to achieve a strong cumulative averaging between multiple images in a time interval shorter than a few seconds. From these considerations, the spatial sampling rate at which the images were acquired is $8 - 16$ nm per pixel, with an average pixel dwell time of $46 - 92$ ns.

7.2 Stretching Line Control and Depletion

As described in Chapter 4, the STED configuration of the setup requires the stretching of the depletion beam pulse from the original 140 fs to a sub-nanosecond width. The stretching is performed by the glass rod combined with the single-mode optical fiber. Additionally, the delay line that allows control of the relative delay between depletion and excitation is positioned in between the two stretching optics. This way, the small misalignments of the beam caused by the shift of the mirrors position does not have any effect on the beam at the output end of the fiber, except for a loss of coupling efficiency that can be quickly regained by centering the fiber input end back on the beam waist. We measured the STED pulse width after the optical fiber using the same procedure described in Chapter 6: a preliminar coarse overlap of the pulses with the help of the fast photodetector, followed by a fine correction using the SFG signal from the KDP powder at different positions of the delay line.

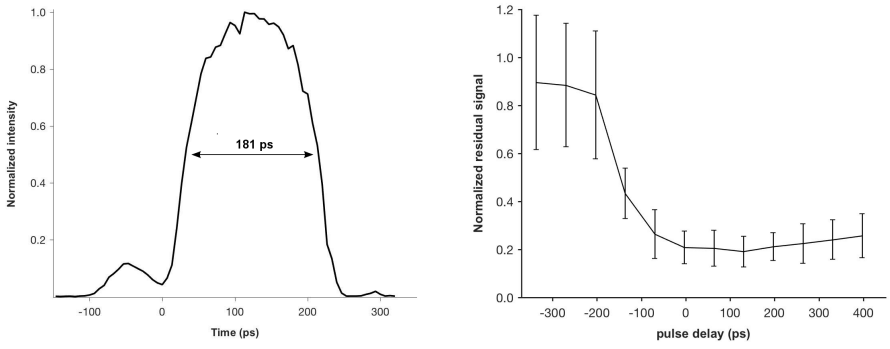

Figure 7.1: **Left)** Temporal profile of the STED pulse as measured using the SFG signal coming from the KDP crystal grains. **Right)** Graph showing the depletion efficiency on red fluorescent beads at different delays between the pulses. The zero position was set at the minimum residual signal point.

The pulse temporal profile can be extracted in this phase, and we can see it in Figure.7.1, where it shows a full-width at half maximum (FWHM) of (181 ± 9) ps.

Proper STED alignment differs from the simple overlap required by MCMPE in the fact that the depletion pulse must closely follow the excitation without significant overlap. The observation of SFG requires overlap, so that only an imprecise alignment of the two pulses can be achieved. The final phase of the pulses alignment was then performed using the feedback from the depletion process itself: a uniform ATTO647N distribution ("dye sea") was imaged at different positions of the delay line, and the signal was collected both in the simple excitation case and while performing depletion. The graph in Figure.7.1 shows the typical sharp decrease of the signal when the depletion pulse arrives with an optimal delay after the excitation pulse, and the slow increasing ramp, which is visible only in its beginning section, that corresponds to temporal separations long enough to let some fluorescence photons be emitted by the excited molecules.

After stretching and temporal alignment, the beam irradiance profile must be given its doughnut shape. We used the masks described in Chapter 4, assessing the proper alignment with the light reflected by gold beads dispersed in oil, at the focal plane of the objective lens. Figure.7.2 shows the STED beam doughnut and its horizontal line profile: the central doughnut intensity is lower than 10%, which following the indications of [92] should provide a depletion of the useful signal lower than 50%, then keeping the SNR sufficiently high for super-resolution imaging. The circular polarization state of the beam was checked with a polarization analyzer.

The first tests on the super-resolution capabilities of the instrument were performed on ideal samples: diamond nanocrystals, known for their high resistance to fluorescence damage and for their high depletion efficiency [93],

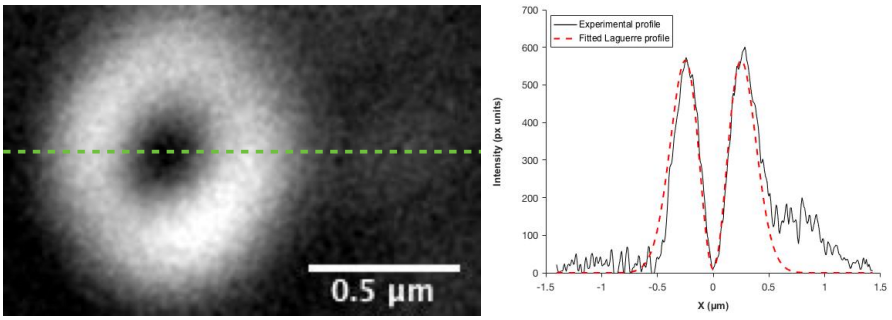

Figure 7.2: **Left)** Example of doughnut shape, imaged using reflection from 80 nm gold nanospheres dispersed in immersion oil. **Right)** Doughnut intensity profile along the linear green ROI (continuous line), compared to its fitted, Laguerre profile (dashed red line). The central intensity is lower than 10% of the maximum average value over the ring.

and fluorescent beads. The tests were performed at full STED power, meaning an average 160 mW on the microscope entrance (~ 80 mW on the objective back aperture). Fig.7.3 shows the resolution enhancement obtained on the diamond nanocrystals: from a $\mathrm{FWHM}_{2P} = (976 \pm 32)$ nm to $\mathrm{FWHM}_{2P-\mathrm{STED}} = (720 \pm 32)$ nm, the ratio between the widths is 1.36 ± 0.08, which means a gain in resolution of about 35%. Fig.7.4, similarly, shows the results on the GATTAquant beads sample: there too, from a $\mathrm{FWHM}_{2P} = (370 \pm 20)$ nm obtained from the 1200 nm laser, to $\mathrm{FWHM}_{2P-\mathrm{STED}} = (240 \pm 50)$ nm with STED depletion at 780 nm, the resolution gain appears to be 1.34 ± 0.08. This results can be interpreted as the best performance our setup is able to provide, both in terms of STED power and in terms of doughnut quality.

7.3 Fluorophores for LWTPE-STED

LWTPE-STED requires, as said above, high cross-sections relative to TPE at wavelengths longer than 1000 nm, and extremely low sensibility at wavelengths in the $[700 - 900]$ nm. This is usually a difficult requirement to meet with conventional dyes, as only recently the market started to offer a number of fluorescent molecules specifically oriented to the excitation and the emission in the far-red spectral window. Even though this is more an improvement targeted to the existing confocal setups, LWTPE microscopes too can take advantage of their use. Just as longer excitation wavelengths experience less scattering and absorption, and are able to probe deeper tissue regions, longer emission wavelengths provide a reduced loss of signal from those same heights, furthering the distance from the sample surface at which imaging is possible.

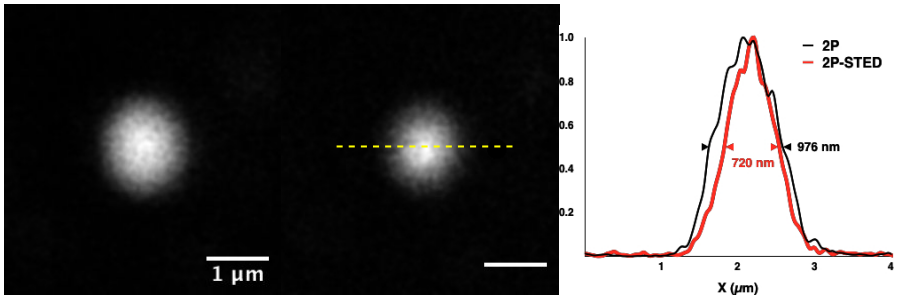

Figure 7.3: Diamond nanocrystal illuminated **Left)** only by the excitation beam ($\lambda = 1200$ nm) and **Center)** by both the beams. **Right)** Intensity profiles of the two images over the linear ROI shown in the central picture: from $\mathrm{FWHM}_{2P} = (976 \pm 32)$ nm to $\mathrm{FWHM}_{2P-\mathrm{STED}} = (720 \pm 32)$ nm we find a resolution enhancement factor of 1.36 ± 0.08. Scale bar $1\mu m$.

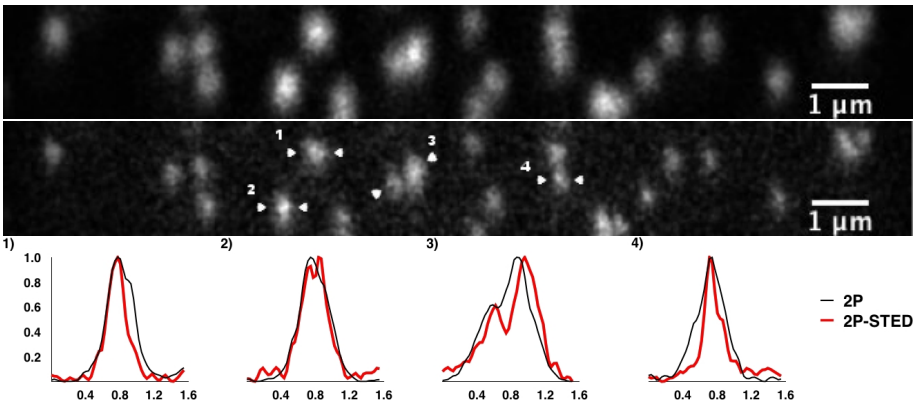

Figure 7.4: **Top)** GATTAquant beads (90 nm diameter) illuminated only by the excitation beam. **Center)** STED image of GATTAbeads. The resolution is visibly enhanced, in particular elements closely packed are now clearly separated. **Bottom)** Normalized intensity profiles of a few beads (plot lines specified by the white arrows in the central figure. from $\mathrm{FWHM}_{2P} = (370 \pm 20)$ nm to $\mathrm{FWHM}_{2P-\mathrm{STED}} = (240 \pm 50)$ nm, the resolution gain is 1.34 ± 0.08.

Although an increasing range of molecules is made available for far-red SPE and TPE imaging, the development of dyes and proteins specifically intended for TPE excitation at wavelengths longer than 1000 nm is still on its way. This leaves us with the only option to assess how suited the existing far-red fluorophores can be for LWTPE-STED.

Molecule	**Type**	**Exc 1P/2P (nm)**	**Em. (nm)**
ATTO 594	dye	607 / 780 - 1140*	626
ATTO 647N	dye	644 / 840 - 1225*	667
mGarnet2	FP	640 / $<$ 1050*	670

Table 7.1: List of the dyes and fluorescent proteins tested. All the molecules emit in the orange/far-red window. The Alexa and ATTO fluorophores are the most famous dyes currently used for sted. The " * " symbol refers to values that were found experimentally using our setup. They are specific to the imaging system we used and should NOT be considered as values valid throughout the other existing platforms.

Table 7.1 shows a list of the dyes and fluorescent proteins we tested for LWTPE and NIR depletion. The Alexa family is one of the most known in the field of immunostaining, though affected by fast photobleaching in typical SPE and TPE setups, their sharp excitation and emission peaks are suitable for a large variety of multicolor imaging purposes. The ATTO products were engineered as an improvement on the Alexa structure, much more resistant to bleaching and with a prolonged useful life of several months.

Repeated use of these dyes in super-resolution makes them the ideal test sample for STED platforms: the fluorescent beads we used contain it in pure form, while for depletion tests and regular imaging the conjugated version was used (in our case, secondary antibody IgG anti-rabbit), with a protocol described in section 5.3.

In addition to the exogenous dyes, we tested different red and far-red fluorescent proteins (FPs), expressed exogenously by cells through trasfection, as explained in detail in section 5.3. The protein approach gives several advantages respect to the immunostaining, such as the general compatibility with live-cell imaging (no fixation and permeabilization of the membrane is required to stain the intracellular structures, and no antbody is required for the attachment of the fluorophore) and the variety of already available sources. There are still disadvantages linked to using FPs, the main hurdle being the low fluorophore density that a cell can provide on its own, followed by the variable trasfection success rate and efficiency. In general, using FPs results in lower signals, even providing considerable excitation powers to the sample. While fluorescent dyes give more signal and a clearer image, though, FPs have spectra - or absorption efficiencies - that are much more compatible with our requirements of weak cross-sections in the $[700 - 900]$ nm, which brings them on par, if not better, with the exogenous source for LWTPE-STED. The best find in this aspect was the mGarnet2 protein, a modification of the monomeric Garnet molecule, with an excitation wavelength of 640 nm, an emission peak at 670 nm and a large Stokes shift of 30 nm, which is a considerable advantage for STED applications [6].

All the absorption efficiencies shown in the following graphs are measured from images of the same feature taken at different wavelengths, with a grossly constant laser power. Noise smoothing is performed applying a 1 px gaussian blur, signal intensity is extracted averaging the 5% brightest pixels of the images and dividing by the specific laser power (in mW, for SPE excitation, or its square, in mW^2, for TPE signals) measured at the beginning of the data acquisition. To measure the powers directly behind the objective aperture, the remotion of the objective lens was required, and any kind of measure at the level of the sample required cumbersome calibration procedures, combined with risks of unwanted drifts due to slipping of the glass support. As we placed the highest importance in testing the fluorescent molecules in steady and uniform conditions, we limited ourselves to measure the powers before the entrance of the microscope. Though the maximum power achievable by our setup was about 170 mW, we never used levels higher than 150 mW, due to high STED excitation signals or due to the damage inflicted to the cell environment.

The data for the depletion curves were acquired from images of the same features taken at different excitation and depletion powers. The "net" intensity values are extracted subtracting the raw data with "dark" images acquired with both the lasers shutters closed, following with the abovemen-

tioned smoothing and signal extraction. To measure the saturation powers of the molecules, we required the remotion of the STED excitation signal, so that we subtracted the signal generated under the excitation and depletion beams with the signal generated only by the depletion beam, finding the "subtracted signal".

The graphs relative to the subtracted signals show an approximately exponential behaviour, but upon different trials with pure, offset and multi-exponential functions, it turned out impossible to achieve a reliable fit on the plotted curves, as the fluorescence signal falls slowlier than expected, without reaching a proper saturation. As our interest lied only in finding the powers P_{sat} at which fluorescent emission was halved, we looked for an ad-hoc function capable to fit the experimental data. We found a close match with a square-root exponential: $I(P_{\text{STED}}) = I_0 + \Delta I \exp\left(-\log(2)\sqrt{P_{\text{STED}}/P_{\text{sat}}}\right)$. The I_0 term was introduced only in order to provide minor corrections to the fit, and its value was bounded to $< 1\%$ of the ($P_{\text{STED}} = 0\,\text{mW}$) signal.

The "normalized subtracted intensity" values are the ratios between the values of the subtracted signal curve and the value at $P_{\text{STED}} = 0\,\text{mW}$.

7.4 Far-red Dyes

ATTO 594 The ATTO 594 molecule behavior at different wavelengths is shown in Fig.7.5: the molecule shows a moderate amount of fluorescence at the STED wavelengths, and a faint excitation ratio at the OPO wavelengths, peaking at 1150 nm. The small ratios observed in the super-ţm spectral range can be easily compensated, though, using moderate-to-high intensities ($\sim 100\,\text{mW}$).

This is reflected by the high values of the dye TPE signal shown in the left panel of Fig.7.6. Despite the considerable brightness of the dye, though, the depletion efficiency at 795 nm is not very high, even with a correct temporal

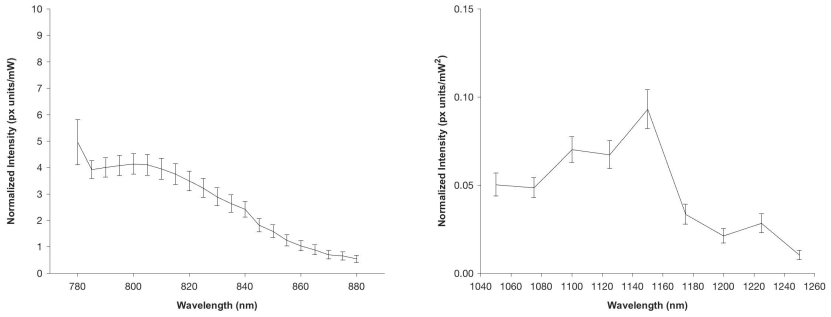

Figure 7.5: Relative emission intensities of the ATTO 594 dye in the spectral intervals **Left)** $[780, 880]\,\text{nm}$, and **Right)** $[1040, 1210]\,\text{nm}$.

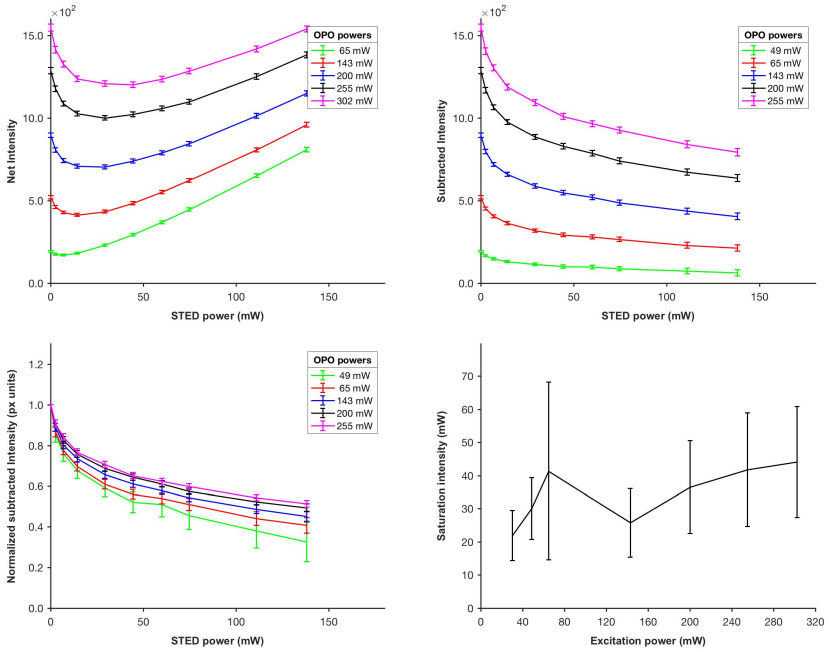

Figure 7.6: ATTO 594 depletion efficiency for different powers of the eccitation and STED laser beams. **[TOP] Left)** Fluorescence intensity (in px units) **Right)** Net fluorescence upon subtraction of the STED beam contribution. **[BOTTOM] Left)** Normalized net intensities. **Right)** Depletion saturation power vs average excitation power.

alignment: as presented explicitly in the bottom-left panel of Fig.7.6, the maximum depletion of the signal was found to be 60% of the original value, with an average saturation power lower than 50 mW.

ATTO 647N In Fig.7.7 it is possible to see the SPE and TPE spectra of the ATTO 647N molecule used: while the unconjugated molecule inside the GATTAbeads did not show a stronger absorption than ATTO 594 at the STED wavelengths, the conjugated version (anti-rabbit IgG, produced in goat) had a much stronger response in the same window, also reacting sensibly in the entire sub-μm spectral range. The excitation ratio due to the longer NIR wavelengths, though, appeared to be much higher than ATTO 594, with a peak at 1200 nm, so that we decided to test the depletion efficiency of the dye.

The bottom-left panel of Fig.7.8 shows that the fluorescence depletion becomes less efficient at higher powers of the STED beam, declining from 60% to 40%, a trend that is expressed in the bottom-right panel by the progressive increment of the saturation average power. Even with image post-processing, this dye proves to be unsuited for LWTPE-STED imaging.

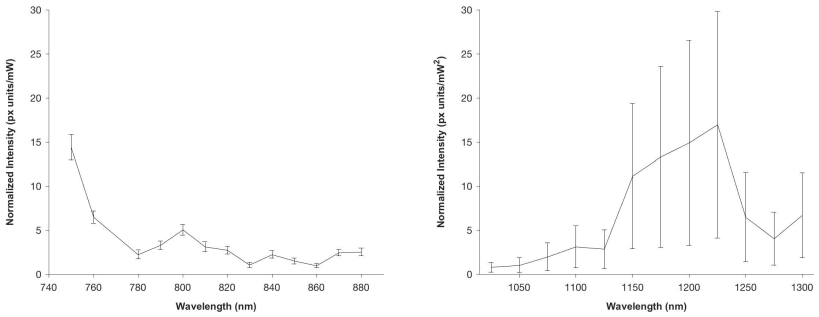

Figure 7.7: Relative emission intensities of the ATTO647N dye in the spectral intervals **Left)** $[750, 880]$ nm and **Right)** $[1025, 1300]$ nm.

7.5 Far-red Fluorescent Proteins

Following these results, we discarded the synthetic dyes in favor of the fluorescent proteins. In the last decade, fluorescent proteins have been attracting attention due to their suitability for live imaging, in particular the GFP

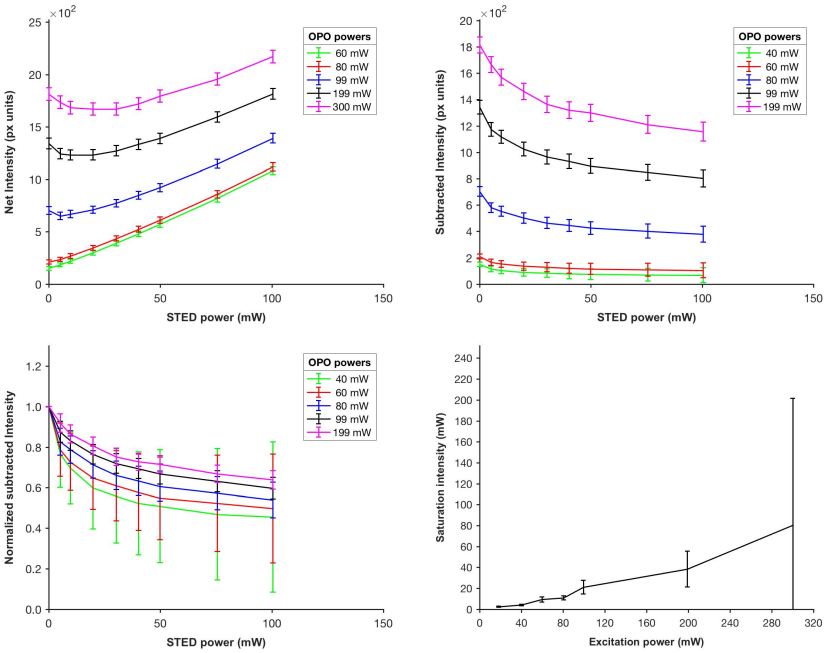

Figure 7.8: ATTO 647N depletion efficiency for different powers of the eccitation and STED laser beams. **[TOP] Left)** Fluorescence intensity (in px units) **Right)** Net fluorescence upon subtraction of the STED beam contribution. **[BOTTOM] Left)** Normalized net intensities. **Right)** Depletion saturation power vs average excitation power.

family. Far-red emitters, in particular, have been the target of most of the genetic engineering efforts to produce new color, due to the advantages of longer-wavelength excitation in live samples. Trasfection protocols used for the expression of the fluorescent proteins inside human cells are described in section 5.3. Between the various poteins we tested, the mGarnet2 (plasmid kindly gifted by prof. Nienhaus [6]) turned out to be the only one capable of both a strong fluorescence emission and a relevant fluorescence quenching at the desired working conditions.

mGarnet2 The emission properties of mGarnet2, as measured in our setup, are shown in Fig.7.9: the signal coming from the STED laser is still fairly low at wavelengths shorter than 800 nm, meaning that we can freely choose the depletion wavelength without compromising on the SNR ratio of the image. Regarding the excitation at super-μm wavelengths, it is clear that a strong peak exists in the [900-1000]nm, which still shows its influence up to 1100 nm. This broad "excitation spot" characteristic can be exploited to avoid autofluorescence peaks residing below the 1050 nm threshold.

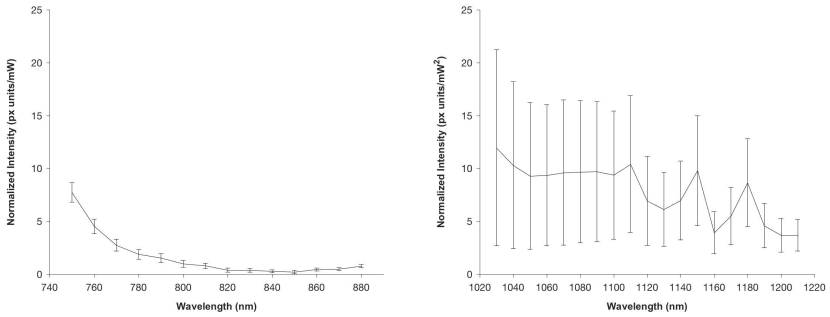

Figure 7.9: Relative emission intensities of the mGarnet2 protein (RITA) in the spectral intervals **Left)** $[750, 880]$ nm and **Right)** $[1020, 1210]$ nm

The depletion curves of mGarnet2 are shown in Fig.7.10: from the top left panel we see that the fluorescence induced by the depletion beam is negligible even at intermediate values of the excitation beam power. Image post-processing in this case is not a primary concern anymore, given the high similarity between raw and net fluorescence value in the two top panels. This is a significant advantage respect to the ATTO molecules tested above. The depletion ratios showed in the bottom left panel are not much different from the ones we saw before, except for the slow slope of the curves, which hints at the possibility of depleting a greater fraction of the fluorescence signal, either further raising the STED beam power, or using shorter depletion wavelengths. The slow depletion increment is confirmed by the saturation powers shown in the bottom right panel, twice as high respect to the values previously derived for the ATTO dyes.

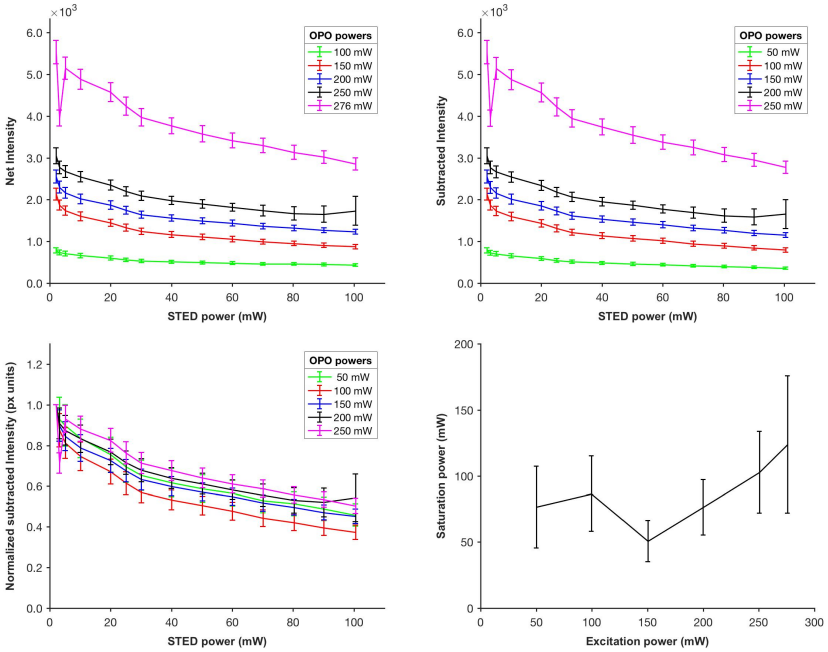

Figure 7.10: mGarnet2 depletion efficiency for different powers of the eccitation and STED laser beams. **[TOP] Left)** Fluorescence intensity (in px units) **Right)** Net fluorescence upon subtraction of the STED beam contribution. **[BOTTOM] Left)** Normalized net intensities. **Right)** Depletion saturation power vs average excitation power.

7.6 Conclusions

We tested the ATTO 594, ATTO 647N and mGarnet2 molecules for depletion at 795 nm, after excitation, respectively, at 1150 nm, 1200 nm and 1050 nm. The results show that a tradeoff must be made when choosing between one of the two dyes and the fluorescent protein: immunostaining probes show a stronger signal overall compared to mGarnet2, together with a relatively low saturation intensity, that our setup is able to reach and surpass routinely, but at the same time they are easily excited by the STED wavelengths, so that not only image processing is always needed to remove excitation background, but any super-resolved structure that might have been revealed also ends up hidden by the strong doughnut signal. mGarnet2, on the contrary, shows a much lower - if not absent - signal when irradiated by the depletion light, this time at the expense of the TPE signal from the 1050 nm laser and with the consequence of a higher saturation intensity, which lowers the depletion efficiency.

To solve this stalemate between noise and performance, different strategies would be available: the dyes could be depleted at longer wavelengths,

where the emitted signal would be lower, but this would mean moving beyond the 820 nm threshold, where the depletion efficiency is lower and the power available from the Ti:Sapphire resonator starts to drop. The opposite solution could also be tried, splitting a fraction of the depletion beam power before the stretching line and use it as a shorter wavelength excitation light source. This single-wavelength TPE-STED approach has been tried by different groups with good results [79, 94], it takes advantage of the high cross-section that many fluorophores show at $700 - 800$ nm to raise the density of excited molecules and reduce the risk of excitation background from the depleting beam.

For mGarnet2 and other FPs, this solution would not give advantages, given the already low short-wavelength cross-section: if anything, the total signal would be reduced, and the SNR would decrease as well. The only option in this regard would be to increase the available STED power, which would require the introduction of a dedicated laser beam, independent from the pump. At this point, we have the informations that we need in order to choose the next step to reach the required conditions for organic samples super-resolution imaging. The choice will be weighted in the near future.

Chapter 8

Fabrication and characterization of spiral phase plates for super-resolution applications

8.1 Introduction

As stated in Chapter 3, STED microscopy requires the generation of doughnut-like intensity distributions on the sample, a process that can be done with a common Gaussian beam coupled with a SPP, as explained in Chapter 4. With a careful control of the beam alignment and polarization, the doughnut profile is preserved on the sample, with a dark central intensity. Commercial SPPs provide plenty of the precision needed for the generation of such doughnut beams, but the solutions are usually thought for a specific set of wavelengths, with customs solutions that are expensive and with a long turnover time. As research on different dyes and proteins for LWTPE-STED implies the need to test different STED wavelengths depending on the fluorescent molecules, either a dynamic DOE mimicking the SPP profile at different wavelengths or a fast and relatively cheap way to fabricate tailored SPPs must be adopted.

In this chapter, we show the results of the latter approach, that is, the fabrication of tailored spiral phase plates for different wavelengths. A paper describing the work done was published [82], which is reported in the following paragraph. The characterization of the doughnut quality for microscopy applications is given in the next paragraphs.

8.2 ARTICLE: Fabrication and characterization of high-quality spiral phase plates for optical applications

Research Article Vol. 54, No. 13 / May 1 2015 / Applied Optics 4077

applied optics

Fabrication and characterization of high-quality spiral phase plates for optical applications

M. Massari,[1,*] G. Ruffato,[1,2] M. Gintoli,[2] F. Ricci,[1,3] and F. Romanato[2,4]

[1]Laboratory for Nanofabrication of Nanodevices (LaNN), Veneto Nanotech, Corso Stati Uniti 4, 35127 Padova, Italy
[2]Department of Physics and Astronomy "G. Galilei," University of Padova, Via Marzolo 8, 35131 Padova, Italy
[3]ICFO—The Institute of Photonic Sciences, Mediterranean Technology Park, Av. C. F. Gauss 3, 08860 Castelldefels, Spain
[4]CNR-INFM TASC IOM National Laboratory, S.S. 14 Km 163.5, 34012 Basovizza, Trieste, Italy
*Corresponding author: michele.massari@venetonanotech.it

Received 4 February 2015; revised 28 March 2015; accepted 6 April 2015; posted 8 April 2015 (Doc. ID 233490); published 27 April 2015

The discovery that light beams with a helical phase front carry orbital angular momentum (OAM) has enabled applications in many fields ranging from optical manipulation to quantum information processing and, recently, free-space information transfer and communications. Here, a novel three-dimensional fabrication process by electron beam lithography was finely tuned in order to realize high-quality spiral phase plates (SPPs) for the generation of OAM-carrying optical beams. Single- and multi-step SPPs have been realized for the generation of high-order Laguerre–Gaussian beams with different values of topological charge and radial index. The optical response of these optical elements was experimentally investigated and compared with theoretical models.

OCIS codes: (050.0050) Diffraction and gratings; (050.1965) Diffractive lenses; (050.6875) Three-dimensional fabrication; (050.4865) Optical vortices; (220.0220) Optical design and fabrication; (220.3740) Lithography.

http://dx.doi.org/10.1364/AO.54.004077

1. INTRODUCTION

Since 1992 [1] it is known that particular light beams characterized by helicoidal phase fronts can possess a well-defined orbital angular momentum (OAM). Unlike spin angular momentum (SAM), which is associated with the polarization of light, orbital angular momentum is linked to the spatial distribution of the intensity and phase of an optical field—even down to the single photon limit [2]. Such a property represents a fundamentally new optical degree of freedom. The fact that individual photons can carry OAM offers the most amazing practical possibilities for using OAM in the quantum domain. In contrast to SAM, which can assume only two possible states, OAM can span over an infinite range of integer values and therefore has the potential to extraordinarily increase the capacity of communication systems [3]. This opens the fascinating possibility to use OAM states either for encoding information or for multiplexing, exploiting OAM-carrying light beams to increase the capacity and the security of optical-fiber-based communications [4,5].

Nowadays, light beams carrying OAM can find applications in a number of different fields, ranging from biology to microscopy, astronomy, and radio communications. In biology, for instance, they can be used as optical tweezers to manipulate micrometer-sized particles and even living cells [6,7]. In phase contrast microscopy, the conversion of phase shifts to brightness changes of the image allows strong contrast enhancement and improved resolution to many cellular structures, otherwise not visible with traditional bright field microscopy techniques [8]. In astronomy, optical vortex coronagraphy can allow for direct detection of extrasolar planets with too low of a contrast ratio to their parent to be observed with other techniques [9–12]. In radio communications, twisted radio beams have recently been considered for an increment of the radio spectral efficiency by using the infinite number of OAM states accessible [13,14]. Finally, in quantum information processing the infinite number of quantum states available for the OAM-carrying optical field could allow for faster data manipulation with higher security [15,16].

Different techniques have been presented in the literature in order to tailor the orbital angular momentum of optical beams. A first method for OAM beams generation was demonstrated by Allen *et al.* with the conversion of Hermite–Gaussian into Laguerre–Gaussian beams by means of a couple of astigmatic cylindrical lenses [1]. Intensive interest in the field has required the development of more simple and reliable methods for the generation of helical wavefront beams from conventional Gaussian beams. One of the most widespread approaches is based on the use of the so-called fork-holograms [17], holographic structures encoding the interference pattern of the considered OAM beam with the generating reference wave,

1559-128X/15/134077-07$15/0$15.00

4078 Vol. 54, No. 13 / May 1 2015 / Applied Optics Research Article

e.g., a plane wave or a Gaussian beam. The interference pattern presents the structure of a grating with one or several central dislocations corresponding to the amount of topological charge and can be realized by lithographic techniques or implemented with computer-controlled spatial light modulators. A more recent method is based on particular anisotropic devices, the q-plates [18], particular birefringent liquid crystal plates having an azimuthal distribution of the local optical axis in the transverse plane, with a topological charge q at its center defect. In this work we focus on a refractive method for OAM generation based on transmission spiral phase plates (SPPs), phase optical elements looking like spiral staircases that shape the wavefront of the incident beam into a helicoidal profile [19]. The first demonstration of a spiral phase plate converting a TEM_{00} Gaussian beam into a Laguerre–Gaussian (LG) beam was proposed by Beijersbergen *et al.* [20]. With respect to the other techniques, spiral phase plates provide a stable, efficient, and compact method for OAM beam generation from common laser beams.

2. THEORY

Light beams carrying OAM always embed an optical vortex (OV) along the beam axis. From a mathematical point of view, OVs are wavefront dislocations, with peculiar topological properties, that arise due to phase singularities in the optical field. Light beams with an embedded OV are universally characterized by a dark central region—a consequence of destructive interference phenomena that gives the beam the typical doughnut-shaped intensity distribution [21].

In the paraxial regime, OAM beams can be described as a superposition of Laguerre–Gaussian modes characterized by the two indices ℓ and p. In cylindrical coordinates, in a plane orthogonal to the beam propagation direction and passing through the beam waist, the amplitude of the LG modes is given by [12]

$$u_p^{\ell}(r,\vartheta) \propto \left(\frac{r\sqrt{2}}{\omega_0}\right)^{|\ell|} L_p^{|\ell|}\left(\frac{2r^2}{\omega_0^2}\right) \exp\left(-\frac{r^2}{\omega_0^2}\right) \exp(-i\ell\vartheta), \quad \textbf{(1)}$$

where ω_0 is the beam waist radius, $L_p^{|\ell|}$ is the associated Laguerre polynomial and the term $\exp(-i\ell\vartheta)$ expresses the linear variation of the phase with the azimuthal angle ϑ. The azimuthal index ℓ, also called topological charge since it corresponds to the strength of the central singularity, indicates the number of twists of the helical wavefront within a wavelength and represents the amount of orbital angular momentum, in units of $\hbar$, carried by each single photon. The index p is related to the number of radial nodes on a plane perpendicular to the direction of propagation: the intensity pattern exhibits $p+1$ concentric rings around the central dark zone of phase singularity.

A spiral phase plate (SPP) is a helicoidal transmission element imposing an azimuthally dependent phase delay on an incident optical wavefront, while preserving the direction of the optical axis. It is a transparent plate, looking like a spiral staircase, in which the thickness increases around the central axis of the plate (see Fig. 1).

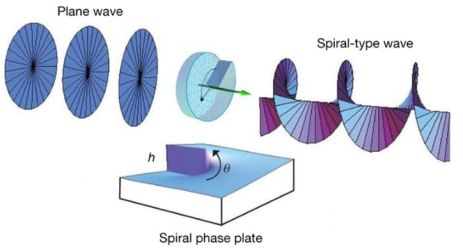

Fig. 1. On-axis working principle (top) of an ideal SPP device (bottom). A spiral phase plate is a transparent element whose thickness increases around the central axis of the plate. It operates imposing an azimuthally dependent phase delay on an incident optical wavefront, while preserving the direction of the optical axis.

The total phase gap in air

$$2\pi\ell = \frac{2\pi}{\lambda}(n_{SPP} - 1)h \quad \textbf{(2)}$$

is built, after a complete rotation of the azimuthal angle ϑ, through a finite number of equispaced levels [Fig. 2(a)], each one introducing a constant phase variation with h being the height of the spiral, n_{SPP} the refractive index of the SPP material, and λ the impinging wavelength. The quality of the output beam increases with the number of phase steps.

SPPs are built for a specific wavelength λ at which the maximum fainting along the optical axis is obtained. Therefore, the height of the spiral needs to be precisely engineered to produce the desired topological charge from the incident wavelength. A nanofabrication process to produce this kind of structure will need to precisely control the spiral geometry in order to accurately fulfill the design requirements of the optical device. In particular, the optical quality of the fabricated SPP mask depends on a good shape definition of the spiral, on the smoothness of the mask, and on the resolution of central singularity and phase step.

Electron beam lithography (EBL) represents a powerful tool to generate this kind of structure, due to the possibility to realize continuous surface profiles, high flexibility in the elements design, and good optical quality of the fabricated reliefs [12, 22–24]. In a recent paper [24] we presented a fabrication technique to obtain millimeter-sized SPPs by means of EBL working at 100 keV in high-speed writing mode, using high currents (tens of nA) and large beam diameters (tens of nm). In the present work we suggest a novel process realized in high resolution, where careful inspection of exposure parameters along with accurate proximity effect correction and optimization of developing conditions, allows for obtaining SPPs of superior optical quality.

3. MATERIALS AND METHODS

Spiral masks can be realized by shaping a disk of transparent material, with refraction index n, imposing a direct proportionality between the thickness of the material and the azimuthal position. 3D profiles can be generated modulating the local

Research Article Vol. 54, No. 13 / May 1 2015 / Applied Optics 4079

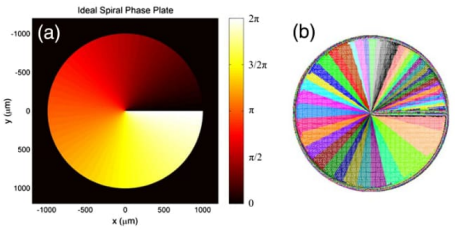

Fig. 2. (a) Designed pattern for the fabrication of a spiral phase plate with radial index $p = 0$, made up of a finite number of equispaced wedges. (b) 3D proximity effect correction calculated with the GenISys Layout Beamer software for fabrication of the element by electron beam lithography: different colors correspond to different doses to apply. In the represented case of a SPP with azimuthal index $\ell = 2$ illuminated by a beam of wavelength $\lambda = 632.8$ nm, doses go from 125 to 375 μC/cm^2, with a difference of less than 1 μC/cm^2 between subsequent colors.

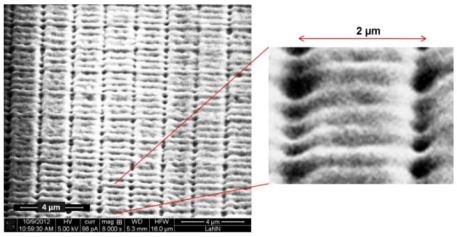

Fig. 3. Partially exposed plain pattern written at 100 keV in high-speed writing mode: the surface appears pitted with a series of holes and lines of extra-dose.

dose distribution, inducing different dissolution rates in the exposed polymer, giving rise to different resist thicknesses after the development process. A dose correction for the compensation of proximity effects is required both to match layout depth with the fabricated relief and to obtain a good shape definition, especially at the phase steps and at the central anomaly of the spiral phase mask [Fig. 2(b)].

In this work, 3D-spiral phase mask profiles have been written on a polymethylmethacrylate (PMMA) resist layer. The choice of ITO-coated soda lime float glass as a substrate has the purpose both to attain the needed transparency of the device and to assure a beam discharging during the exposure. For the considered wavelength of the laser beam used ($\lambda = 632.8$ nm), PMMA refractive index results $n = 1.489$ from spectroscopic ellipsometry analysis, therefore, according to Eq. (2), the total height of the fabricated spirals as a function of the topological charge is $h = \ell \cdot 1294.1$ nm.

A JEOL JBX-6300FS EBL machine, working at 100 keV, has been used to fabricate the SPPs. It is equipped with a 2-stage objective lens system for either high-speed or ultrafine writing mode. It operates dividing the exposure pattern into an array of fields which is then written using a combination of electron beam vector-scan and step-and-repeat stage movements. Due to the presence of errors in beam repositioning during the writing process, stitching mismatch can occur at field boundaries. This represents a serious problem in 3D fabrication since, due to the logarithmic character of the contrast curve, even small stitching overlaps can produce deep, wide grooves during the development process, heavily deteriorating the optical quality of the mask. In our previous work [22] we overcame the problem using the so-called "multi-field shift overlap writing mode," which operates by dividing the pattern into overlapping portions of the same field size and writing each one at a reduced dose, with the overall effect of substantially reducing the amount of field stitching.

Nevertheless, at an in-depth level, a further problem comes up with the appearance at a submicron level of dots or lines of extra-exposure within the pattern, in particular at the 2 μm subfield boundaries. The effect can be clearly seen in Fig. 3, which shows a partially exposed plain pattern written at 100 keV, with a 2 nA current, in high-speed writing mode: the surface appears as though it were pitted with a series of holes and lines of extra-dose.

Many tests have been made to eliminate what looks like a subfield stitching problem, by applying a suitable bias to the subfield size. Unfortunately, the issue appears difficult to remove with this strategy due to the lack of uniformity in the extra-dose distribution, especially at higher doses. Moreover, the required bias appears to be dependent on the dose and on the thickness of the resist layer (see Fig. 4). In addition, a kind of roughness is present even inside the subfields, especially at higher doses, due to a number of extra-dose lines which cannot be eliminated by just biasing the subfields. Further tests have been made at different acceleration voltages (25 and 50 keV) as well, still without substantial improvements.

We have then evaluated the chance to operate in high resolution (ultrafine writing mode, with a beam diameter down to 2 nm), in order to take advantage of the smaller subfield size with respect to the high-speed writing mode (0.5 versus 2 μm) and to reduce the resist beam charging by the use of a lower current (100 pA versus 2 nA). Coating the resist with a thin layer of gold has allowed us to both further reduce the beam charging and make use of the white light height detection system, unavailable for transparent samples. By measuring a height

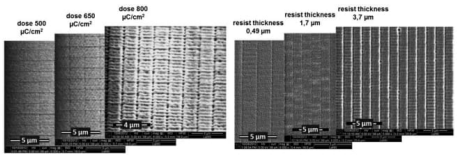

Fig. 4. Partially exposed plain pattern at different doses (from left to right: 500, 650, and 800 μC/cm^2) for the same PMMA resist thickness and for different resist thicknesses (from left to right: 0.49, 1.7, and 3.7 μm) at the same dose. Same development time and solution have been used for all the samples. Striping of the surface is clearly visible, which gets worse with the increase of the dose and the thickness of the resist layer.

4080 Vol. 54, No. 13 / May 1 2015 / Applied Optics Research Article

map of the surface, this system offers advantages both in stitching removal and in pattern resolution, thanks to a more precise setting of the beam focus. Finally, the choice of a long development time (600 s in a solution of deionized water:IPA 3:7) has allowed us to shorten the exposure time (allowing for low-dosage exposure) and improve the overall roughness of the surface. To compensate the proximity effect, we have worked in collaboration with GenISys GmbH, exploiting the Layout BEAMER PEC (Proximity Effect Correction) software.

4. RESULTS AND DISCUSSION

Careful inspection of exposure parameters, along with accurate proximity effect correction and optimization of developing conditions, has allowed for obtaining SPPs with superior optical quality [scanning electron microscopy (SEM) images of the fabricated masks can be shown in Figs. 5 and 6].

So far, though azimuthally high- and radially low-order LG beams have been extensively studied, only a few groups described the generation of radially high-order LG beams with nonzero radial index, obtained using spatial light modulators [25] or fabricated fork-holograms [26,27]. Spiral phase plates, however, are much more preferred, especially in applications such as spiral phase contrast microscopy [8], stimulated emission depletion (STED) microscopy [28], and optical coronagraphy [12], since they do not alter the direction of propagation and show a higher efficiency.

In this work we have been able to realize high-quality multistep SPPs with high values of the radial index p. A number of selected SPPs, with radial index p between 1 and 6 and topological charge $\ell = 1$, is shown in Fig. 6.

All the spiral phase plates presented in the paper have been fabricated starting from a layout consisting of 256 equally spaced wedges. This number has been chosen considering the minimum number of wedges theoretically calculated to observe an optical vortex using a spiral phase plate [29,30] and the reported number to obtain a continuous profile for a fabricated SPP [23]. The quality of the fabricated masks has been assessed using SEM and atomic force microscopy (AFM) techniques. In Fig. 5 the SEM micrograph of a fabricated SPP with radial index $p = 0$ and topological charge $\ell = 2$, whose layout is displayed in Fig. 2(a), is shown. The fabrication quality of the mask can be inferred from the good shape definition of the spiral, the smoothness of the mask, the sharp spiral phase step, and the high definition of the central singularity (shown in detail in Fig. 7). Moreover, the fabricated element has been characterized by AFM, with which we have measured a very low roughness, $R_{\mathrm{RMS}} < 2$ nm (average RMS on a surface area of 10 μm × 10 μm).

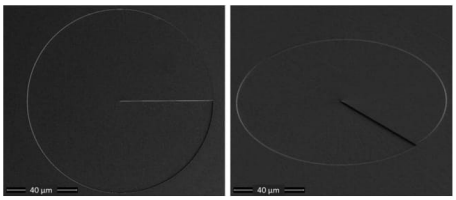

Fig. 5. SEM images (top and tilted) of a PMMA spiral phase plate with radial index $p = 0$ and topological charge $\ell = 2$, written at 100 keV in high-precision writing mode. An accurate 3D proximity effect correction and a thorough optimization of the process parameters have allowed us to obtain SPPs with smooth surfaces and highly defined steps and singularities (shown in detail in Fig. 7).

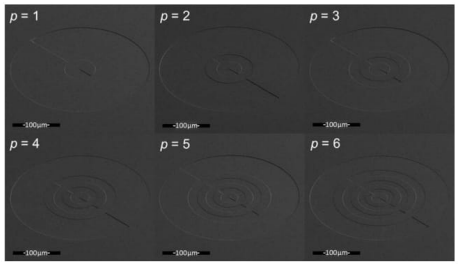

Fig. 6. SEM images of multi-step SPPs, with radial index p from 1 to 6 and topological charge $\ell = 1$, fabricated with high-resolution electron beam lithography.

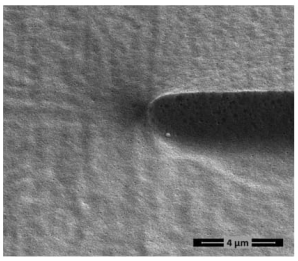

Fig. 7. Detail of the center of the spiral phase plate shown in Fig. 5. The tilted SEM image highlights the remarkable definition of the step and the singularity. The R_{RMS} surface roughness has been measured to be lower than 2 nm.

The fabricated SPPs were also optically characterized with the optical setup displayed in Fig. 8. A Gaussian beam ($\lambda = 632.8$ nm, beam waist $\omega_0 = 240$ μm, power $P = 0.8$ mW), emitted by a He–Ne laser (Thorlabs HNL008L) source, is focused by a lens L_1 of focal length $f_1 = 750$ mm onto the SPP. The lens is mounted on a slit to adjust the z-position, thus determining the focus position, the Gaussian spot size, and the wavefront curvature. Note that this step of the optical path is crucial to guarantee a flat wavefront illumination of the SPP, which would otherwise produce a far-field pattern substantially different from the analytical prediction. Finally, a far-field imaging system is created by means of a lens L_2 and a CCD in an usual f–f configuration.

In Fig. 9 we show a first result of the optical characterization of a SPP having radial index $p = 0$ and topological charge $\ell = 2$ (same device observed in Figs. 5 and 7). The figure presents the doughnut-shaped far-field intensity pattern

Research Article Vol. 54, No. 13 / May 1 2015 / Applied Optics 4081

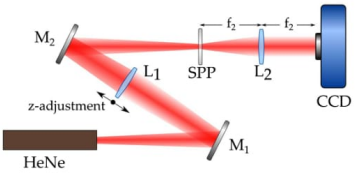

Fig. 8. Optical setup for the generation of Laguerre–Gaussian beams. The Gaussian beam, emitted by a Helium–Neon laser ($\lambda = 632.8$ nm, $\omega_0 = 240$ μm, $P = 0.8$ mW) is focused on a SPP, converted into an OAM-carrying optical vortex beam and detected by a CCD camera (pixel size: 3.4 μm × 3.4 μm, 3 × 12-bit RGB color depth) placed in the Fourier plane of the SPP.

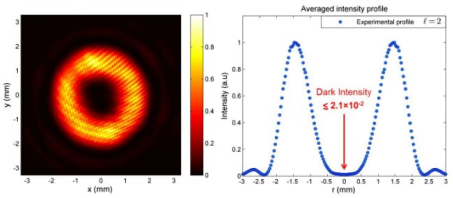

Fig. 9. Optical characterization of the SPP of radial index $p = 0$ and topological charge $\ell = 2$ observed in Figs. 5 and 7, along with the azimuthally averaged intensity profile taken on a plane perpendicular to the optical axis.

recorded by the CCD, together with the respective azimuthally averaged intensity profile.

Figure 10 shows the results of the characterization process for the SPPs of radial indexes $p = 1$, $p = 2$, $p = 3$ and topological charge $\ell = 1$ observed in Fig. 6. For the phase pattern of the optical elements depicted in Fig. 10(a), the far-field after Gaussian illumination was obtained by implementing a custom code in MATLAB environment based on a commercial algorithm for fast Fourier transform (FFT) calculation. The result is reported in Fig. 10(b) in a false-color scale, where the brightness indicates the intensity of the field and the color exhibits its phase. The intensity pattern measured on the camera [Fig. 10(c)] reproduces the simulated intensity distribution. Even if an antireflection coating was not present on the surface of the analyzed SPPs, the far-field intensity pattern appears not to be affected by an azimuthal modulation due to multiple internal reflections, as predicted and described in recent literature [31–34]. On the other hand, this effect could have been hidden by the noise due to signal fluctuation and further analyses could be required in order to unveil this phenomenon [33].

A theoretical survey of the optical response of these phase elements, along with an in-depth investigation of the purity of the experimental beams in terms of Laguerre–Gaussian mode contributions, has been recently published by our research group [35]. A clarification is worthwhile. The output generated by a Gaussian beam impinging on a spiral phase plate or a fork-hologram is, in the far-field, a confluent hypergeometric

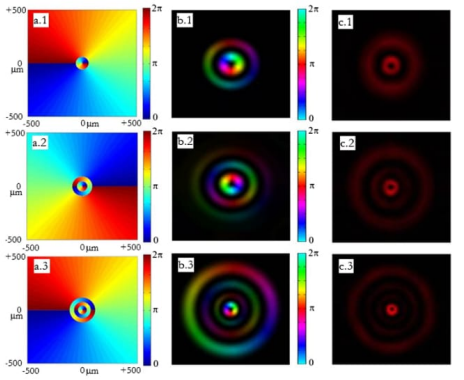

Fig. 10. Generation of LG_1^1, LG_2^1, and LG_3^1 beams. (a) Phase pattern of the corresponding spiral phase plates. (b) Simulation of the far-field. Brightness and colors refer, respectively, to intensity and phase of the field. (c) Experimental far-field intensity pattern.

Gaussian beam (also called a "Kummer beam" [36]). As demonstrated in [35], OAM beams generated by our spiral phase plates, or by multi-ringed fork-holograms as well, do not present an analytical expression as simple Kummer beams, since they are a convolution of Kummer beams with a finite sum of Bessel functions. However, since these modes can be decomposed in the complete set of Laguerre–Gaussian beams with the same azimuthal index, and moreover in this sum more than 80% of the total energy is carried by a single Laguerre–Gaussian beam with the prescribed p-index, we assumed we can talk about Laguerre–Gaussian beams generation anyway. This is clear in Fig. 11, where the experimental cross section, measured on a plane perpendicular to the propagation direction

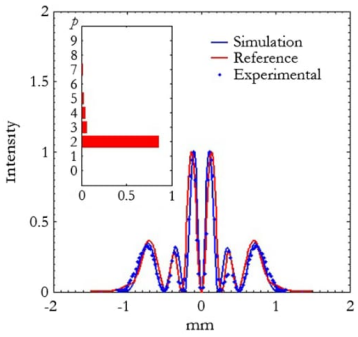

Fig. 11. Comparison between a cross section of the experimental far-field intensity (blue dots), numerical computation of the far-field intensity (blue solid line), and reference profile of a linear superposition of LG_p^1 beams (red solid line), with weights shown in the inset bar plot: $\gamma_0^1 = 8.48\text{e}-3$, $\gamma_1^1 = 4.75\text{e}-6$, $\gamma_2^1 = 85.5\text{e}-2$, $\gamma_3^1 = 6.12\text{e}-2$, $\gamma_4^1 = 3.85\text{e}-2$, $\gamma_5^1 = 1.85\text{e}-2$, $\gamma_6^1 = 6.54\text{e}-3$, $\gamma_7^1 = 9.59\text{e}-3$, $\gamma_8^1 = 4.22\text{e}-5$, and $\gamma_9^1 = 1.21\text{e}-4$.

and crossing the central singularity, is compared with the far-field numerical simulation and with a linear superposition of Laguerre–Gaussian contributions with $\ell = 1$, and p in the range 0–9. Experimental data exhibit a perfect accordance with numerical results. The efficiency in the generation of the dominant LG_2^1 is around 85.5%, with minor contributions from closer terms, in particular LG_3^1 (6.1%), LG_4^1 (3.8%), and LG_5^1 (1.9%) (cf. inset bar plot). All other terms contribute with less than 1% for an overall value lower than 3%.

5. CONCLUSIONS

In conclusion, a novel 3D fabrication process for high-optical-quality SPPs has been presented. It makes use of high-resolution electron beam lithography, based on accurate proximity effect correction and thorough optimization of process parameters, to obtain smooth surfaces and high resolution, especially in correspondence of critical features such as phase steps and singularities.

Single- and multi-step SPPs, with several radial indices and topological charges for the generation of different high-order Laguerre–Gaussian beams have been designed, realized, and optically investigated. The quality of the masks is highlighted by the remarkable accordance between simulated and experimental far-field intensity distributions. These optical elements can find applications in wide range of different fields, such as biophysics [6], micromechanics [37], or microfluidics [38] and might also be used in optical data storage [39], for imaging and metrology [8,11,40], or in free-space communications [3].

Last, we quote here that a high-quality SPP mask with radial index $p = 0$ and topological charge $\ell = 2$, realized by means of the novel fabrication process described, has recently been integrated in *Aqueye Plus* [41], a fast photometer with an optical vortex coronagraph for astronomical and industrial applications.

We gratefully acknowledge the companies JEOL Ltd. and GenISys GmbH for their cooperation and support, and Project SECARS—CARIPLO 2012 based at the Department of Physics and Astronomy of Padua University.

REFERENCES

1. L. Allen, M. W. Beijersbergen, R. J. C. Spreeuw, and J. P. Woerdman, "Orbital angular momentum of light and the transformation of Laguerre–Gaussian modes," Phys. Rev. A **45**, 8185–8189 (1992).
2. G. Molina-Terriza, J. P. Torres, and L. Torner, "Twisted photons," Nat. Phys. **3**, 305–310 (2007).
3. G. Gibson, J. Courtial, M. J. Padgett, M. Vasnetsov, V. Pas'ko, S. M. Barnett, and S. Franke-Arnold, "Free-space information transfer using light beams carrying orbital angular momentum," Opt. Express **12**, 5448–5456 (2004).
4. J. Wang, J.-Y. Yang, I. M. Fazal, N. Ahmed, Y. Yan, H. Huang, Y. Ren, Y. Yue, S. Dolinar, M. Tur, and A. E. Willner, "Terabit free-space data transmission employing orbital angular momentum multiplexing," Nat. Photonics **6**, 488–496 (2012).
5. N. Bozinovic, Y. Yue, Y. Ren, M. Tur, P. Kristensen, H. Huang, A. E. Willner, and S. Ramachandran, "Terabit-scale orbital angular momentum mode division multiplexing in fibers," Science **340**, 1545–1548 (2013).
6. K. Dholakia and T. Čižmár, "Shaping the future of manipulation," Nat. Photonics **5**, 335–342 (2011).
7. M. Padgett and R. Bowman, "Tweezers with a twist," Nat. Photonics **5**, 343–348 (2011).
8. S. Bernet, A. Jesacher, S. Fürhapter, C. Maurer, and M. Ritsch-Marte, "Quantitative imaging of complex samples by spiral phase contrast microscopy," Opt. Express **14**, 3792–3805 (2006).
9. G. A. Swartzlander, Jr., "Broadband nulling of a vortex phase mask," Opt. Lett. **30**, 2876–2878 (2005).
10. G. Foo, D. M. Palacios, and G. A. Swartzlander, Jr., "Optical vortex coronagraph," Opt. Lett. **30**, 3308–3310 (2005).
11. N. M. Elias II, "Photon orbital angular momentum in astronomy," Astron. Astrophys. **492**, 883–922 (2008).
12. E. Mari, G. Anzolin, F. Tamburini, M. Prasciolu, G. Umbriaco, A. Bianchini, C. Barbieri, and F. Romanato, "Fabrication and testing of $l = 2$ optical vortex phase masks for coronography," Opt. Express **18**, 2339–2344 (2010).
13. B. Thidé, H. Then, J. Sjöholm, K. Palmer, J. Bergman, T. D. Carozzi, Y. N. Istomin, N. H. Ibragimov, and R. Khamitova, "Utilization of photon orbital angular momentum in the low-frequency radio domain," Phys. Rev. Lett. **99**, 087701 (2007).
14. F. Tamburini, E. Mari, A. Sponselli, B. Thidé, A. Bianchini, and F. Romanato, "Encoding many channels on the same frequency through radio vorticity: first experimental test," New J. Phys. **14**, 033001 (2012).
15. A. Mair, A. Vaziri, G. Weihs, and A. Zeilinger, "Entanglement of the orbital angular momentum states of photons," Nature **412**, 313–316 (2001).
16. J. Leach, B. Jack, J. Romero, A. K. Jha, A. M. Yao, S. Franke-Arnold, D. G. Ireland, R. W. Boyd, S. M. Barnett, and M. J. Padgett, "Quantum correlations in optical angle-orbital angular momentum variables," Science **329**, 662–665 (2010).
17. N. R. Heckenberg, R. McDuff, C. P. Smith, H. Rubinsztein-Dunlop, and M. J. Wegener, "Laser-beams with phase singularities," Opt. Quantum Electron. **24**, S951–S962 (1992).
18. L. Marrucci, C. Manzo, and D. Paparo, "Optical spin-to-orbital angular momentum conversion in inhomogeneous anisotropic media," Phys. Rev. Lett. **96**, 163905 (2006).
19. S. N. Khonina, V. V. Kotlyar, M. V. Shinkaryev, V. A. Soifer, and G. V. Uspleniev, "The phase rotor filter," J. Mod. Opt. **39**, 1147–1154 (1992).
20. M. W. Beijersbergen, R. P. C. Coerwinkel, M. Kristensen, and J. P. Woerdman, "Helical-wavefront laser beams produced with a spiral phaseplate," Opt. Commun. **112**, 321–327 (1994).
21. D. L. Andrews and M. Babiker, eds., *The Angular Momentum of Light* (Cambridge University, 2012).
22. E. B. Kley, "Continuous profile writing by optical and electron lithography," Microelectron. Eng. **34**, 261–298 (1997).
23. M. Prasciolu, F. Tamburini, G. Anzolin, E. Mari, M. Melli, A. Carpentiero, C. Barbieri, and F. Romanato, "Fabrication of a three-dimensional optical vortices phase mask for astronomy by means of electron-beam lithography," Microelectron. Eng. **86**, 1103–1106 (2009).
24. M. Massari, F. Romanato, M. Carli, T. Ongarello, M. Prasciolu, F. Tamburini, E. Mari, A. Bianchini, and C. Barbieri, "Design, fabrication and characterization of phase masks for astronomical applications," Microelectron. Eng. **88**, 2675–2678 (2011).
25. N. Matsumoto, T. Ando, T. Inoue, Y. Ohtake, N. Fukuchi, and T. Hara, "Generation of high-quality higher-order Laguerre–Gaussian beams using liquid-crystal-on-silicon spatial light modulators," J. Opt. Soc. Am. A **25**, 1642–1651 (2008).
26. J. Arlt, K. Dholakia, L. Allen, and M. J. Padgett, "The production of multiringed Laguerre–Gaussian modes by computer-generated holograms," J. Mod. Opt. **45**, 1231–1237 (1998).
27. M. Granata, C. Buy, R. Ward, and M. Barsuglia, "Higher-order Laguerre–Gauss mode generation and interferometry for gravitational wave detectors," Phys. Rev. Lett. **105**, 231102 (2010).
28. D. Wildanger, J. Buckers, V. Westphal, S. W. Hell, and L. Kastrup, "A STED microscope aligned by design," Opt. Express **17**, 16100 (2009).
29. Q. Wang, X. W. Sun, P. Shum, and X. J. Yin, "Dynamic switching of optical vortices with dynamic gamma-correction liquid crystal spiral phase plate," Opt. Express **13**, 10285–10291 (2005).
30. V. V. Kotlyar and A. A. Kovalev, "Fraunhofer diffraction of the plane wave by a multilevel (quantized) spiral phase plate," Opt. Lett. **33**, 189–191 (2008).
31. Y. S. Rumala and A. E. Leanhardt, "Multiple-beam interference in a spiral phase plate," J. Opt. Soc. Am. B **30**, 615–621 (2013).

32. Y. S. Rumala, "Interference theory of multiple optical vortex states in spiral phase plate etalon: thick-plate and thin-plate approximation," J. Opt. Soc. Am. B **31**, A6–A12 (2014).
33. Y. S. Rumala, "Structured light interference due to multiple reflections in a spiral phase plate device and its propagation," Proc. SPIE **8999**, 899912 (2014).
34. P. Schemmel, G. Pisano, and B. Maffei, "Modular spiral phase plate design for orbital angular momentum generation at millimetre wavelengths," Opt. Express **22**, 14712–14726 (2014).
35. G. Ruffato, M. Massari, and F. Romanato, "Generation of high-order Laguerre–Gaussian modes by means of spiral phase plates," Opt. Lett. **39**, 5094–5097 (2014).
36. G. Anzolin, F. Tamburini, A. Bianchini, and C. Barbieri, "Method to measure off-axis displacements based on the analysis of the intensity distribution of a vortex beam," Phys. Rev. A **79**, 033845 (2009).
37. P. Galajda and P. Ormos, "Complex micromachines produced and driven by light," Appl. Phys. Lett. **78**, 249–251 (2001).
38. K. Ladavac and D. G. Grier, "Microoptomechanical pumps assembled and driven by holographic optical vortex arrays," Opt. Express **12**, 1144–1149 (2004).
39. R. J. Voogd, M. Singh, and J. J. M. Braat, "The use of orbital angular momentum of light beams for optical data storage," Proc. SPIE **5380**, 387–392 (2004).
40. L. Torner, J. P. Torres, and S. Carrasco, "Digital spiral imaging," Opt. Express **13**, 873–881 (2005).
41. E. Verroi, G. Naletto, C. Barbieri, M. Zaccariotto, T. Occhipinti, I. Capraro, L. Zampieri, A. Cardullo, F. Frassetto, B. Luca, F. Romanato, F. Ricci, and M. Gintoli, "Aqueye plus: a wavefront sensorless adaptive optics system for narrow field coronagraphy," Proc. SPIE **8864**, 88641W (2013).

8.3 Characterization of phase masks for STED super-resolution

To characterize the performance of our custom SPPs, we fabricated a mask designed to operate at the STED wavelength used in Chapter 7, $\lambda_{\mathrm{STED}} = 795\,\mathrm{nm}$, then we compared the generated intensity distribution, examined on the focal plane of the objective, with the one found using the commercial SPP. As a measure of fitness we evaluated the darkness of the central region, on which depends the super-resolution capability of the microscope, as explained in Chapter 3.

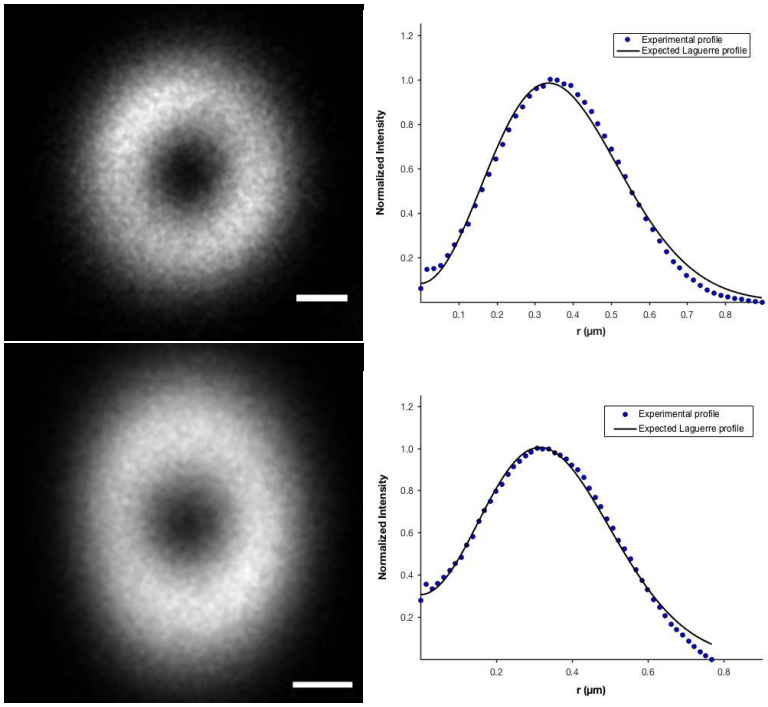

Figure 8.1: Comparison between the doughnut beams generated by the tailored and commercial SPPs on the sample plane (NA = 1.4). The photograms were taken imaging an isolated quantum dot. **[TOP] Left)** Doughnut from a tailored mask; **Right)** average radial intensity profile of the intensity distribution: the experimental points (blue dots) were fitted with the sum of a LG_0^1 Laguerre-Gaussian profile and a central Gaussian function (continuous line). **[BOTTOM] Left)** Doughnut from the commercial mask; **Right)** average radial intensity profile of the intensity distribution. Scale bars: 250 nm.

The evaluation was performed fitting the average radial intensity profile of the doughnut with a suitable function (the sum of a LG_0^1 Laguerre-Gaussian profile and a Gaussian function), and then computing the ratio between the fitted central intensity and the maximum intensity of the distribution. The reason why we chose to use the fitted instead of the average central intensity is due to the fact that even with high image resolution (8 nm/px, referring to the scaning step size), the central region always occupies a portion of a few tens of pixel, and the average intensities measured in that spot become sensitive to the local noise. To reduce this effect, we relied on the fit of the intensity profile.

Figure.1 shows the doughnut-shaped focal spots (left panels), observed imaging the same isolated quantum dot, and the relative average radial intensity profiles (right panels). The result are two qualitatively equal beams, with strong central intensities, even with a perfectly circular polarization at the back aperture of the objective. Upon consecutive measurements, we saw that independently on the mask we used, the average central intensity reached ∼20% of the maximum value found on the ring (Figure.1 shows a 10% and 30% central intensity for custom and commercial SPP). Further investigations showed that this high central intensity was an artefact due to the imaging of a quantum dot sample.

Other fluorescent sources showed a similar effect, so that we decided to switch to the observation of the light reflected by gold beads. The new measurements showed for the commercial masks an average (fitted) central intensity amounting to ∼5% of the maximum ring intensity. An example is given by Figure.2 of Chapter 7, that we report in Figure.2 for convenience.

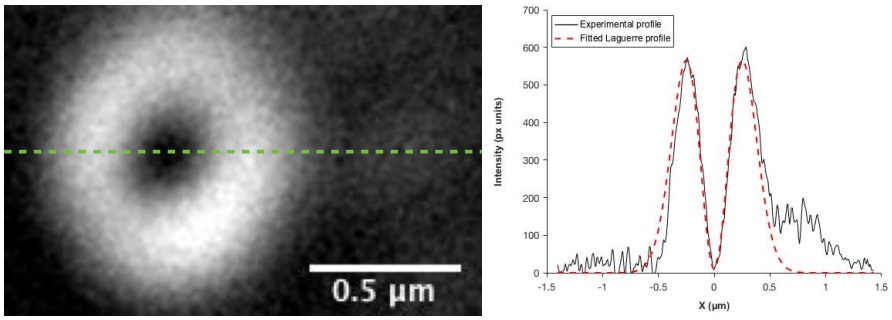

Figure 8.2: **Left)** Example of doughnut shape, imaged using reflection from 80 nm gold nanospheres dispersed in immersion oil. **Right)** Doughnut intensity profile along the linear green ROI (continuous line), compared to its fitted, Laguerre profile (dashed red line). The central intensity is lower than 10% of the maximum average value over the ring. The asymmetry on the right side of the profile is due to a small source of scattered light in the proximity of a doughnut.

The amount of central intensity for the custom masks was not measured, though we can expect a similar result, that will be measured in the near future.

8.4 Conclusions

We developed a protocol for the fabrication of custom SPPs using a high-resolution EBL process, based on a subfield size smaller than $1\mu m$, low exposure currents to reduce the charging effect on the resist, a conductive and reflective coating to further reduce charging and enable the local adjustment of the beam focus height, plus a low-contrast development process to minimize the surface roughness and to allow for faster, low-dose exposure.

The result is the faithful reproduction of the SPP design geometry, with a surface root mean squared (RMS) smaller than 2 nm. The optical performance of the SPP was measured in the paraxial regime, where the ability to reproduce Laguerre-Gauss beams with $p > 0$ with high fidelity ($> 80\%$ of the energy on a single p-mode) was demonstrated.

We finally characterized the generated doughnut quality of $\ell = 1$ masks on the focal plane of our microscope. Regarding the symmetry of the doughnut intensity distribution, we saw similar results compared with the commercial masks. We now have to test the doughnut central darkness to verify the capability to provide central intensities lower than 10% of the maximum average ring intensity.

Chapter 9

Conclusions

The current state-of-the-art in TPE-STED has been proved to work up to depth no greater than $100\mu m$, due to scattering, absorption and deformation of the wavefronts of the STED beam [4]. The aim of the work described in this thesis was the development of a first-of-a-kind STED microscope for *in vivo* applications, that surpassed the limitations of the current TPE-STED microscopes, working at longer excitation wavelengths and longer depletion wavelengths. An additional element of the microscope design was a configuration dedicated to two-photon excitation over the entire $[700 - 1500]$ nm spectrum, obtained from the combination of wavelength emitted by the pump+OPO system, and the virtual wavelengths of two-color two-photon excitation.

We also wanted to develop a fabrication process for tailored phase masks, aimed at the generation of doughnut beams at arbitrary depletion wavelengths.We obtained positive results testing the overall nonlinear imaging capabilities of the system with *in vivo* imaging in mice [95, 90], and with combined TPE autofluorescence/HG from murine heart and lung tissue [91]. We could also verify the ability to span the entire $[700-1500]$ nm wavelength range with the contribution of two-color excitation. On a separate note, these combined results are in agreement with previous tests of the validity of pump+OPO system as cheaper alternatives to synchronized dual-laser systems in nonlinear platforms [29].

As for the STED capabilities, we observed a resolution increment on fluorescent nanodiamonds and fluorescent beads, with a 34% reduction of the measured FWHM. We went on with preliminary tests on the ATTO dyes and the mGarnet2 fluorescent protein, which returned unsatisfactory results regarding the level of depletion reached by the molecules. ATTO 594 and ATTO 647N demonstrated low excitation efficiencies at wavelengths longer than $1\mu m$, so that many molecules left unaffected by the excitation pulse were excited, covering the super-resolution image with excitation background.

The tests on mGarnet2, which showed a low excitation cross-section at the depletion range, showed also a low depletion efficiency that could only be compensated by higher STED intensities beyond the reach of the pump+OPO system. As of now, we don't know of available fluorescent molecules with higher cross-section at the excitation wavelengths. As explained in the previous chapter, a tested solution suitable for the ATTO and other similar dyes is to use a fraction of the unstretched pump beam power to provide excitation, which would generate a higher density of excited fluorophores, and provide higher signals with lower unwanted excitation background.

The alternative of using longer STED wavelengths ($\geqslant 820\,\mathrm{nm}$) would require a different laser source, capable of higher intensities to compensate the lower depletion efficiency, and while this expense could be avoided for the dyes, it would be the only option available for mGarnet2 and other similar fluorescent proteins.

We successfully tested the fabrication of tailored phase masks with an EBL platform, obtaining optical surfaces that faithfully reproduce the design geometry and that show surface roughness at the nanometer level. Optical tests in the paraxial regime confirmed the ability to reproduce LG_p^ℓ modes with $p > 0$ with high fidelity [82], while tests of $\ell = 1, p = 0$ masks in the optical path of the microscope show symmetric doughnut distribution in the focal plane of the objective. Final tests will be performed to assess the level of darkness at the center of the doughnut.

The development of a fabrication process for custom three-dimensional surfaces has a value that goes beyond the customization of the microscopy setup with tailored spiral phase plates, as it can be extended to the generation of more complex spiral patterns, or even entirely different masks designs, like flat metasurfaces or holograms. The ability to freely design and fabricate custom optics opens also the possibility to develop multi-element optical devices for achromatic generation of doughnut beams (like in [96]). Although typically more difficult to install and align, multi-element achromatic optics would render the microscope able to work efficiently regardless of the depletion wavelength, which in turn would avoid the need for major changes in the setup configuration, thereby reducing the routine manteinance efforts required.

Bibliography

[1] M. Minsky. Microscopy apparatus, 1961. US Patent 3,013,467.

[2] S W Hell and J Wichmann. Breaking the diffraction resolution limit by stimulated emission: stimulated-emission-depletion fluorescence microscopy. *Opt Lett*, 19(11):780–782, 1994.

[3] Gael Moneron and Stefan W Hell. Two-photon excitation STED microscopy. *Opt Express*, 17(17):14567–14573, aug 2009.

[4] K T Takasaki, J B Ding, and B L Sabatini. Live-cell superresolution imaging by pulsed sted two-photon excitation microscopy. *Biophys J*, 104(4):770–777, feb 2013.

[5] Philipp Bethge, Ronan Chéreau, Elena Avignone, Giovanni Marsicano, and U. Valentin Nägerl. Two-photon excitation STED microscopy in two colors in acute brain slices. *Biophysical Journal*, 104(4):778–785, 2013.

[6] Gabriela Matela, Peng Gao, Gernot Guigas, Antonia F. Eckert, Karin Nienhaus, and G. Ulrich Nienhaus. A far-red emitting fluorescent marker protein, mGarnet2, for microscopy and STED nanoscopy. *Chem. Commun.*, 53(5):979–982, 2017.

[7] J R Lakowicz, I Gryczynski, H Malak, and Z Gryczynski. Two-color two-photon excitation of fluorescence. *Photochemistry and Photobiology*, 64(4):632–635, 1996.

[8] C. Xu, W. Zipfel, J. B. Shear, R. M. Williams, and W. W. Webb. Multiphoton fluorescence excitation: new spectral windows for biological nonlinear microscopy. *Proceedings of the National Academy of Sciences*, 93(20):10763–10768, 1996.

[9] Winfried Denk, JH H Strickler, and WW W Webb. Two-photon laser scanning fluorescence microscopy. *Science*, 248(4951):73–76, 1990.

[10] Stefan W Hell, Karsten Bahlmann, Martin Schrader, Aleksi Soini, Henryk M Malak, Ignacy Gryczynski, and Joseph R Lakowicz. Three-

photon excitation in fluorescence microscopy. *Journal of Biomedical Optics*, 1(1):71–74, 1996.

[11] David L. Wokosin, Victoria E. Centonze, Sarah Crittenden, and John White. Three-photon excitation fluorescence imaging of biological specimens using an all-solid-state laser. *Bioimaging*, 4(3):208–214, 1996.

[12] Ammasi Periasamy, Demirhan Kobat, Peter T C So, Angela Wong, Chris B Schaffer, and Chris Xu. Comparison of two-photon imaging depths with 775 nm excitation and 1300 nm excitation. 7183:71832D, 2009.

[13] N G Horton, K Wang, D Kobat, C G Clark, F W Wise, C B Schaffer, and C Xu. In vivo three-photon microscopy of subcortical structures within an intact mouse brain. *Nat Photonics*, 7(3), 2013.

[14] Y Barad, H Eisenberg, M Horowitz, and Y Silberberg. Nonlinear scanning laser microscopy by third harmonic generation. *Applied Physics Letters*, 70(8):922–924, 1997.

[15] J Squier, M Müller, G Brakenhoff, and K Wilson. Third harmonic generation microscopy. *Opt. Express*, 3(9):315–324, 1998.

[16] M Oheim, E Beaurepaire, E Chaigneau, J Mertz, and S Charpak. Two-photon microscopy in brain tissue: parameters influencing the imaging depth. *J Neurosci Methods*, 111(1):29–37, 2001.

[17] M Goeppert-Mayer. Ueber elementarakte mit zwei quantenspruengen. *Annalen der Physik*, 9(273):273–294, 1931.

[18] Y Sako, a Sekihata, Y Yanagisawa, M Yamamoto, Y Shimada, K Ozaki, and a Kusumi. Comparison of two-photon excitation laser scanning microscopy with UV-confocal laser scanning microscopy in three-dimensional calcium imaging using the fluorescence indicator Indo-1. *Journal of microscopy*, 185(Pt 1):9–20, 1997.

[19] David W. Piston. Imaging living cells and tissues by two-photon excitation microscopy. *Trends in Cell Biology*, 9(2):66–69, 1999.

[20] Demirhan Kobat, Nicholas G. Horton, and Chris Xu. In vivo two-photon microscopy to 1.6-mm depth in mouse cortex. *Journal of Biomedical Optics*, 16(10):106014, 2011.

[21] Gerhard A. Blab, Piet H.M. Lommerse, Laurent Cognet, Gregory S. Harms, and Thomas Schmidt. Two-photon excitation action cross-sections of the autofluorescent proteins. *Chemical Physics Letters*, 350(1-2):71–77, 2001.

[22] M Drobizhev, S Tillo, N S Makarov, T E Hughes, and A Rebane. Absolute two-photon absorption spectra and two-photon brightness of orange and red fluorescent proteins. *J Phys Chem B*, 113(4):855–859, 2009.

[23] Mikhail Drobizhev, Nikolay S Makarov, Shane E Tillo, Thomas E Hughes, and Aleksander Rebane. Two-photon absorption properties of fluorescent proteins. *Nature Methods*, 8(5):393–399, 2011.

[24] S. Maiti. Measuring Serotonin Distribution in Live Cells with Three-Photon Excitation. *Science*, 275(5299):530–532, 1997.

[25] Stefan Quentmeier, Stefan Denicke, Jan-Eric Ehlers, Raluca A Niesner, and Karl-Heinz Gericke. Two-color two-photon excitation using femtosecond laser pulses. *The Journal of Physical Chemistry B*, 112(18):5768–5773, 2008.

[26] Stefan Quentmeier, Claudia C. Quentmeier, Peter J. Walla, and Karl Heinz Gericke. Two-color two-photon excitation of intrinsic protein fluorescence: Label-free observation of proteolytic digestion of bovine serum albumin. *ChemPhysChem*, 10(9-10):1607–1613, 2009.

[27] S Quentmeier, S Denicke, and K H Gericke. Two-color two-photon fluorescence laser scanning microscopy. *J Fluoresc*, 19(6):1037–1043, 2009.

[28] S Denicke, S Quentmeier, J-E Ehlers, and K-H Gericke. Applications of the time-resolved two-colour two-photon excitation of uv fluorophores using femtosecond laser pulses. *Physica Scripta*, 80(4):048105, 2009.

[29] P Mahou, M Zimmerley, K Loulier, K S Matho, G Labroille, X Morin, W Supatto, J Livet, D Débarre, and E Beaurepaire. Multicolor two-photon tissue imaging by wavelength mixing. *Nat Methods*, 9(8):815–818, 2012.

[30] Robert W Boyd. Nonlinear optics. *Nonlinear Optics (Third Edition)*, 2008.

[31] Thomas Y F Tsang. Optical third-harmonic generation at interfaces. *Phys Rev A*, 52(5):4116–4125, 1995.

[32] Rebecca M. Williams, Warren R. Zipfel, and Watt W. Webb. Interpreting Second-Harmonic Generation Images of Collagen I Fibrils. *Biophysical Journal*, 88(2):1377–1386, 2005.

[33] M Strupler, a M Pena, M Hernest, P-L Tharaux, J-L Martin, E Beaurepaire, and M-C Schanne-Klein. Second harmonic imaging and scoring of collagen in fibrotic tissues. *Optics express*, 15(7):4054–4065, 2007.

[34] Ming-Rung Tsai, Yu-Wei Chiu, Men Tzung Lo, and Chi-Kuang Sun. Second-harmonic generation imaging of collagen fibers in myocardium for atrial fibrillation diagnosis. *Journal of biomedical optics*, 15(April 2010):026002, 2014.

[35] K. N. Anisha Thayil, E. J. Gualda, S. Psilodimitrakopoulos, I. G. Cormack, I. Amat-Roldán, M. Mathew, D. Artigas, and P. Loza-Alvarez. Starch-based backwards SHG for in situ MEFISTO pulse characterization in multiphoton microscopy. *Journal of Microscopy*, 230(1):70–75, 2008.

[36] Z Y Zhuo, C S Liao, C H Huang, J Y Yu, Y Y Tzeng, W Lo, C Y Dong, H C Chui, Y C Huang, H M Lai, and S W Chu. Second harmonic generation imaging - A new method for unraveling molecular information of starch. *Journal of Structural Biology*, 171(1):88–94, 2010.

[37] R.M. Brown Jr, A.C. Millard, and P.J. Campagnola. Macromolecular structure of cellulose studied by second-harmonic generation imaging microscopy. *Optics letters*, 28(22):2207–2209, 2003.

[38] Oleg Nadiarnykh, Ronald B Lacomb, Paul J Campagnola, and William a Mohler. Coherent and incoherent SHG in fibrillar cellulose matrices. *Optics express*, 15(6):3348–3360, 2007.

[39] Hyungsik Lim, Denis Sharoukhov, Imran Kassim, Yanqing Zhang, and James L Salzer. Label-free imaging of Schwann cell myelination by third harmonic generation microscopy. 2014.

[40] D Debarre, W Supatto, A.-M. Pena, A Fabre, T Tordjmann, L Combettes, M.-C. Schanne-Klein, and E Beaurepaire. Imaging lipid bodies in cells and tissues using third-harmonic generation microscopy. *Nat. Methods*, 3(1):47–53, 2006.

[41] E. Abbe. Beiträge zur theorie des mikroskops und der mikroskopischen wahrnehmung. *Archiv für Mikroskopische Anatomie*, 9(1):413–418, 1873.

[42] Born and Wolf. *Principles Of Optics*. Cambridge University Press, Cambridge, 1970.

[43] D W Pohl. Scanning near-field optical microscopy (snom). *Adv. Opt. Electron. Microsc.*, 12:243–312, 1991.

[44] H. Heinzelmann and D. W. Pohl. Scanning near-field optical microscopy. *Applied Physics A Solids and Surfaces*, 59(2):89–101, 1994.

[45] G. Toraldo Di Francia. Super-gain antennas and optical resolving power. *Il Nuovo Cimento*, 9(3 Supplement):426–438, 1952.

[46] W. Lukosz. Optical systems with resolving powers exceeding the classical limit ii. *Journal of the Optical Society of America*, 57(7):932, 1967.

[47] MAA Neil, R Juškaitis, and T Wilson. Real time 3d fluorescence microscopy by two beam interference illumination. *Optics communications*, 153(1-3):1–4, 1998.

[48] Hans Blom and Jerker Widengren. Stimulated emission depletion microscopy. *Chemical reviews*, 117(11):7377–7427, 2017.

[49] William E Moerner and Lothar Kador. Optical detection and spectroscopy of single molecules in a solid. *Physical review letters*, 62(21):2535, 1989.

[50] Michel Orrit and J Bernard. Single pentacene molecules detected by fluorescence excitation in a p-terphenyl crystal. *Physical review letters*, 65(21):2716, 1990.

[51] E Brooks Shera, Newton K Seitzinger, Lloyd M Davis, Richard A Keller, and Steven A Soper. Detection of single fluorescent molecules. *Chemical Physics Letters*, 174(6):553–557, 1990.

[52] R Rigler and J Widengren. Ultrasensitive detection of single molecules by fluorescence correlation spectroscopy. 1990.

[53] Eric Betzig. Proposed method for molecular optical imaging. *Optics letters*, 20(3):237–239, 1995.

[54] AM Van Oijen, J Köhler, J Schmidt, M Müller, and GJ Brakenhoff. 3-dimensional super-resolution by spectrally selective imaging. *Chemical Physics Letters*, 292(1-2):183–187, 1998.

[55] Matthew P Gordon, Taekjip Ha, and Paul R Selvin. Single-molecule high-resolution imaging with photobleaching. *Proceedings of the National Academy of Sciences of the United States of America*, 101(17):6462–6465, 2004.

[56] Eric Betzig, George H Patterson, Rachid Sougrat, O Wolf Lindwasser, Scott Olenych, Juan S Bonifacino, Michael W Davidson, Jennifer Lippincott-Schwartz, and Harald F Hess. Imaging intracellular fluorescent proteins at nanometer resolution. *Science*, 313(5793):1642–1645, 2006.

[57] Samuel T Hess, Thanu PK Girirajan, and Michael D Mason. Ultra-high resolution imaging by fluorescence photoactivation localization microscopy. *Biophysical journal*, 91(11):4258–4272, 2006.

[58] Michael J Rust, Mark Bates, and Xiaowei Zhuang. Sub-diffraction-limit imaging by stochastic optical reconstruction microscopy (storm). *Nature methods*, 3(10):793, 2006.

[59] Mike Heilemann, Sebastian Van De Linde, Mark Schüttpelz, Robert Kasper, Britta Seefeldt, Anindita Mukherjee, Philip Tinnefeld, and Markus Sauer. Subdiffraction-resolution fluorescence imaging with conventional fluorescent probes. *Angewandte Chemie International Edition*, 47(33):6172–6176, 2008.

[60] Stefan W Hell and Matthias Kroug. Ground-state-depletion fluorescence microscopy: A concept for breaking the diffraction resolution limit. *Applied Physics B*, 60(5):495–497, 1995.

[61] Michael Hofmann, Christian Eggeling, Stefan Jakobs, and Stefan W Hell. Breaking the diffraction barrier in fluorescence microscopy at low light intensities by using reversibly photoswitchable proteins. *Proceedings of the National Academy of Sciences of the United States of America*, 102(49):17565–17569, 2005.

[62] Mariano Bossi, Jonas Fölling, Marcus Dyba, Volker Westphal, and Stefan W Hell. Breaking the diffraction resolution barrier in far-field microscopy by molecular optical bistability. *New journal of physics*, 8(11):275, 2006.

[63] Antoine G Godin, Brahim Lounis, and Laurent Cognet. Super-resolution microscopy approaches for live cell imaging. *Biophysical journal*, 107(8):1777–1784, 2014.

[64] Martin Schrader, Franziska Meinecke, Karsten Bahlmann, Matthias Kroug, Christoph Cremer, Erkki Soini, and Stefan W. Hell. Monitoring the excited state of a fluorophore in a microscope by stimulated emission. *Bioimaging*, 3(4):147–153, 1995.

[65] Benjamin Harke, Jan Keller, Chaitanya K Ullal, Volker Westphal, Andreas Schönle, and Stefan W Hell. Resolution scaling in sted microscopy. *Opt Express*, 16(6):4154–4162, 2008.

[66] D Wildanger, R Medda, L Kastrup, and SW Hell. A compact sted microscope providing 3d nanoscale resolution. *Journal of microscopy*, 236(1):35–43, 2009.

[67] Christian A Wurm, Kirill Kolmakov, Fabian Göttfert, Haisen Ta, Mariano Bossi, Heiko Schill, Sebastian Berning, Stefan Jakobs, Gerald Donnert, Vladimir N Belov, et al. Novel red fluorophores with superior performance in sted microscopy. *Optical Nanoscopy*, 1(1):7, 2012.

[68] Fabian Göttfert, Christian A Wurm, Veronika Mueller, Sebastian Berning, Volker C Cordes, Alf Honigmann, and Stefan W Hell. Coaligned dual-channel sted nanoscopy and molecular diffusion analysis at 20 nm resolution. *Biophysical journal*, 105(1):L01–L03, 2013.

[69] Kirill Kolmakov, Christian A Wurm, Dirk NH Meineke, Fabian Göttfert, Vadim P Boyarskiy, Vladimir N Belov, and Stefan W Hell. Polar red-emitting rhodamine dyes with reactive groups: synthesis, photophysical properties, and two-color sted nanoscopy applications. *Chemistry-A European Journal*, 20(1):146–157, 2014.

[70] Giuseppe Vicidomini, Gael Moneron, Christian Eggeling, Eva Rittweger, and Stefan W Hell. Sted with wavelengths closer to the emission maximum. *Optics express*, 20(5):5225–5236, 2012.

[71] Gerald Donnert, Jan Keller, Rebecca Medda, M Alexandra Andrei, Silvio O Rizzoli, Reinhard Lührmann, Reinhard Jahn, Christian Eggeling, and Stefan W Hell. Macromolecular-scale resolution in biological fluorescence microscopy. *Proceedings of the National Academy of Sciences*, 103(31):11440–11445, 2006.

[72] J B Ding, K T Takasaki, and B L Sabatini. Supraresolution imaging in brain slices using stimulated-emission depletion two-photon laser scanning microscopy. *Neuron*, 63(4):429–437, 2009.

[73] K I Willig and U V Nägerl. Stimulated emission depletion (STED) imaging of dendritic spines in living hippocampal slices. *Cold Spring Harb Protoc*, 2012(5), 2012.

[74] J Tønnesen and U V Nägerl. Two-color sted imaging of synapses in living brain slices. *Methods Mol Biol*, 950:65–80, 2013.

[75] Travis J Gould, Daniel Burke, Joerg Bewersdorf, and Martin J Booth. Adaptive optics enables 3d sted microscopy in aberrating specimens. *Optics express*, 20(19):20998–21009, 2012.

[76] Brian R Patton, Daniel Burke, David Owald, Travis J Gould, Joerg Bewersdorf, and Martin J Booth. Three-dimensional sted microscopy of aberrating tissue using dual adaptive optics. *Optics express*, 24(8):8862–8876, 2016.

[77] Wei Yan, Yanlong Yang, Yu Tan, Xun Chen, Yang Li, Junle Qu, and Tong Ye. Coherent optical adaptive technique improves the spatial resolution of sted microscopy in thick samples. *Photonics Research*, 5(3):176–181, 2017.

[78] Qifeng Li, Yang Wang, Da Chen, and Sherry SH Wu. 2pe-sted microscopy with a single ti: sapphire laser for reduced illumination. *PloS one*, 9(2):e88464, 2014.

[79] Teodora Scheul, Ciro D'Amico, Irène Wang, and Jean-Claude Vial. Two-photon excitation and stimulated emission depletion by a single wavelength. *Optics Express*, 19(19):18036, 2011.

[80] A Hense, B Prunsche, P Gao, Y Ishitsuka, K Nienhaus, and G U Nienhaus. Monomeric Garnet, a far-red fluorescent protein for live-cell STED imaging. *Sci Rep*, 5:18006, 2015.

[81] B E A Saleh and M C Teich. *Fundamentals of photonics*, volume 24. Wiley Interscience, 1992.

[82] M Massari, G Ruffato, M Gintoli, F Ricci, and F Romanato. Fabrication and characterization of high-quality spiral phase plates for optical applications. *Appl. Opt.*, 54(13):4077–83, 2015.

[83] FRancesco Ricci. *Experimental Study of Phase Singularities in Optical Beams Carrying Orbital Angular Momentum*. PhD thesis, 2012.

[84] Zheng Cui. *Nanofabrication: Principles, Capabilities and Limits*. Springer, 2008.

[85] Ivor Brodie and Julius J Muray. *The physics of micro/nano-fabrication*. 1992.

[86] Bryan Cord, Joel Yang, Huigao Duan, David C. Joy, Joseph Klingfus, and Karl K. Berggren. Limiting factors in sub-10nm scanning-electron-beam lithography. *Journal of Vacuum Science & Technology B: Microelectronics and Nanometer Structures*, 27(6):2616, 2009.

[87] Nezih Unal, Martin D.B. Charlton, Yudong Wang, Ulrike Waizmann, Thomas Reindl, and Ulrich Hofmann. Easy to adapt electron beam proximity effect correction parameter calibration based on visual inspection of a "best dose sensor". *Microelectronic Engineering*, 88(8):2158–2162, aug 2011.

[88] Stephan Armin Wacker, Cristobal Alvarado, Götz von Wichert, Uwe Knippschild, Jörg Wiedenmann, Karen Clauß, Gerd Ulrich Nienhaus, Horst Hameister, Bernd Baumann, Tilman Borggrefe, Walter Knöchel, and Franz Oswald. Rita, a novel modulator of notch signalling, acts via nuclear export of rbp-j. *The EMBO Journal*, 30(1):43–56, 2011.

[89] Alessandra Castaldi, Tania Zaglia, Vittoria Di Mauro, Pierluigi Carullo, Giacomo Viggiani, Giulia Borile, Barbara Di Stefano, Gabriele Giacomo Schiattarella, Maria Giovanna Gualazzi, Leonardo Elia, Giuliano Giuseppe Stirparo, Maria Luisa Colorito, Gianluigi Pironti, Paolo

Kunderfranco, Giovanni Esposito, Marie Louise Bang, Marco Mongillo, Gianluigi Condorelli, and Daniele Catalucci. MicroRNA-133 modulates the beta1-adrenergic receptor transduction cascade. *Circulation Research*, 115(2):273–283, 2014.

[90] G P Fadini, L Menegazzo, M Rigato, V Scattolini, N Poncina, A Bruttocao, S Ciciliot, F Mammano, C D Ciubotaru, E Brocco, M C Marescotti, R Cappellari, G Arrigoni, R Millioni, S Vigili de Kreutzenberg, M Albiero, and A Avogaro. Netosis delays diabetic wound healing in mice and humans. *Diabetes*, 65(4):1061–1071, 2016.

[91] Andrea Filippi, Giulia Borile, Eleonora Dal Sasso, Laura Iop, Andrea Armani, Michele Gintoli, Marco Sandri, Gino Gerosa, and Filippo Romanato. Multiphoton label-free ex-vivo imaging using a custom-built dual-wavelength microscope with chromatic aberrations compensation. sep 2017.

[92] Silvia Galiani, Benjamin Harke, Giuseppe Vicidomini, Gabriele Lignani, Fabio Benfenati, Alberto Diaspro, and Paolo Bianchini. Strategies to maximize the performance of a STED microscope. *Optics express*, 20(7):7362–74, mar 2012.

[93] Eva Rittweger, Kyu Young Han, Scott E. Irvine, Christian Eggeling, and Stefan W. Hell. Sted microscopy reveals crystal colour centres with nanometric resolution. *Nature Photonics*, 3(3):144–147, Feb 2009.

[94] P. Bianchini, B. Harke, S. Galiani, G. Vicidomini, and A. Diaspro. Single-wavelength two-photon excitation-stimulated emission depletion (sw2pe-sted) superresolution imaging. *Proceedings of the National Academy of Sciences*, 109(17):6390–6393, 2012.

[95] G P Fadini, L Menegazzo, V Scattolini, M Gintoli, M Albiero, and A Avogaro. A perspective on netosis in diabetes and cardiometabolic disorders. *Nutr Metab Cardiovasc Dis*, 26(1):1–8, 2016.

[96] X-C Yuan, J Lin, J Bu, and RE Burge. Achromatic design for the generation of optical vortices based on radial spiral phase plates. *Optics express*, 16(18):13599–13605, 2008.

List of Figures

List of Tables